

# Analytical and Experimental Investigation of Insect Respiratory System Inspired Microfluidics

Krishnashis Chatterjee

Dissertation submitted to the Faculty of the  
Virginia Polytechnic Institute and State University  
in partial fulfillment of the requirements for the degree of

Doctor of Philosophy

in

Engineering Mechanics

Anne E. Staples, Chair

Rafael Davalos

John J. Socha

Saad A. Ragab

Alexandrina Untaroiu

September 20, 2018

Blacksburg, Virginia

Keywords: Microfluidics, insect-inspired, microscale pumping, slip boundary conditions, single actuation, frequency dependent flow control.

Copyright 2018, Krishnashis Chatterjee

# Analytical and Experimental Investigation of Insect Respiratory System Inspired Microfluidics

Krishnashis Chatterjee

(ABSTRACT)

There have been considerable advances in the complexity and miniaturization of microfluidic devices, but there remains an actuation overhead problem: these small, complex microfluidic devices are tethered to extensive off-chip machinery that limit their portability and efficiency. Insects, in contrast, efficiently handle their respiratory air flows in complex networks consisting of thousands of microscale tracheal pathways. This work analytically and experimentally investigates incorporating some of the essential kinematics and actuation strategies of insect respiratory systems in microfluidic devices. Two mathematical models of simplified individual tracheal pathways were derived and analyzed. The first was a model of slip flow in a rectangular microchannel with rhythmic wall contractions, meant to model the essential features of flows in mid-scale insect tracheal pathways. The second was a model in the same mid-scale regime, but with a more realistic circular tracheal pathway geometry and with physiological pressure boundary conditions taken from the entomological literature. Both models showed a reduction in flow rate with an increase in the slip parameter for the shear-driven flows under study. Finally, a total of fifteen insect-mimetic single-channel and network polydimethylsiloxane (PDMS) valveless microfluidic devices were fabricated and tested using standard soft lithography techniques. It was found that these devices are capable of pumping fluids very efficiently using insect-mimetic actuation techniques, and also that the fluid flow direction and magnitude in the devices could be controlled via the actuation frequency alone, a feature never before realized in a microfluidic device. These results suggest that insect-mimicry may be a promising direction for designing more efficient microfluidic devices.

# Analytical and Experimental Investigation of Insect Respiratory System Inspired Microfluidics

Krishnashis Chatterjee

(GENERAL AUDIENCE ABSTRACT)

Microfluidics or the study of fluids at the microscale has gained a lot of interest in the recent past due to its various applications starting from electronic chip cooling to biomedical diagnostic devices and exoplanetary chemical analysis. Though there has been a lot of advancements in the functionality and portability of microfluidic devices, little has been achieved in the improvement of the peripheral machinery needed to operate these devices. On the other hand insects can expertly manipulate fluids, in their body, at the microscale with the help of their efficient respiratory capabilities. In the present study we mimic some essential features of the insect respiratory system by incorporating them in microfluidic devices. The feasibility of practical application of these techniques have been tested, at first, analytically by mathematically modeling the fluid flow in insect respiratory tract mimetic microchannels and tubes and then by fabricating, testing and analyzing the functionality of microfluidic devices. The mathematical models, using slip boundary conditions, showed that the volumetric fluid flow through a trachea mimetic tube decreased with the increase in the amount of slip. Apart from that it also revealed a fundamental difference between shear and pressure driven flow at the microscale. The microfluidic devices exhibited some unique characteristic features never seen before in valveless microfluidic devices and have the potential in reducing the actuation overhead. These devices can be used to simplify the operating procedure and subsequently decrease the production cost of microfluidic devices for various applications.

# Dedication

*Dedicated to Anuradha Sen Chatterjee*

# Acknowledgments

My journey as a graduate student in the Department of Biomedical Engineering and Mechanics has been a pleasant learning experience. So, I would like to thank all those people without whom this would not have been possible.

I would like to express my sincere gratitude to my advisor Dr. Anne Staples, who has been a source of constant support, guidance and motivation. She has been there beside me whenever I needed her help, advice and understanding. Thanks, Dr. Staples!

I acknowledge all other committee members, Dr. Davalos, Dr. Socha, Dr. Ragab, and Dr. Untaroiu, for their valuable advice and input on my research. In addition, I would like to specially thank Dr. Davalos for his support and advice which provided a new direction to my research. I also greatly appreciate the help and guidance that I received from Dr. Socha.

My parents and my brother have always been the source of inspiration which helped me to keep moving forward through the ups and downs of my life. Thank you baba, maa, bhai. Last but not the least I am greatly indebted to my fiancée Anuradha for her constant help, support, motivation and unconditional love and care without whom this journey would not have been possible.

At the end I would like to thank the almighty who has bestowed his blessings upon me throughout my life.

# Contents

<b>List of Figures</b>	<b>x</b>
<b>List of Tables</b>	<b>xvii</b>
<b>1 Introduction</b>	<b>1</b>
1.1 Motivation and overview . . . . .	1
1.2 Literature review . . . . .	3
1.3 Contributions . . . . .	10
1.4 Research outline . . . . .	12
<b>References</b>	<b>15</b>
<b>2 Slip flow in a microchannel driven by rhythmic wall contractions</b>	<b>20</b>
2.1 Abstract . . . . .	20
2.2 Introduction . . . . .	21
2.3 Problem Schematic . . . . .	26
2.4 Mathematical Model . . . . .	27
2.5 Results . . . . .	31
2.5.1 Channel wall profiles, $H_1(x, t)$ and $H_2(x, t)$ . . . . .	32

2.5.2	Model Validation . . . . .	34
2.5.3	Velocity and pressure . . . . .	36
2.5.4	Comparison of streamlines . . . . .	42
2.5.5	Net flow produced . . . . .	47
2.6	Conclusions . . . . .	49
	<b>References</b>	<b>51</b>
<b>3</b>	<b>Slip flow in a microtube driven by rhythmic wall collapses</b>	<b>55</b>
3.1	Abstract . . . . .	55
3.2	Introduction . . . . .	56
3.3	Mathematical modeling . . . . .	61
3.4	Results . . . . .	64
3.4.1	Wall contraction profiles . . . . .	64
3.4.2	Velocity and pressure . . . . .	66
3.4.3	Net flow produced . . . . .	69
3.5	Conclusions . . . . .	71
	<b>References</b>	<b>73</b>
<b>4</b>	<b>Frequency-specific, single-actuation flow control in insect-mimetic valveless microfluidic devices</b>	<b>77</b>

4.1	Abstract . . . . .	77
4.2	Introduction . . . . .	78
4.3	Results and discussion . . . . .	83
4.4	Concluding remarks and future scope . . . . .	97
	<b>References</b>	<b>99</b>
<b>5</b>	<b>Conclusions and future work</b>	<b>103</b>
5.1	Summary and concluding remarks . . . . .	103
5.2	Recommendations for future research . . . . .	106
	<b>Appendices</b>	<b>107</b>
	<b>Appendix A</b>	<b>108</b>
A.1	Derivation of reduced governing equations used in chapters 2 and 3 . . . . .	108
	<b>Appendix B</b>	<b>110</b>
B.1	Materials and methods . . . . .	110
	<b>Appendix C</b>	<b>115</b>
C.1	CAD designs of the devices with dimensions . . . . .	115
C.2	Masks of the channel device designs . . . . .	116
C.3	Fabrication and assembly of the microfluidic devices . . . . .	117

C.4 Schematic of the experimental setup . . . . .	118
---	-----

# List of Figures

2.1	(a) 3D view of the tracheal system in the thorax of a carabid beetle ( <i>Platynus decentis</i> ) with a highlighted portion showing the part modeled here (reproduced with permission from [35]). (b) Time dependence of the upper wall collapse functions ( $g_1(t)$ and $g_2(t)$ ). (c) Problem Schematic: 2D rectangular channel with moving lower wall contraction profile $H_1(x, t)$ and upper wall contraction profile $H_2(x, t)$ . . . . .	27
2.2	(a) Pressure gradient $dp/dx$ and static pressure $p$ . (b) $u$ and $v$ velocities for no-slip boundary conditions with single wall contractions at $t = T/4$ and $\theta_{12} = 0^\circ$ . The dashed lines represent the channel walls. From [7]. . . . .	35
2.3	(a) Pressure gradient $dp/dx$ and static pressure $p$ . (b) $u$ and $v$ velocities for no-slip boundary conditions with single wall contractions at $t = T/4$ and $\theta_{12} = 0^\circ$ . The dashed lines represent the channel walls. Plots from present study. . . . .	35
2.4	Comparison of $u$ , $p$ , and $dp/dx$ for $\theta_{12} = 0^\circ$ at $t = T/4$ and $t = 3T/4$ . Three representative cases are shown: no slip ( $\beta = 0$ ), low slip ( $\beta = 0.01$ ) and high slip ( $\beta = 0.1$ ). . . . .	38
2.5	Comparison of $u$ , $p$ , and $dp/dx$ for $\theta_{12} = 30^\circ$ at $t = T/4$ and $t = 3T/4$ . Three representative cases are shown: no slip ( $\beta = 0$ ), low slip ( $\beta = 0.01$ ) and high slip ( $\beta = 0.1$ ). . . . .	40
2.6	Streamlines for no slip ( $\beta = 0$ ) at $t = T/4$ and $\theta_{12} = 0^\circ$ . . . . .	42

2.7	Streamlines for low slip ( $\beta = 0.01$ ) at $t = T/4$ and $\theta_{12} = 0^\circ$ . . . . .	43
2.8	Streamlines for high slip ( $\beta = 0.1$ ) at $t = T/4$ and $\theta_{12} = 0^\circ$ . . . . .	43
2.9	Streamlines for no slip ( $\beta = 0$ ) at $t = T/4$ and $\theta_{12} = 30^\circ$ . . . . .	44
2.10	Streamlines for low slip ( $\beta = 0.01$ ) at $t = T/4$ and $\theta_{12} = 30^\circ$ . . . . .	45
2.11	Streamlines for high slip ( $\beta = 0.1$ ) at $t = T/4$ and $\theta_{12} = 30^\circ$ . . . . .	45
2.12	Streamlines for no slip ( $\beta = 0$ ) at $t = 3T/4$ and $\theta_{12} = 30^\circ$ . . . . .	46
2.13	Streamlines for low slip ( $\beta = 0.01$ ) at $t = 3T/4$ and $\theta_{12} = 30^\circ$ . . . . .	46
2.14	Streamlines for high slip ( $\beta = 0.1$ ) at $t = 3T/4$ and $\theta_{12} = 30^\circ$ . . . . .	46
2.15	Time averaged net flow rate plotted for different phase lag values over an entire cycle at $x = 0.5$ . Three cases are shown: no slip ( $\beta = 0$ ), low slip ( $\beta = 0.01$ ) and high slip ( $\beta = 0.1$ ). The circles on the plots represent the data points from calculations using Eq. 2.9. The solid and dashed curves are cubic splines fit to the calculated points in order to demonstrate the trend of the calculations. . . . .	48
3.1	Comparison of $V_x$ for $\theta_{12} = 30^\circ$ at $t = T/4$ and $t = 3T/4$ . Three representative cases are shown: high slip ( $\beta = 0.1$ ), low or intermediate slip ( $\beta = 0.01$ ), and no slip ( $\beta = 0$ ). . . . .	67
3.2	Comparison of $p$ for $\theta_{12} = 30^\circ$ at $t = T/4$ and $t = 3T/4$ . Three representative cases are shown: high slip ( $\beta = 0.1$ ), low or intermediate slip ( $\beta = 0.01$ ), and no slip ( $\beta = 0$ ). . . . .	68

3.3	Comparison of $dp/dx$ for $\theta_{12} = 30^\circ$ at $t = T/4$ and $t = 3T/4$ . Three representative cases are shown: high slip ( $\beta = 0.1$ ), low or intermediate slip ( $\beta = 0.01$ ), and no slip ( $\beta = 0$ ). . . . .	68
3.4	Time-averaged net flow rate plotted against phase lag values over an entire contraction-relaxation cycle at $x = 0.5$ . Three representative cases are shown: high slip ( $\beta = 0.1$ ), low or intermediate slip ( $\beta = 0.01$ ), and no slip ( $\beta = 0$ ). The asterisk marks on the plots represent the data points. The solid solid and the dashed lines are cubic splines fit to the data points showing the trend of calculations. . . . .	70
4.1	<b>a</b> , Synchrotron X-ray image of <i>Platynus decentis</i> (top view) head and thorax with largest thoracic respiratory tracts highlighted (modified by J.J. Socha with permission from [26]). <i>Inset 1 – 4</i> : Time series images of directional tracheal collapse in the bess beetle, <i>Odontotaenius disjunctus</i> . Collapse propagates from lower left of image (red point pair) to upper right (yellow point pair).([18]). <b>b</b> , Synchrotron X-ray image of the largest thoracic tracheae, fully inflated, in <i>Pterostichus stygicus</i> . <b>c</b> , Synchrotron X-ray image of the largest thoracic tracheae, fully collapsed with discrete collapse location indicated ([14]).	80

4.2	Schematics of the eleven single-channel devices fabricated and tested. Positive flow is in the direction of the ‘+’ symbol. The grey channels are the actuating channels, and the colored ones are fluid channels. The grey arrows show the direction of the pressurized gas inflow into the actuating channel. Devices S2 and S4-9 produce the directional collapse phenomenon observed in insects by incorporating a tapered flow channel. Devices S1 and S3-11 produce the discrete collapse phenomenon observed in insects by incorporating two discrete collapse locations. Devices S6-11 produce a time lag between discrete collapses by incorporating a u-shaped actuation channel. . . . .	81
4.3	<b>a</b> , Schematic (side view) of three layer PDMS device. Bottom (clear) layer is a foundational layer consisting of a glass slide. Grey layers are cured PDMS. Blue layer is the flow channel (depth is 80 $\mu\text{m}$ for all devices, width varies from 100-1000 $\mu\text{m}$ ). Dark grey layer is the elastomeric membrane that serves as the flow channel ceiling (thickness 14-20 $\mu\text{m}$ ). Clear top channels are the actuation channels into which pressurized gas is released and subsequently evacuated in order to collapse the flow channel ceiling. <b>b</b> , A representative pressure signal in the actuation channel. . . . .	82
4.4	Volumetric flow rate versus actuation frequency for all eleven single-channel devices. All devices produce unidirectional flow in response to a single, symmetric actuation signal. Device S4 reverses the flow direction above a critical actuation frequency threshold of approximately 4 Hz. . . . .	84

4.5	Volumetric flow rate versus actuation frequency for Device S4 with error envelope. The shading represents the uncertainty in the data due to measurement error and is calculated as the maximum possible error in the volumetric flow rate due to the resolution of the measurement of the time taken by the fluid front to travel a certain distance in the outlet tube. . . . .	85
4.6	Volumetric flow rate versus actuation pressure magnitude for device S11. The shading represents the uncertainty in the data due to measurement error and is calculated as the maximum possible error in the volumetric flow rate due to the resolution of the measurement of the time taken by the fluid front to travel a certain distance in the outlet tube. . . . .	88
4.7	Top view of device S4 over a complete collapse and re-expansion cycle. Left column displays collapse images. Right column displays re-expansion images.	89
4.8	Maximum deflection versus actuation pressure for larger and smaller contractions of Device S4. . . . .	90
4.9	Pressure range of flow transition from one direction to the other plotted against actuation frequency for Device S4. The ‘+’ and the ‘−’ signs represent flows towards the positive and negative directions respectively. . . . .	91
4.10	<b>a</b> , Synchrotron X-ray image of <i>Platynus decentis</i> (top view) head and thorax with largest thoracic respiratory tracts highlighted (modified by J.J. Socha with permission from [26]). <b>b</b> , Photograph of fabricated microfluidic network device mimicking the highlighted part as shown in Fig. 4.10(a) with green dye in the flow channel and red dye in the overlying actuation channel for visualization purposes. . . . .	92

<p>4.11 Schematics and flow rate data for two multichannel microfluidic devices. Both the devices are left-right symmetric. Positive flow is toward the top of the device, in the direction of the ‘+’ symbol. The shading represents the uncertainty in the data due to measurement error and is calculated as the maximum possible error in the volumetric flow rate due to the resolution of the measurement of the time taken by the fluid front to travel a certain distance in the outlet tube. <b>a</b>, Device M1 displays frequency-dependent channel selectivity. Below a critical actuation frequency, there is no flow produced through channel C, positive flow through channel A, and negative flow through channel B. After the critical frequency (about 5 Hz) there is positive flow through channel C, positive flow through channel A and negative flow through channel B. <b>b</b>, Device M2 produces positive flow through all three channels, A,B, and C, at every actuation frequency tested. . . . .</p>	93
<p>4.12 Schematics and flow rate data for two multichannel microfluidic devices. Both the devices are left-right symmetric. Positive flow is toward the top of the device, in the direction of the ‘+’ symbol. The shading represents the uncertainty in the data due to measurement error and is calculated as the maximum possible error in the volumetric flow rate due to the resolution of the measurement of the time taken by the fluid front to travel a certain distance in the outlet tube. <b>a</b>, Device M3 produces negligible flow through channel B for actuation frequencies below a threshold frequency of about 1 Hz, after which it produces a negative flow in channel B. The device produces positive flow in channels A and C for all actuation frequencies tested. <b>b</b>, Device M4 produces positive flow through channels A and C and negative flow through channel B at every actuation frequency tested. . . . .</p>	94

4.13	Tests were performed in half the symmetric network with water mixed with food coloring. The actuation pressures for the tests was 13 psi. Flow direction convention is the same as in 4.11 or 4.12. <b>a</b> , Device M3 actuated at high frequency (5 Hz). At this frequency, which is higher than the critical frequency for device M3, the black liquid from the reservoir feeding channel B walls pumped in the negative direction and mixed with the green fluid in channel A, which pumped fluid in the forward direction. Channel C also pumped fluid in the forward direction. <b>b</b> , Device M3 actuated at low frequency (0.33 Hz). At this frequency below the critical frequency frequency for device M3, no black fluid is pumped from the reservoir into channel B, while the green fluid in channels A and C is pumped forward. . . . .	96
4.14	Tests were performed in half the symmetric network with water mixed with food coloring. The actuation pressures for the tests was 17 psi. Flow direction convention is the same as in 4.11 or 4.12. <b>a</b> , Device M4 actuated at 1.25 Hz, contraction part of cycle. fluid was pumped from channel A and channel C into channel B. <b>b</b> , Device M4 actuated at 1.25 Hz, re-expansion part of cycle. Fluid continued to be pumped from channels A and C into channel B. . . . .	97
C.1	CAD designs with dimensions (in $\mu\text{m}$ ) for devices S1 (top left), S10/S11 (top right), S2 (bottom left) and S4 (bottom right). All the dimensions are in $\mu\text{m}$ .	115
C.2	Masks created from the CAD designs, that were used to create the silicon wafer.	116
C.3	<b>a</b> , Schematic of the soft lithography fabrication technique. <b>b</b> , Assembly process of the microfluidic devices. . . . .	117
C.4	Schematic of the experimental set up. . . . .	118

# List of Tables

2.1	Relevant Knudsen number regimes through the insect respiratory system. . .	29
2.2	Values of parameters used in generating the plots in Figs. 2.3 - 2.15. . . . .	32

# Chapter 1

## Introduction

*Look deep into nature, and then you will understand everything better.*

A. Einstein

### 1.1 Motivation and overview

Microfluidic technology is currently a critical research area in a wide range of disciplines ranging from molecular biology to medicine to microelectronics. Although it is considered to be a technology in its nascent stage, it has already gained wide popularity for a number of advantages over conventional macroscale fluid flow handling technologies. Microfluidic devices are economical in fabrication cost due to their small sizes, use smaller amounts of working fluids, and deal mainly with laminar flow thus getting rid of the complications that arise due to turbulence. In molecular biology, microfluidics finds applications in different analytical techniques such as gas phase and high pressure liquid chromatography and electrophoresis. In biomedical engineering, apart from the revolutionary organ-on-a-chip devices, bioassays with microfluidic networks are used for targeted drug delivery research. Microfluidics also has wide applications in silicon microelectronics, microelectromechanical systems, and electronic chip cooling. All these have been made possible by the advances made in photolithography and silicon micromachining techniques. But the current state-of-the-art microfluidic devices which are comprised of complex networks of microchannels, rely on the

coordinated actuation of many different valves and micropumps in order to drive the flow in the desired direction at the desired rate. The fabrication and operation of these devices can be expensive and complex, and they depend upon several factors for their successful performance.

In contrast, studies of insect respiratory systems, in particular, synchrotron x-ray imaging of active respiration in some insects, have revealed elegant and novel microscale pumping techniques with a low actuation overhead. In those insects, these techniques which consist of the periodic, localized buckling of the tracheal channel walls in response to abdominal compressions are thought to pressurize the fluid in the abdominal cavity. Directional tracheal channel collapses have been observed in at least one species of beetle with a traveling collapse wave appearing to propagate along the axis of the channel. And two or more discrete collapse locations with a lag in the timing of their relative collapses has been hypothesized to occur. Both these actuation methods may produce unidirectional flows in insect respiratory systems.

Mathematical models of insect respiratory system-inspired flow actuation in simplified model tracheal channels in the no-slip flow regime were derived and analyzed in previous studies by Aboelkassem and Staples. These studies found that two or more discrete collapse sites could produce a unidirectional flow in a model tracheal pathway with zero pressure gradient as long as there was a break in temporal symmetry. This break in symmetry was accomplished in the models by introducing a time (phase) lag between the collapse events.

But the practical implementation of insect-inspired flow actuation methods in microfluidic devices was not investigated before the present work. Additionally, since insect respiratory flows occur at and below the scale at which rarefaction effects become significant for gaseous flows, the previous models of Aboelkassem and Staples were extended here by Chatterjee and Staples to investigate the effects of slip on the mathematical models of fluid pumping in insect tracheal pathways. Thus, the studies in this work start with the investigation of the

effects of slip boundary conditions in flows through microchannels and microtubes driven by rhythmic contractions of the channel wall, and are followed by an experimental investigation of PDMS based single and multiple channel microfluidic devices that mimic key features of insect respiratory systems to produce and control unidirectional flows.

## 1.2 Literature review

Over the last two decades microfluidic technology has seen a remarkable development with a drastic increase in the number of application areas. Starting from complicated organ-on-a-chip devices and exoplanetary chemical analysis on microfluidic cards, the diversity of the applications of microfluidic technology extends up to mimicking cellular microenvironment and fabrication of microfluidic large-scale integration (mLSI) and microfluidic very-large-scale-integration (mVLSI) devices. Since, at the microscale, portability, precision and cost effectiveness are important factors that drive the development of technology, any advancement in the simplification and refinement of the accessory machinery that preferentially drives the flow in different directions on the chip is a substantial improvement in the functionality. The present study aims to address this particular issue by attempting to simplify and reduce the actuation overhead required to drive the fluid flow in microfluidic devices. In this section, a thorough and detailed review of the relevant important studies have been presented in order to acclimatize the readers to the context and importance of this current study.

A detailed review of polydimethylsiloxane (PDMS) based microfluidic devices for applications in biological studies was first presented by Sia and Whitesides in [1]. In their study the authors extensively analyzed the advantages of using PDMS for miniaturized biological studies e.g., immunoassays, cell sorting and manipulation, and separation of proteins and

DNA. With a special emphasis on cell biology, advantages of miniaturization of biological analyses were also outlined. In his seminal paper on the use of organs-on-chips for reverse engineering of human pathophysiology [2], Donald Ingber outlined the importance of developing microscale systems that enable the analysis of communications and interactions between cells and tissues in an organ context. Thus the organ-on-chip systems that can incorporate living cells for the study of human physiology and pathophysiology, are excellent *in vitro* models that enable high-throughput and precise cell culture control. They are economically sustainable and are substitutes for animal testing. Each of these devices has specific technical requirements and they hold great promise for the investigation of disease pathogenesis [3]. A four-organ-chip interconnected model for the co-culture of human liver, skin, intestine, and kidney was developed to mimic the microphysiological functionality of these organs [4]. Preformed human skin and intestine models have been integrated with 3D-based spheroid, equivalent to liver lobules and polymeric membrane lined with human proximal tubule epithelial cells in order to create the four-organ-chip model. A peristaltic micropump, generating a pulsatile media flow was used to interconnect the models of the four organs. This study was the first of its kind to attempt the integration of multiple organs into a system for *in vitro* microfluidic profiling. A human “breathing lung-on-a-chip” micro device model was proposed by Dongeun Huh in [5]. This model enabled the reconstitution of the microarchitecture, mechanical behavior and physiological functionality of the alveolar-capillary interface and is suitable for modeling human disease processes. A lung-on-a-chip array that reproduces the pulmonary parenchymal environment, alveolar barrier, and breathing induced cyclic strain was fabricated in [6]. Co-cultured epithelial and endothelial cells that formed tight monolayers on both sides of a membrane was subjected to cyclic strain, which was found to influence the cytokine secretion and metabolic activity of the epithelial cells. The results highlight the importance of mechanical strain and the suitability of this device as a lung-on-a-chip model. A lung-on-a-chip microdevice was used to model pulmonary

edema, induced by drug toxicity in [9]. It was found that the mechanical forces resulting from physiological breathing motions played an important role in the increase of vascular leakage that lead to pulmonary edema. Potential new therapeutics were also identified by the study. Human Caco-2 cells were found to undergo robust morphogenesis of intestinal villi when exposed to physiological peristalsis motion in microfluidic ‘Gut-on-a-Chip’ devices [7]. Thus the cells were used to recreate the human intestinal villi lined with four different types of epithelial cells. This Gut-on-a-Chip model can serve as a useful tool for mechanistic research and drug testing. Kim et. al. in [8] developed a biomimetic human gut-on-a-chip microdevice with epithelial cell coated porous membrane separating two microfluidic channels, a model that mimics the physiology of the intestine. The cells were subjected to low shear stress and cyclic strains to mimic physiological peristaltic motions. These epithelial cells polarized and grew into folds that recapitulated the internal structure of the intestinal villi. Thus, this model successfully recreated multiple functional and physical features of the human intestine. A thorough review of the advantages of microfluidic devices for applications in *in vitro* brain slice research has been performed in [10]. The authors outlined several advantages of the use of microfluidic techniques which are overcoming of limitations of interface and submerged slice chambers, better spatiotemporal control on drug delivery to specific regions and possibility of successful integration with current physiological and optical techniques. Park et. al. in [11] developed a microfluidic chip based on neurospheroids that mimic the brain microenvironment by maintaining a constant fluid flow by using an osmotic micropump. The effects the flow on neural network, neurospheroid size, and neural differentiation were investigated. The toxic effects of amyloid- $\beta$ , a major contributor in Alzheimer’s disease were also analyzed. It was found that the viability of neurospheroids was greatly reduced when the amyloid- $\beta$  was treated with an osmotic micropump. This also caused significantly more neural network destruction compared to the treatment under static conditions. The authors concluded that their device was able to recreate *in vivo*-like brain

microenvironments that could model neurodegenerative diseases and drug screening. The blood-brain-barrier allows selective passage of compounds into the central nervous system, thus increasing the difficulty of drug development. Conventional dynamic and static transwell models of the *in vitro* blood-brain-barrier lacks, thin interface layer of dual cell layers and fluid shear stress respectively. In [12] Booth and Kim tried address these limitations by creating a model with a thin culture membrane and a dynamic environment. They tested the validity of their model with optical imaging, permeability assays, and trans-endothelial electrical resistance (TEER) and concluded that it was suitable for investigations involving drug delivery and blood-brain-barrier functions. fabrication of microfluidic devices specially targeted for neuroscience research has also gained impetus in recent times. Taylor et. al. in [13] describes the fabrication of a multi-component PDMS-based microfluidic device for neuroscience research. The two components of the device were separated by a barrier with micron-size grooves to allow the growth of neurites across the compartment. The authors used polylysine patterning to facilitate visualization and identification of neurons. They claimed that by directing the sites of attachment of the neurons and outgrowth of neurite along with isolating the compartments fluidically had significant advantages over the conventional neuronal culture methods. A human neurovascular unit was modeled by fabricating a linked organ-on-chip model by Maoz et. al. in [14] revealed the metabolic coupling of neuronal and endothelial cells and could serve as an *in vitro* approach for investigating the efficiency, transport, action mechanism, and toxicity of neuroactive drugs. A protocol describing the fabrication of a microfluidic culture platform compatible with microscopy methods was proposed by Park et. al. in [15]. The multi-compartment device was made of tiny channels with the ability to culture a few thousand cells. Their device could find potential applications in modeling neurodegeneration and injury of the central nervous system. Apart from the organ-on-chip applications as described till now, microfluidic technology finds application in diverse fields e.g., in extraterrestrial in Situ analysis. In [16] Mora et.al.

provides a detailed outline for the automation of microfluidics for extraterrestrial chemical analysis. The process of laser-induced fluorescence (LIF) along with microchip capillary electrophoresis ( $\mu$ CE) served the purpose earlier but they lacked the necessary automation. The authors in [16] describe a fully integrated microfluidic device which can perform amino acid analyses by LIF and  $\mu$ CE. An electrophoretic channel was integrated along with pneumatically actuated pumps and valves for autonomous routing of fluids in the desired direction. Electrophoretic analysis and sample pretreatment was performed by via computer control. Microfluidic devices are also used for high throughput chemical analysis of cells as outlined in [17]. Jurkat cells loaded with fluorogenic dyes were used to perform electrophoretic separation, integrated cell handling, and rapid cell lysis. A fully integrated microfluidic device for DNA sequencing-by-synthesis was developed by Kartalov and Quake as mentioned in [18]. Using their microfluidic device along with fluorescence detection, the authors could sequence 4 consecutive bps. Other microfluidic components could be integrated with the sequencer to develop a lab-on-a-chip technology. A thorough review of the use of microfluidic devices in DNA sequencing, pathogen detection, gene expression analysis, and forensic repeat typing was performed in [19] by Liu and Mathies. The authors highlighted the importance of increased sensitivity, high speed, and enhanced reliability of integrated microsystems to address the challenges mentioned earlier. A review of present and future applications of microfluidics along with the potentials of lab-on-a-chip techniques for drug discovery have been done by Dittrich and Manz in [20]. The authors opine that microfluidic handling of fluid connections and small volumes could eventually overtake robotic fluid handling. Apart from that, surface per volume laws of scale, heat transport and molecular diffusion significantly increases the throughput in microscale though the nature of molecular reactions remains the same. Other than all the chemical and biological applications of microfluidics discussed till now, the technology finds extensive applications in heat transfer and cooling of integrated circuits. Hot spots and uneven thermal maps in integrated circuits result in performance

degradation and physical stress. These thermal management issues are becoming more and more important everyday with the decrease of size and increase of package densities in IC designs. In [21], the authors present a cooling method which relies on electrowetting manipulation of submicrolitre droplets. A flowrate feedback control was also proposed so that the heated areas receive more supply of droplets due to thermocapillarity.

As the current study mainly deals with novel bio-inspired micropumping strategies, an overview of studies of various microscale pumping techniques is given in this section. A seminal work on the review of micropumps was first performed by Laser and Santiago in [22]. After surveying the developments in microscale pumping devices over the past 25 years, the authors in the mentioned study provided a thorough and exhaustive reference for micropump researchers. Based on the functionalities, two main types of micropumps were considered i.e., displacement and dynamic. The displacement micropumps can be divided into three categories based on the type and nature of displacement i.e., reciprocating, rotary, and aperiodic. On the other hand, the types of dynamic pumps that have been included in the review are centrifugal, electrohydrodynamic, electroosmotic, magnetohydrodynamic, acoustic streaming, and special effects. Not only did the authors present a detailed picture of the working methodologies of these pumps, they also presented an extensive comparative analysis of the performance of all types of micropumps reported in literature till then (2004). Au et. al in their review paper [23] presented the design of microvalves and micropumps with a detailed analysis of their working mechanisms, advantages and limitations mainly for biomedical applications. Lai and Folch in [24] also presented the design and working principle of a monolithic PDMS based micropump with the capability of generating peristaltic flow using single control channel. A microvalve with a raised seat was also incorporated in their design to improve bonding reliability. The authors concluded that their design represented a substantial reduction in the real estate occupied by control line to operate a peristaltic

pump. A caterpillar locomotion-inspired micropump which was pneumatically actuated by a tear drop shaped membrane was presented by So et. al. in [25]. An elastomeric membrane was asymmetrically deformed and then executed a touch down motion on the bottom of the chamber, in response to a pressure caused the flow towards the tail of the chamber connected to an outlet. The investigation was performed computationally as well as experimentally. A set of 10 PDMS based three valve peristaltic micropumps were experimentally investigated in [26]. The variations in flow rate with cycle frequencies, actuation pressures, fluid viscosities, and design parameters were studied. The authors also presented a numerical as well as an analytically model which agreed with the experimental results. The maximum flow rate achieved by their models was  $7.5 \mu\text{L}/\text{min}$  which showed significant improvement compared to the reported highest value for that particular type of micropump. Unger et. al. used multilayer soft lithography to fabricate microfluidic valves and pumps in [27]. They built active microfluidic systems consisting of switching valves, on/off valves, and pumps entirely out of elastomer. Their models reduced the device areas while retaining other advantages of soft lithography such as biocompatibility, ease of fabrication, and rapid prototyping. Lastly, in [28] Thorsen, Maerkl, and Quake presented a design of high density microfluidic chips consisting of thousands of micromechanical valves and hundreds of chambers which can be addressed individually. They used these integrated microfluidic networks to fabricate an analog of a comparator array and a memory storage device.

The studies presented here are motivated by the hypothesized mechanisms that drive the flow in thousands of tracheal tubes which comprise the insect respiratory systems. Discrete or directional wall collapses in several regions of these tubes in response to the pressure exerted by a single abdominal contraction are presumed to be the main driving factors behind the transport of respiratory gases from the spiracles to the tissues and vice versa. Thus, a knowledge of the relevant literature about the insect respiratory system would help to put

the current study into perspective. The study by Westneat et. al. in [29] revealed rapid compression and expansion cycles in the tracheal tubes of head and thorax of a particular species of insect when viewed via synchrotron X-ray, which along with flow-through respirometry was used by Socha et. al. in [30] to visualize the respiration mechanism of ground beetle. The study which was aimed to find a correlation between tracheal compression and excurrent gas exchange concluded that the tracheal compression plays a major role in ventilation in respiratory system of insects. Aboelkassem and Staples in a number of studies ([31], [32], [33], [34]), presented an analytical as well as a computational model that investigated the flow inside trachea mimetic microfluidic channels and tubes where the main driving factors responsible for the flow are wall collapses with phase lags. Lastly Chatterjee and Staples in [35] studied the effects of slip boundary conditions on a microchannel flow driven by the same wall collapse mechanisms.

### 1.3 Contributions

In this thesis, the practical viability of incorporating some essential features and kinematics of insect respiratory system into mathematical models and practical microfluidic devices has been investigated. Though there has been considerable advancements and improvements in the complexity, size, and function of microfluidic devices over the last two decades, much work remains on determining how to simplify the associated actuation accessories that preferentially drive the flow in these devices. Since portability and miniaturization are two of the most important areas addressed by the microfluidic techniques, even a slight improvement or reduction in the actuation overhead of the pneumatically actuated microfluidic devices can be a major advancement in the technology. Though there has been a lot of research on microfluidic devices with different types of functionalities, little has been explored so far in

the field of insect-mimetic techniques. But insects are nature's testbed for applications of the most efficient fluid manipulations at the microscale which have become more sophisticated with evolutionary refinements. With the help of these superior respiratory mechanisms, insects are able to increase their metabolic activities drastically as and when required. A single abdominal contraction in some insects applies a pressure differential across thousands of tracheal tubes which then undergo localized contractions and relaxations. These compressions and relaxations of the tracheal tubes have been hypothesized to play a vital role in active ventilation in entomological respiratory systems. Two observed collapse phenomena: discrete and directional collapse of sections of the tracheal pathways have been modeled mathematically and incorporated into the design of experimental devices in the present study. In the devices, the actuation overhead was reduced by two-thirds from the current state-of-the-art microfluidic devices. The flow rate and direction in the devices could also be controlled by actuation frequency alone for a given actuation pressure, a feature never before realized in a valveless microfluidic device. Thus, the studies presented in each of the three chapters of this these could be the starting point for a novel field of insect-mimetic microfluidics.

In the first study, the effects of incorporating first order accurate slip boundary conditions have been mathematically tested for a flow in a two-dimensional rectangular microchannel driven by rhythmic wall collapses, without a pressure drop across the ends. These wall collapses are executed with a phase lag in their timing. It was found that in local pressure gradient dominated regions of the channel the magnitude of the axial velocity increased with increase in Knudsen number values; whereas in wall shear dominated regions the reverse happened. Also, the overall effect of incorporating slip boundary conditions in this wall contraction driven flow was to reduce the volumetric flow rate. Thus it might be possible that in the smallest of the tracheal tubes, slip boundary conditions slow down the flow rate thus acting as a diffuser.

In the second study the same rhythmic wall collapse driven flow was modeled in an axisymmetric microtube using first order accurate slip boundary conditions at the wall. Intratracheal pressure values taken from the entomology literature were used as pressure boundary conditions across the tube. Here also, it was found that increase of slip decreases the volumetric flow rate. But interestingly, there were some phase lag values for which there was a flow in the negative direction which means that a suitable combination of phase lag and pressure drop across the length of the tube can be chosen to drive the flow in the model tracheal pathway toward or away from the tissues.

In the third study fifteen insect respiratory system mimetic, single and multichannel microfluidic devices were designed, fabricated, and tested. These PDMS devices were able to generate a unidirectional flow by either discrete wall contractions or directional wall collapse of the fluid channel ceiling in response to a single distributed pressure signal. Apart from that, one of the single channel devices was able to reverse the direction of the flow based on just the actuation frequency alone for a given actuation pressure. Lastly, two of the multichannel devices were able to turn the flow in a particular channel on or off based on the actuation frequency alone. These features have never been realized before in a valveless microfluidic device. The results can be used to reduce the actuation overhead and subsequently the space required to operate pneumatically actuated complex microfluidic devices.

## 1.4 Research outline

The present thesis, as mentioned earlier, aims to address some of the actuation overhead problems encountered in current state of the art microfluidic devices by trying to mimic some of the key features of insect respiratory system.

The second chapter of this thesis, “Slip flow in a microchannel driven by rhythmic wall

contractions” investigates the effects of incorporating rarefaction effects into a flow in a microchannel driven by two rhythmic wall contractions with a time lag in between the collapses. The Navier-Stokes equations have been solved with microscale and lubrication theory assumptions and slip boundary conditions with zero pressure drop across the ends. Axial velocity, pressure gradient and static pressures have been plotted along the axial direction for two instances of time and three different values of the slip flow parameter starting from the no slip to the largest slip or the Knudsen number values. The volumetric flow rate was also plotted as a function of the time or the phase lags for different slip values. It was found that in local pressure gradient dominated regions, the magnitude of the axial velocity was directly proportional to the value of the slip flow parameter or the Knudsen number. Whereas in wall shear dominated regions, it was just the reverse. Apart from that, increase in the amount of slip decreased the volumetric flow rate over an entire contraction-relaxation cycle and the maximum flow rate occurred between  $63^\circ$  to  $67^\circ$ .

In the third chapter, entitled “Slip flow in a microtube driven by rhythmic wall collapses” the same type of wall collapse driven flow was modeled in a microtube with first order accurate slip boundary conditions in order to simulate the flow inside certain regions of the tracheal pathways where there are wall contractions as well as rarefaction effects. Physiologically realistic intratracheal pressure boundary condition data was obtained from the existing literature and used along with slip to solve the Navier-Stokes equations in cylindrical coordinates. The axial velocity, pressure gradient and static pressures were plotted along the tube axis for different values of slip at two different instances of time in the contraction relaxation cycle. The volumetric flow rate was plotted in the center of the tube for different values of the phase lag and for three different values of slip which spans the no slip as well as the largest slip conditions. Just like results from the second chapter, here also, the increase in the magnitude of slip increased the axial velocity at pressure gradient dominated regions

whereas the opposite happened in the wall shear dominated regions. Also, increase in slip decreased the volumetric flow rate over an entire cycle. One of the most interesting results obtained in this section was the existence of flows in the negative direction at very low and very high phase lag values. Thus it can be concluded that a suitable combination of phase lag and pressure difference can be used to generate forward as well as backward flows in the model respiratory tract.

The fourth chapter, entitled “Frequency-specific, single-actuation flow control in insect-mimetic valveless microfluidic devices” presents the results of the analysis of the performance of 15 insect mimetic microfluidic devices. Eleven single channel and four multichannel, PDMS based microfluidic devices were designed, fabricated, tested and analyzed. All the devices generated unidirectional flow as a result of discrete or directional collapse of the ceilings of the fluid channel in response to a periodic pressure pulse generated by a single source and then distributed in different areas over the devices. One of the devices was able to generate a bi directional flow in both the positive as well as the negative direction as a result of variation of actuation frequency. Apart from that, in two of the multichannel devices it was possible to control the flow rate in one of the channels again just by varying the frequency of the actuation or the pressure pulse. Also, a decent flow rate was generated by most of the devices and two of them were among the highest flow rate values obtained from existing literature for pneumatically actuated micropumps.

In the fifth and final chapter of this thesis, the work is summarized, and recommendations are made for possible future research directions on the topic of insect-inspired and insect-mimetic microfluidics.

# References

- [1] Sia, S. K., & Whitesides, G. M. (2003). Microfluidic devices fabricated in poly (dimethylsiloxane) for biological studies. *Electrophoresis*, 24(21), 3563-3576.
- [2] Ingber, D. E. (2016). Reverse engineering human pathophysiology with organs-on-chips. *Cell*, 164(6), 1105-1109.
- [3] Luni, C., Serena, E., & Elvassore, N. (2014). Human-on-chip for therapy development and fundamental science. *Current opinion in biotechnology*, 25, 45-50.
- [4] Maschmeyer, I., Lorenz, A. K., Schimek, K., Hasenberg, T., Ramme, A. P., Hübner, J., ... & Sambo, N. S. (2015). A four-organ-chip for interconnected long-term co-culture of human intestine, liver, skin and kidney equivalents. *Lab on a Chip*, 15(12), 2688-2699.
- [5] Huh, D. (2015). A human breathing lung-on-a-chip. *Annals of the American Thoracic Society*, 12(Supplement 1), S42-S44.
- [6] Stucki, A. O., Stucki, J. D., Hall, S. R., Felder, M., Mermoud, Y., Schmid, R. A., ... & Guenat, O. T. (2015). A lung-on-a-chip array with an integrated bio-inspired respiration mechanism. *Lab on a Chip*, 15(5), 1302-1310.
- [7] Kim, H. J., & Ingber, D. E. (2013). Gut-on-a-Chip microenvironment induces human intestinal cells to undergo villus differentiation. *Integrative Biology*, 5(9), 1130-1140.
- [8] Kim, H. J., Huh, D., Hamilton, G., & Ingber, D. E. (2012). Human gut-on-a-chip inhabited by microbial flora that experiences intestinal peristalsis-like motions and flow. *Lab on a Chip*, 12(12), 2165-2174.

- [9] Huh, D., Leslie, D. C., Matthews, B. D., Fraser, J. P., Jurek, S., Hamilton, G. A., ... & Ingber, D. E. (2012). A human disease model of drug toxicity-induced pulmonary edema in a lung-on-a-chip microdevice. *Science translational medicine*, 4(159), 159ra147-159ra147.
- [10] Huang, Y., Williams, J. C., & Johnson, S. M. (2012). Brain slice on a chip: opportunities and challenges of applying microfluidic technology to intact tissues. *Lab on a Chip*, 12(12), 2103-2117.
- [11] Park, J., Lee, B. K., Jeong, G. S., Hyun, J. K., Lee, C. J., & Lee, S. H. (2015). Three-dimensional brain-on-a-chip with an interstitial level of flow and its application as an in vitro model of Alzheimer's disease. *Lab on a Chip*, 15(1), 141-150.
- [12] Booth, R., & Kim, H. (2012). Characterization of a microfluidic in vitro model of the blood-brain barrier (BBB). *Lab on a Chip*, 12(10), 1784-1792.
- [13] Taylor, A. M., Rhee, S. W., Tu, C. H., Cribbs, D. H., Cotman, C. W., & Jeon, N. L. (2003). Microfluidic multicompartiment device for neuroscience research. *Langmuir*, 19(5), 1551-1556.
- [14] Maoz, B. M., Herland, A., FitzGerald, E. A., Grevesse, T., Vidoudez, C., Pacheco, A. R., ... & Budnik, N. (2018). A linked organ-on-chip model of the human neurovascular unit reveals the metabolic coupling of endothelial and neuronal cells. *Nature biotechnology*.
- [15] Park, J. W., Vahidi, B., Taylor, A. M., Rhee, S. W., & Jeon, N. L. (2006). Microfluidic culture platform for neuroscience research. *Nature protocols*, 1(4), 2128.
- [16] Mora, M. F., Greer, F., Stockton, A. M., Bryant, S., & Willis, P. A. (2011). Toward total automation of microfluidics for extraterrestrial in situ analysis. *Analytical chemistry*, 83(22), 8636-8641.

- [17] McClain, M. A., Culbertson, C. T., Jacobson, S. C., Allbritton, N. L., Sims, C. E., & Ramsey, J. M. (2003). Microfluidic devices for the high-throughput chemical analysis of cells. *Analytical chemistry*, 75(21), 5646-5655.
- [18] Kartalov, E. P., & Quake, S. R. (2004). Microfluidic device reads up to four consecutive base pairs in DNA sequencing-by-synthesis. *Nucleic acids research*, 32(9), 2873-2879.
- [19] Liu, P., & Mathies, R. A. (2009). Integrated microfluidic systems for high-performance genetic analysis. *Trends in biotechnology*, 27(10), 572-581.
- [20] Dittrich, P. S., & Manz, A. (2006). Lab-on-a-chip: microfluidics in drug discovery. *Nature Reviews Drug Discovery*, 5(3), 210.
- [21] Pamula, V. K., & Chakrabarty, K. (2003, April). Cooling of integrated circuits using droplet-based microfluidics. In *Proceedings of the 13th ACM Great Lakes symposium on VLSI* (pp. 84-87). ACM.
- [22] Laser, D. J., & Santiago, J. G. (2004). A review of micropumps. *Journal of micromechanics and microengineering*, 14(6), R35.
- [23] Au, A. K., Lai, H., Utela, B. R., & Folch, A. (2011). Microvalves and micropumps for BioMEMS. *Micromachines*, 2(2), 179-220.
- [24] Lai, H., & Folch, A. (2011). Design and dynamic characterization of “single-stroke” peristaltic PDMS micropumps. *Lab on a Chip*, 11(2), 336-342.
- [25] So, H., Pisano, A. P., & Seo, Y. H. (2014). Caterpillar locomotion-inspired valveless pneumatic micropump using a single teardrop-shaped elastomeric membrane. *Lab on a Chip*, 14(13), 2240-2248.

- [26] Goulpeau, J., Trouchet, D., Ajdari, A., & Tabeling, P. (2005). Experimental study and modeling of polydimethylsiloxane peristaltic micropumps. *Journal of Applied Physics*, 98(4), 044914.
- [27] Unger, M. A., Chou, H. P., Thorsen, T., Scherer, A., & Quake, S. R. (2000). Monolithic microfabricated valves and pumps by multilayer soft lithography. *Science*, 288(5463), 113-116.
- [28] Thorsen, T., Maerkl, S. J., & Quake, S. R. (2002). Microfluidic large-scale integration. *Science*, 298(5593), 580-584.
- [29] Westneat, M. W., Betz, O., Blob, R. W., Fezzaa, K., Cooper, W. J., & Lee, W. K. (2003). Tracheal respiration in insects visualized with synchrotron X-ray imaging. *science*, 299(5606), 558-560.
- [30] Socha, J. J., Lee, W. K., Harrison, J. F., Waters, J. S., Fezzaa, K., & Westneat, M. W. (2008). Correlated patterns of tracheal compression and convective gas exchange in a carabid beetle. *Journal of Experimental Biology*, 211(21), 3409-3420.
- [31] Aboelkassem, Y., & Staples, A. E. (2013). A bioinspired pumping model for flow in a microtube with rhythmic wall contractions. *Journal of Fluids and Structures*, 42, 187-204.
- [32] Aboelkassem, Y., & Staples, A. E. (2012). Flow transport in a microchannel induced by moving wall contractions: a novel micropumping mechanism. *Acta Mechanica*, 223(3), 463-480.
- [33] Aboelkassem, Y., & Staples, A. E. (2013). Stokeslets-meshfree computations and theory for flow in a collapsible microchannel. *Theoretical and Computational Fluid Dynamics*, 27(5), 681-700.

- [34] Aboelkassem, Y., & Staples, A. E. (2014). A three-dimensional model for flow pumping in a microchannel inspired by insect respiration. *Acta Mechanica*, 225(2), 493-507.
- [35] Chatterjee, K., & Staples, A. (2018). Slip flow in a microchannel driven by rhythmic wall contractions. *Acta Mechanica*, 1-17.

# Chapter 2

## Slip flow in a microchannel driven by rhythmic wall contractions

### Publication information

The contents of this chapter have been published as:

Chatterjee, K., & Staples, A. (2018). Slip flow in a microchannel driven by rhythmic wall contractions. *Acta Mechanica*, 1-17. <https://doi.org/10.1007/s00707-018-2210-7>

### 2.1 Abstract

We adopt a recent minimal mathematical model of a pumping mechanism in entomological respiratory systems and consider the model's behavior in the slip flow regime, which occurs naturally in the distalmost portions of insect respiratory systems. In the model, a phase lag in the timing of two neighboring wall contractions in a rectangular microchannel produces a unidirectional flow. The current study investigates the results of incorporating slip effects into the model by introducing first order accurate slip boundary conditions to investigate the method's performance for slip flows at the microscale in the slip flow regime. The two-dimensional Navier-Stokes equations are solved with microscale and lubrication theory assumptions, and the tangential momentum accommodation coefficient is assumed to be one, so that the slip flow parameter  $\beta$  is identically equivalent to the Knudsen number,  $Kn$ .

The variations of the axial velocity, pressure gradient, and total pressure along the channel are determined for three representative Knudsen numbers that span the continuum and slip flow regimes. It was observed that for the shear driven flow investigated here, the overall effect of increasing the amount of slip is to decrease the volumetric flow rate, and that the phase lag for producing maximum flow is in the range of  $63^\circ$  to  $67^\circ$ , while in the no-slip case the optimum phase lag is approximately  $63^\circ$ . The results suggest that shear driven flows at the microscale in the slip flow regime may see a reduction in flow rate in contrast to pressure driven microscale gas flows in the slip flow regime.

## 2.2 Introduction

Microfluidics is an important research area because of the versatility of its applications across disciplines ranging from molecular biology to medicine and microelectronics, including such critical applications as organs on a chip [29], bio assays with microfluidic networks used for targeted drug delivery [30], and high-performance liquid chromatography [31]. These sophisticated applications are possible because of the advances made in photolithography and silicon micromachining techniques. But current state-of-the-art microfluidic devices, comprised of complex networks of microchannels, often rely on the coordinated actuation of several different valves and micropumps in order to drive the flow in the desired direction in the network [32]. The fabrication and actuation of these devices can be complex and expensive, and they depend upon many different factors for their successful performance [33]. An inventive alternative mechanism for actuating fluid flows in microscale networks, presented by Aboelkassem *et al.* in [19], is the periodic and localized buckling of the microchannel wall with time lags between consecutive buckling sites, which results in controlled flow in the network by varying the channels' spatial hydraulic resistance profile with time while

imparting momentum to the fluid. The flow is precisely controlled by varying the geometry of each branch in the network and the single actuation input for the entire network, which each branch can respond to differently. Since many microscale flows involve slip, including the insect respiratory systems that inspired Aboelkassem *et al.*'s model, in this work we study the effects of rarefaction in Aboelkassem's model.

In the following paragraphs, we review some of the relevant previous work on shear-driven flows in channels, beginning here with macroscale flows driven by collapsing walls without slip at the boundaries. In [25, 26], the authors studied the linear stability of Poiseuille flow and the influence of boundary conditions on it, respectively. A similarity solution of the Navier-Stokes equations for viscous, unsteady, incompressible flow in a semi-infinite, contracting and expanding pipe was analytically derived in [2]. The effects of Reynolds number and viscosity on the nature of the flow at the contracting and expanding regions of the pipe were studied. The solutions derived were also valid for a completely collapsed pipe as the nonlinearity was retained in full. The flow of a viscous, incompressible fluid through long two-dimensional channels with parallel walls pulsating sinusoidally with small amplitudes was analytically studied in [3]. The flow was driven by wall collapse as well as an externally applied pressure. The relationship of the natural frequency of the system with that of the external oscillatory pressure was also studied. The squeezing, unsteady flow of an incompressible and viscous fluid between two rectangular or circular parallel plates approaching or receding from each other symmetrically was studied in [10] by numerically solving the ordinary differential equations obtained from full Navier-Stokes equations using a similarity transformation. Finally, the effects of a non-dimensional parameter, representing the relative importance of unsteadiness and viscosity, were studied analytically and numerically by solving full Navier-Stokes equations in [22] for the squeezing, unsteady flow of a viscous fluid through a tube whose radius varies with time.

A number of important studies on flow in channels driven by deformations of the channel wall propagating in the axial direction have been performed. The pumping of fluid by an infinite train of peristaltic waves of large wavelength, at low Reynolds number was analytically, numerically, and experimentally investigated in [23] as a model for flow in the ureter and the gastro-intestinal system for both plane and axisymmetric geometries and for different amplitude ratios. A backward reflux flow was found to exist near the periphery of the channel. The fluid mechanics of the duodenum and the effects of the wall movements on the absorption in intestine were studied in [14, 15], where the authors analytically modeled low Reynolds number flows driven by stationary, symmetric or peristaltic ring contractions. In another study, the behavior of an unsteady, viscous, incompressible flow in a channel due to a moving wall indentation was investigated [12]. In that study the Navier-Stokes equations were solved numerically and it was observed that eddies formed downstream of the indentation. Vorticity contours were also plotted, revealing the inviscid nature of the wave generation process. The transport of an incompressible, viscous fluid due to non-steady peristaltic sinusoidal waves in tubes of finite length was analytically studied in [8] using lubrication theory assumptions. In the same study the dependence of pumping performance and the fluctuations of pressure and shear stress on the nature and number of peristaltic waves were also examined. The effects of inertia and streamline curvature on the peristaltic pumping rate and shear stress levels for incompressible, Newtonian fluid flow in symmetric and asymmetric channels were studied analytically in [13]. It was seen that there were instances where the fluid flow was opposite to the direction of wave propagation, even for a favorable pressure gradient.

A substantial amount of research has been conducted on the effects of slip boundary conditions in microscale fluid flows. A pioneering work on pressure driven, gaseous slip flow at low Reynolds number, in long microchannels involving both experiments and computations was

performed by Arkilic *et al.* in [5]. The authors found the presence of both rarefaction and compressibility effects after solving the two-dimensional, time invariant Navier-Stokes equation with first order slip boundary conditions. These analytical solutions corresponded well with the experimental results. In [11] the author analytically investigated the entrainment of incompressible gases in a microtube, with the flow induced by surface wave propagation along the wall. The results showed the presence of back flows as well as some other complex flow patterns for smaller tube diameters. Both slip and magnetic field effects on the peristaltic transport of an incompressible, Newtonian fluid at low Reynolds number in an asymmetric microchannel were investigated both numerically and analytically in [17]. Additionally, the effects of a phase difference in the traveling waves, the Knudsen number, and the magnetic field strength on the pumping characteristics were discussed. In [16] the Navier-Stokes equations were analytically solved with second order accurate slip boundary conditions for pressure driven, steady and fully developed flows in long microchannels. It was shown that solutions were more accurate than when using first-order slip boundary conditions. The results were compared to those obtained from Boltzmann's equation and shown to be accurate up to a Knudsen number of 5. On the other hand, the analytical study in [4] revealed that the Navier-Stokes equations with slip boundary conditions are not sufficient to accurately model gaseous, steady and laminar fluid flow in the transition regime. A comprehensive review of various slip models for flow in microchannels with varying geometric features was presented in [6]. This review study demonstrated the sensitivity of microscale gas flows to cross sectional area, roughness, and channel curvature. Lastly in [21], the effects of the introduction of slip in a pressure-driven transient flow of an incompressible, Newtonian fluid in a microchannel with elastic walls were studied analytically. It was shown that the elastic behavior of the microtube coupled nonlinearly with the slip velocity, greatly enhancing the achievable flow rate.

Finally, in a series of articles Aboelkassem and colleagues put forth a mathematical model of the rhythmic, directional contractions that have been observed to occur in the tracheal tubes of insects [1, 18] and analyzed its efficiency as a pumping mechanism for fluid transport at the microscale. In [7, 9], Aboelkassem *et al.* modeled low-Reynolds number flow in a two-dimensional infinite channel driven by a simplified model of the tracheal wall contraction kinematics and demonstrated that it acted as a pumping mechanism. In [27], Aboelkassem and Staples performed Stokeslets-based meshfree computations of the system and verified the earlier theoretical results. In [19], Aboelkassem and Staples extended the single-channel approach of their earlier work to a network comprised of individual insect-inspired channels. In this work, they demonstrated that flow in such a network could be directed into specific branches of the network by simply changing the actuation frequency. In [20], Aboelkassem and Staples extended the model to circular cross-section channels. In [28], Aboelkassem and Staples presented three-dimensional meshfree computations and compared them to earlier results from the two-dimensional theory and computations.

As stated earlier, Aboelkassem's model is the basis for the analysis presented here. In our analysis, however, we extend the version of the model Aboelkassem and Staples presented in [7] to have both the lower and upper channel walls collapsing, and we use first-order slip boundary conditions at the channel walls rather than no-slip boundary conditions, thus investigating the effects of slip on this bioinspired pumping paradigm.

In the following sections, we present the model and analyze it. In Section 2.3, we present a schematic of the model geometry. In Section 2.4, Aboelkassem's two-dimensional mathematical model and our innovations to the model are presented. In Section 2.5 we present results for the axial velocity, pressure gradient, static pressure, streamlines, and volumetric flow rate for the model, and compare them at different values of the slip parameter. In Section 2.6, we make our concluding remarks.

## 2.3 Problem Schematic

The insect respiratory system is a complex network comprised of thousands of tubes. Following [7], in the present study we mathematically modeled a representative, simple, straight portion of a tube as highlighted in Fig. 2.1(a). Here, we have tried to analytically model fluid flow in the slip regime in insect tracheal tubes. For this purpose, we have chosen a simplified schematic of a straight microchannel and used slip boundary conditions and three different values of Kn which span the slip regime. The incompressible flow of a fluid in the infinite rectangular two-dimensional microchannel depicted in Fig. 2.1(c) is considered. The channel length,  $L$ , is assumed to be much greater than the height  $W$ , so that  $\delta \equiv W/L \ll 1$ . The symmetric lower and upper wall contraction profiles are composed of two discrete contraction sites located along the axial dimension  $x$  that contract periodically with time  $t$ . The contraction profiles of the lower and upper wall are described by  $H_1(x, t)$  and  $H_2(x, t)$ , respectively. For the present study, following [7] these mathematical functions have been chosen in such a way that when plotted, they closely resemble the shape of the contractions of the insect respiratory channels. These functions,  $H_1(x, t)$  and  $H_2(x, t)$  represent localized and non-peristaltic contractions at both the walls. The first wall contraction at location  $x_1$  may operate with a phase lag  $\theta_{12}$  with respect to the second wall contraction at location  $x_2$ . Fig. 2.1(b) shows the temporal parts,  $g_1(t)$  and  $g_2(t)$ , of the contractions in the upper wall with respect to time for a phase lag ( $\theta_{12}$ ) of  $30^\circ$ . Similarly, the spatial parts ( $f_i(x)$ ) of the wall collapse functions ( $H_1(x, t)$  and  $H_2(x, t)$ ) at  $t = T/4$  and  $\theta_{12} = 0^\circ$  are presented in the schematic diagram in Fig. 2.1(c). Expressions for the velocities in the channel in  $x$  and  $y$  directions are derived along with expressions for the pressure gradient and static pressure. The effects of different values of the phase lag and slip parameters on these fluid flow characteristics are investigated. Lastly, an optimal phase lag value is obtained for which there is a maximum volumetric flow rate,  $Q$ .

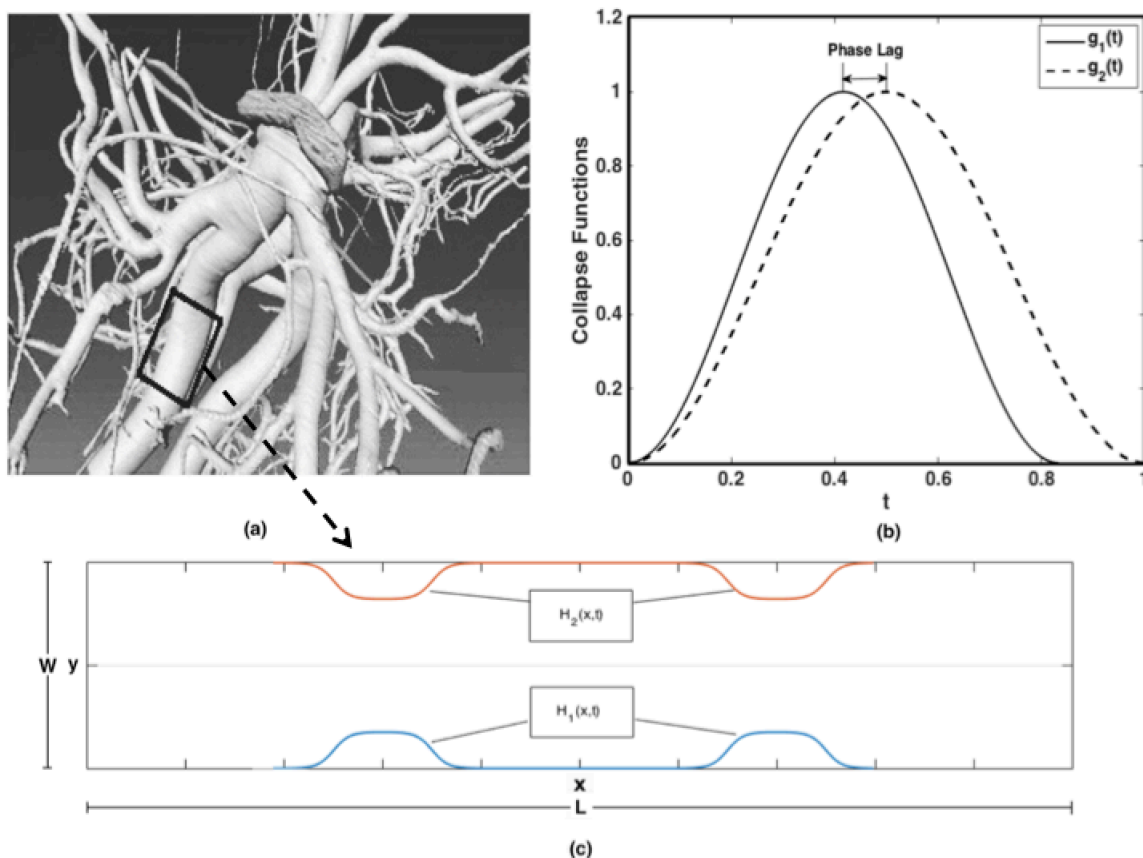


Figure 2.1: (a) 3D view of the tracheal system in the thorax of a carabid beetle (*Platynus decentis*) with a highlighted portion showing the part modeled here (reproduced with permission from [35]). (b) Time dependence of the upper wall collapse functions ( $g_1(t)$  and  $g_2(t)$ ). (c) Problem Schematic: 2D rectangular channel with moving lower wall contraction profile  $H_1(x,t)$  and upper wall contraction profile  $H_2(x,t)$ .

## 2.4 Mathematical Model

For our mathematical model we adopt Eqns. (4-6) of Aboelkassem and Staples [7]. The model considers the incompressible and isothermal flow of a Newtonian fluid with a constant viscosity in a two-dimensional rectangular channel with localized, non-peristaltic wall contractions, and uses lubrication theory and microscale assumptions. The velocity of the flow is assumed to be  $\mathbf{V} = (u, v, 0)$ , and the flow variables and parameters are nondimen-

non-dimensionalized in the following way:  $x = x^*/L$ ,  $y = y^*/W$ ,  $H_1 = H_1^*/W$ ,  $H_2(x, t) = H_2(x, t)^*/W$ ,  $t = t^*/(L/u_o)$ ,  $u = u^*/u_o$ ,  $v = v^*/\delta u_o$ ,  $p = p^*W^2/(\mu u_o L)$ ,  $\tau_{xy} = \tau_{xy}^*/(\mu u_o/W)$ ,  $Q = Q^*/(u_o W)$ ,  $St = fL/u_o$ ,  $Re = \rho u_o W/\mu$ , where  $\mu$  is the dynamic viscosity of the fluid,  $\rho$  is the fluid density,  $u$  and  $v$  are the horizontal ( $x$ ) and vertical ( $y$ ) components of the velocity,  $St$  and  $Re$  are the non-dimensional Strouhal and Reynolds numbers, and  $\tau_{xy}$ ,  $p$ , and  $Q$  are the wall shear stress, static pressure, and volumetric flow rate, respectively. The frequency and time scale of the symmetric contractions are given by  $f$  and  $T$ , respectively, and  $u_o$  is an arbitrary reference velocity, which can be any standard velocity in the flow regime of the channel. A possible choice of  $u_o$  that could be used to solve for the non-dimensional parameters is the velocity at the inlet. Given the model assumptions, the Navier-Stokes equations in two dimensions reduce to

$$\frac{\partial u}{\partial x} + \frac{\partial v}{\partial y} = 0 \quad (2.1)$$

$$-\frac{\partial p}{\partial x} + \frac{\partial^2 u}{\partial y^2} = 0 \quad (2.2)$$

$$\frac{\partial p}{\partial y} = 0. \quad (2.3)$$

Instead of the standard, no-slip boundary conditions used by Aboelkassem and Staples, in this work we use the following first-order slip boundary conditions

$$(i) \text{ at } y = 0, \frac{\partial u}{\partial y} = 0, v = 0$$

$$(ii) \text{ at } y = H_1(x, t), u = \beta \frac{\partial u}{\partial y}, v = \frac{\partial H_1}{\partial t}$$

$$(iii) \text{ at } y = H_2(x, t), u = -\beta \frac{\partial u}{\partial y}, v = \frac{\partial H_2}{\partial t}$$

$$(iv) \text{ at } x = 0, p = p_o(t)$$

$(v)$  at  $x = 1, p = p_L(t)$ .

The vertical velocity  $v$  in the  $y$  direction is set to zero because of the symmetric lower and upper wall contractions, which causes the  $y$  direction velocities generated due to lower and upper wall contractions to cancel each other at the mid-channel axis.  $\beta$  in the above equations is the slip flow parameter which is given by,  $\beta = Kn \frac{2-\sigma}{\sigma}$ , where  $\sigma$  is the tangential momentum accommodation coefficient and  $Kn$  is the Knudsen number. The Knudsen number is a dimensionless quantity which is defined as  $Kn = \frac{\lambda}{L}$ , where  $\lambda$  is the mean free path of the fluid molecules and  $L$  is a characteristic length scale. Here, the characteristic length scale is the channel height. The mean free path of a gas molecule can be calculated by the formula  $\lambda = \frac{RT}{\sqrt{2}\pi d^2 N_A P}$  where  $R$  is the universal gas constant,  $T$  is the temperature,  $d$  is the diameter of a single gas molecule,  $N_A$  is Avogadro's number and  $P$  is the pressure. For example, using this formula, the mean free path of a nitrogen molecule is  $5.9 \times 10^{-8}$  at a pressure of  $10^5$  Pa and a temperature of 275 K. Here, assuming the mean free path of air is fixed, the Knudsen number value gives an idea of the scale of the flow. Insect respiratory tracts span three distinct regimes starting from the spiracle, the entry to the respiratory tract, going toward the tissue. These three regimes can be distinguished from one another on the basis of Knudsen number, tract diameter, and the presence of slip and wall collapse. The relevant information for these regimes is presented in Table 1.

Regime	Knudsen Number ( $Kn$ )	Diameter ( $\mu m$ )	Slip ( <i>Yes/No</i> )	Collapse ( <i>Yes/No</i> )
1	0 - 0.001	500 - 60	No	Yes
2	0.001 - 0.1	60 - 25	Yes	Yes
3	0.001 - 0.1	25 - 1	Yes	No

Table 2.1: Relevant Knudsen number regimes through the insect respiratory system.

Integrating Eq. 2.2 twice with respect to  $y$  and using the above boundary conditions we

have the following expression for the horizontal velocity,  $u$

$$u(x, y, t) = \frac{1}{2} \frac{\partial p}{\partial x} [y^2 + \beta(H_1 - H_2) + H_1 H_2]. \quad (2.4)$$

Setting  $H_2 = +h$  and  $H_1 = -h$  in the above expression for  $u(x, y, t)$ , we get the same expression as Eq. 2.2 of [24]. Here we have assumed  $H_1 + H_2 = 0$  at any instant of time, because of the symmetric lower and upper wall contractions. The validity of this assumption has been verified by using the code.

From Eq. 2.4 we find an expression for the vertical velocity component  $v$  as follows

$$v(x, y, t) = \frac{1}{12} \frac{\partial^2 p}{\partial x^2} (V_1) + \frac{1}{12} \frac{\partial p}{\partial x} (V_2) \quad (2.5)$$

where,  $V_1 = -2y^3 - 6\beta H_1 y + 6\beta H_2 y - 6H_1 H_2 y$  and  $V_2 = -6\beta y \frac{\partial H_1}{\partial x} + 6\beta y \frac{\partial H_2}{\partial x} - 6H_2 y \frac{\partial H_1}{\partial x} - 6H_1 y \frac{\partial H_2}{\partial x}$ . The velocity stream function  $\psi(x, y)$  can be found by integrating  $u$  and  $v$  in the equations  $u = \frac{\partial \psi}{\partial y}$  and  $v = -\frac{\partial \psi}{\partial x}$ . The final expression for  $\psi(x, y)$  is as follows

$$\psi(x, y) = \frac{y}{2} \frac{\partial p}{\partial x} \left[ \frac{y^2}{3} + \beta (H_1 - H_2) + H_1 H_2 \right] \quad (2.6)$$

Applying boundary conditions (ii) and (iii) to Eq. 2.5 we obtain expressions for  $\frac{\partial H_1}{\partial t}$  and  $\frac{\partial H_2}{\partial t}$ . After subtracting the equations from one another and rearranging, we have the final partial differential equation as follows

$$\frac{\partial^2 p}{\partial x^2} = \frac{12}{-6\beta K^2 - 6LK - 2K(K^2 + 3L)} \left( \frac{\partial K}{\partial t} \right) - \frac{-6K \left( \beta \frac{\partial K}{\partial x} + \frac{\partial L}{\partial x} \right)}{-6\beta K^2 - 6LK - 2K(K^2 + 3L)} \left( \frac{\partial p}{\partial x} \right) \quad (2.7)$$

where  $K(x, t) = H_1 - H_2$  and  $L(x, t) = H_1 H_2$ .

The above equation is then solved numerically with the following boundary conditions at

$x = 0$ ,  $p = 0$  and at  $x = 1$ ,  $p = 0$ , to get expressions for  $\frac{\partial p}{\partial x}$  and  $\frac{\partial^2 p}{\partial x^2}$ . Thus the contractions are solely responsible for driving the flow and there is no pressure difference across the two ends of the channel. An expression for the volumetric flow rate can also be determined

$$Q(x, t) = \int_{H_1}^{H_2} u(x, y, t) dy. \quad (2.8)$$

Using Eq. 2.8 and performing the integration yields,

$$Q(x, t) = \frac{\partial p}{\partial x} \left[ \frac{1}{6} (H_2^3 - H_1^3 + 3H_1H_2^2 - 3H_1^2H_2) - \frac{1}{2}\beta (H_1 - H_2)^2 \right]. \quad (2.9)$$

Integrating the above equation over a complete time cycle we get the time averaged volumetric flow rate at any  $x$  location,  $Q_T(x)$ .

Given wall contraction functions  $H_1(x, t)$  and  $H_2(x, t)$  and slip parameter values, Eqns. 2.4 - 2.9 provide a complete description of the flow under study.

## 2.5 Results

The motions of the lower and upper channel walls are governed by the functions  $H_1(x, t)$  and  $H_2(x, t)$ . As discussed in Section 2.3 the walls undergo a complete cycle of collapse and re-expansion with or without a phase lag  $\theta_{12}$  between the motion of the two contraction sites. Though we have chosen specific values for the phase lag in different parts of this study, there is no reported consistent phase lag in insect respiratory systems. A complete contraction cycle takes place from  $t = 0$  to  $t = T$  with  $t = T/2$  being the point in time when the maximum contraction occurs. In general, we present results for two time instances, the first midway through the collapse half of the cycle at  $t = T/4$  and the other midway through the reexpansion half of the cycle at  $t = 3T/4$ . We assume values of  $L = 1$  and  $T = 1$  in

nondimensional units for our results; additionally, the first contraction starts at the location  $x = 0.25$  and spans a distance of 0.1, ending at  $x = 0.35$ . The second contraction starts at  $x = 0.65$ , spans a distance of 0.1, and ends at  $x = 0.75$ . We use three slip parameter values  $\beta = 0, 0.01, \text{ and } 0.1$ , which span the continuum and slip flow regimes. Generally, results are presented for two values of the phase lag parameter  $\theta_{12}$ , which are  $0^\circ$  and  $30^\circ$ , except for in Fig. 2.15, which includes the full range of possible phase lag values, from  $0^\circ$  to  $180^\circ$ . The following table presents the values of all the relevant parameters used in generating our results and in producing Figs. 2.3 - 2.15 (Table 2).

<i>Test</i>	<i>Figure</i>	<i>T</i>	$\theta_{12}$	$\beta$
1	3	$T/4$	$0^\circ$	0
2	4	$T/4, 3T/4$	$0^\circ$	0, 0.01, 0.1
3	5	$T/4, 3T/4$	$30^\circ$	0, 0.01, 0.1
4	6, 7, 8	$T/4$	$0^\circ$	0, 0.01, 0.1
5	9, 10, 11	$T/4$	$30^\circ$	0, 0.01, 0.1
6	12, 13, 14	$3T/4$	$30^\circ$	0, 0.01, 0.1
7	15	<i>N/A</i>	$0^\circ - 180^\circ$	0, 0.01, 0.1

Table 2.2: Values of parameters used in generating the plots in Figs. 2.3 - 2.15.

### 2.5.1 Channel wall profiles, $H_1(x, t)$ and $H_2(x, t)$

Following [7], we first assume general expressions for the channel wall profiles based approximately on the shape of contractions of the walls of the insect respiratory tracts as revealed by synchrotron X-ray imaging [18]. These expressions, functions of both time and space, are defined as

$$H_1(x, t) = -\frac{1}{2} + \sum_{i=1}^N A_i f_i(x) k_i(t) \quad (2.10)$$

$$H_2(x, t) = \frac{1}{2} + \sum_{i=1}^N A_i f_i(x) g_i(t) \quad (2.11)$$

where  $f_i(x) \in C^r [0, 1]$  and  $g_i(t) \in C^r [0, T = 1/St]$  represent the spatial and temporal variations of the lower and upper wall geometries. The spatially varying function that governs the wall contractions is

$$f_i(x) = \tanh(\alpha(x - x_i)) - \tanh(\alpha(x - (x_i + d_i))) \quad (2.12)$$

where  $\alpha = 2\pi/\delta$ ,  $x_i$  marks the starting point of the  $i$ th contraction and  $d_i \in (0, 1 - x_i]$  marks its extent along the  $x$  axis, as shown in Fig. 2.1(c). The temporal distribution of the first lower wall contraction,  $H_1(x, t)$ , is given by

$$k_1(t) = \begin{cases} \frac{1}{2} (-1 - \cos(2\pi t \beta_p St - \pi)), & 0 \leq t \leq 1/\beta_p St \\ 0 & 1/\beta_p St < t \leq 1/St \end{cases} \quad (2.13)$$

while that of the second contraction is given by

$$k_2(t) = \frac{1}{2} (-1 - \cos(2\pi t St - \pi)), \quad 0 \leq t \leq 1/St. \quad (2.14)$$

Similarly for the upper wall,  $H_2(x, t)$ , the temporal functions are given by

$$g_1(t) = \begin{cases} \frac{1}{2} (1 - \cos(2\pi t \beta_p St)), & 0 \leq t \leq 1/\beta_p St \\ 0 & 1/\beta_p St < t \leq 1/St \end{cases} \quad (2.15)$$

and

$$g_2(t) = \frac{1}{2} (1 - \cos(2\pi t St)), \quad 0 \leq t \leq 1/St. \quad (2.16)$$

The functions of  $x$  are identical for both the lower and the upper wall contractions upon reflection about the  $x$  axis.  $\beta_p$  is the non-dimensional phase lag parameter. It is related to the phase lag by the following equation,  $\theta_{12} = \pi(1 - 1/\beta_p)$ , where  $\theta_{12}$  is the phase lag between the first and the second contraction sites. The two contractions have the same time period  $T = 1/St = 1$  and for  $\beta_p = 1$  there is no phase lag between the contractions.

### 2.5.2 Model Validation

In order to validate our numerical calculations, we compare our computations with no-slip boundary conditions and contractions occurring on only the upper wall with the results for the same conditions in [7]. In [7], the maximum contraction amplitude of the upper wall is 70% of the total depth of the channel. In our double wall contraction case, with and without slip, we have chosen each of the upper and lower wall contractions to be 35% of the total depth of the channel, so that both the contractions of the upper and lower wall together cover 70% of the total depth in order to recover the same value for the volumetric flow rate as in [7]. In our study, we do not compare the flow rates for different wall collapse amplitudes (as in [7]). Here all the results except those presented in this validation section, have been obtained for 70% wall collapse (35% for each wall).

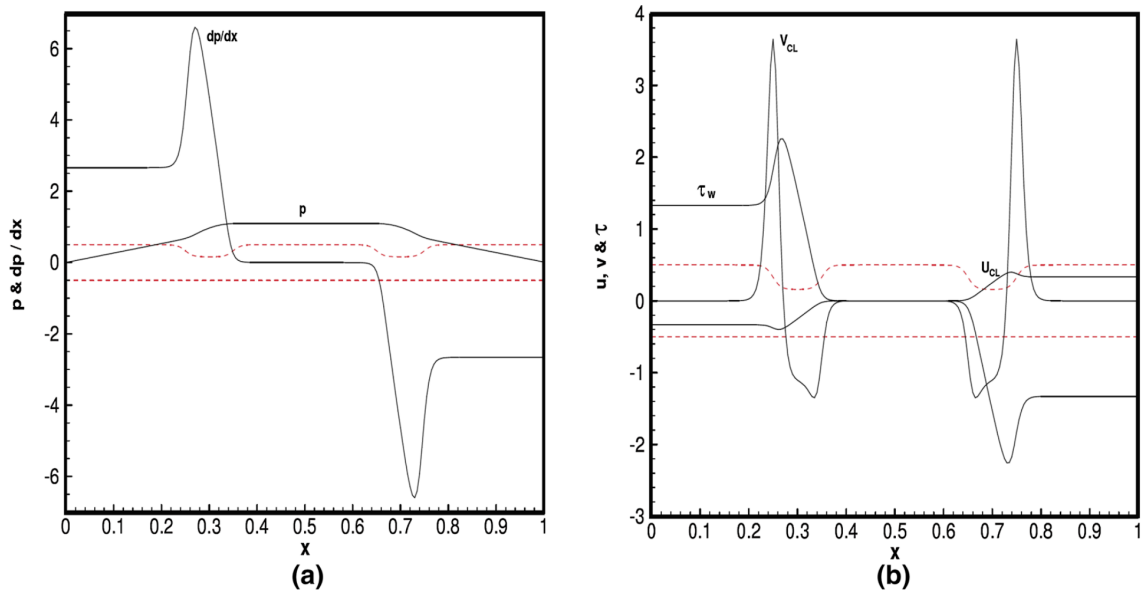


Figure 2.2: (a) Pressure gradient  $dp/dx$  and static pressure  $p$ . (b)  $u$  and  $v$  velocities for no-slip boundary conditions with single wall contractions at  $t = T/4$  and  $\theta_{12} = 0^\circ$ . The dashed lines represent the channel walls. From [7].

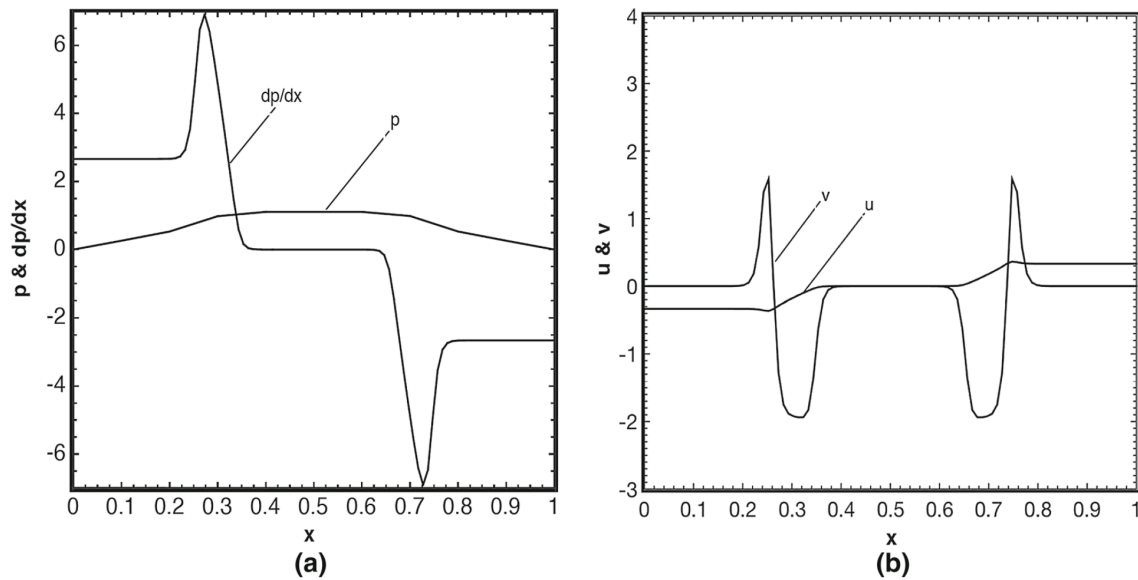


Figure 2.3: (a) Pressure gradient  $dp/dx$  and static pressure  $p$ . (b)  $u$  and  $v$  velocities for no-slip boundary conditions with single wall contractions at  $t = T/4$  and  $\theta_{12} = 0^\circ$ . The dashed lines represent the channel walls. Plots from present study.

Fig. 2.2a shows the variations of the pressure gradient and static pressure along the  $x$  direction from [7]. Fig. 2.3a shows the plots of the same quantities obtained using the current code, which are indistinguishable from those in Fig. 2.2a. In both cases, the pressure gradient profile at the first contraction shows a positive spike while there is a negative spike at the second contraction location. For positive  $u$ , the flow direction is from left to right. The positive pressure gradient in the  $x$  direction corresponds to flow towards the left and the negative pressure gradient corresponds to flow towards the right. Figs. 2.2b and 2.3b show the  $u$  and  $v$  velocities, comparing those from [7] with results produced by the current code. Similar to the pressure gradient plots, the  $u$  velocity also is negative in the first contraction region and then stays constant at zero value in the middle region and then again shows a positive value after the second contraction. The  $v$  velocity is symmetric and shows both positive and negative values at the contraction regions. Fig. 2.2b, obtained from [7] also shows the wall shear stress  $\tau_w$  plotted along the axis of the channel. But in the present work we are not concerned with the wall shear stress and focus on the variations of the axial velocity, pressure gradient, and static pressure. Both Figs. 2.2 and 2.3 are generated for the conditions of zero phase lag ( $\theta_{12} = 0^\circ$ ) between the contraction cycles for the first and second contractions, and for  $t = T/4$ , halfway through the compression phase of the contraction cycle. At this point in the cycle, the fluid flows symmetrically towards the left from the first contraction and towards the right from the second contraction, which ensures zero net axial flow. The flow is balanced in this way throughout the entire contraction cycle, resulting in zero net flow over an entire cycle.

### 2.5.3 Velocity and pressure

In order to investigate the flow behavior in the contracting microchannel and the effects of implementing slip boundary conditions, we plot the flow variables along the  $x$  axis at the

vertical position  $y = 0$ , which is at the center of the channel, as a function of  $\beta$ , the slip flow parameter. The tangential momentum accommodation coefficient (TMAC)  $\sigma$  provides information regarding the type of surfaces. TMAC can be expressed as a function of the tangential momentum of the incident ( $\tau_i$ ) and reflected ( $\tau_r$ ) molecules by the following relation:  $\sigma = \frac{\tau_i - \tau_r}{\tau_i}$ . Thus,  $\sigma = 1$  for fully diffused and 0 for fully specular surfaces. For most theoretical, numerical and engineering applications the value of  $\sigma$  is assumed to be 1 [5, 34]. Thus, in this study also we have assumed  $\sigma = 1$ . Using this value, consulting the following equation  $\beta = Kn \frac{2-\sigma}{\sigma}$  [5, 34], we see that  $\beta = Kn$ . Here, we have used three different slip parameter values that span the slip regime, as follows: no slip ( $\beta = 0$ ), low slip ( $\beta = 0.01$ ), and high slip ( $\beta = 0.1$ ). We consider these values to the the average Knudsen number value along the entire length of the channel, unlike some other studies on microchannel flows where the authors consider a local Kn along with the assumption that it varies along the length of the channel because of an externally applied pressure difference across the channel which drives flow. In the present study, the flow is shear-driven and so the Knudsen number has been assumed to be constant along the entire length of the channel, apart from local variations in response to the wall motions.

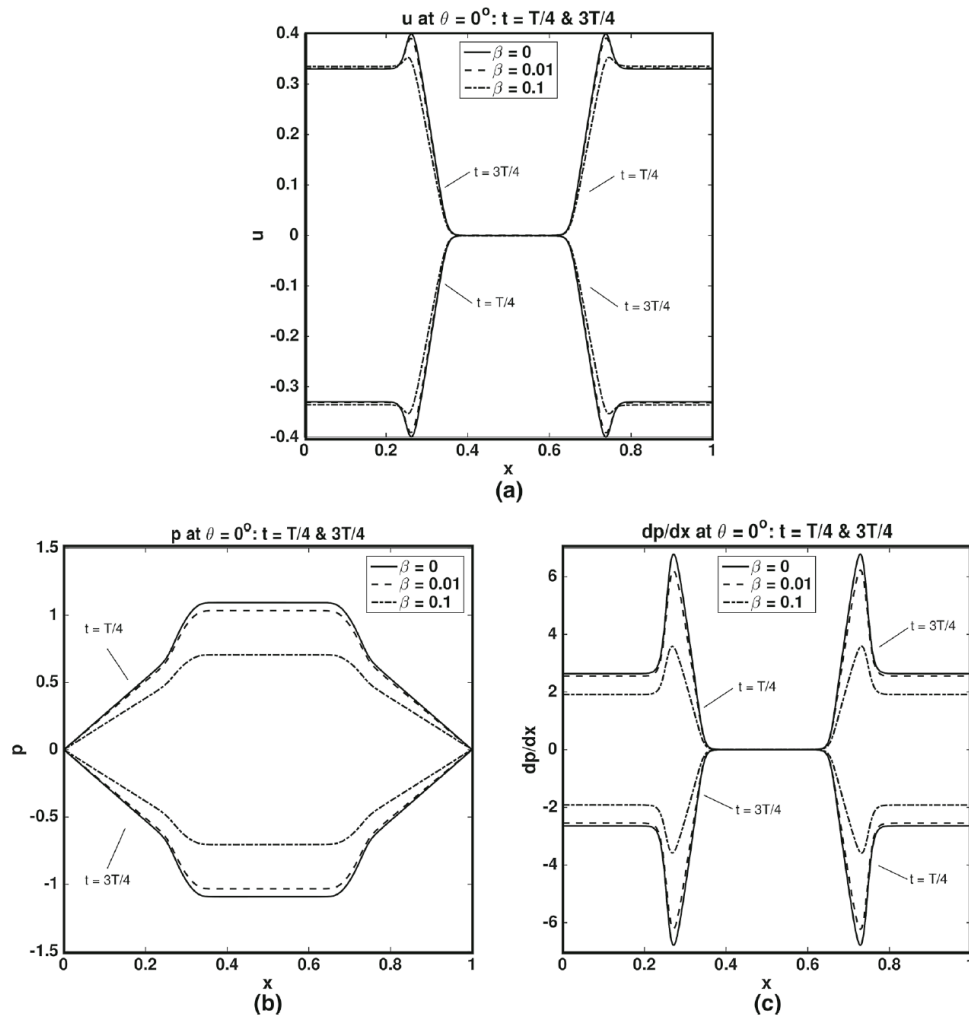


Figure 2.4: Comparison of  $u$ ,  $p$ , and  $dp/dx$  for  $\theta_{12} = 0^\circ$  at  $t = T/4$  and  $t = 3T/4$ . Three representative cases are shown: no slip ( $\beta = 0$ ), low slip ( $\beta = 0.01$ ) and high slip ( $\beta = 0.1$ ).

Fig. 2.4a shows the comparison of the  $u$  velocity profiles at the center line of the channel ( $y = 0$ ) for a phase lag of  $\theta_{12} = 0^\circ$  at  $t = T/4$  and  $t = 3T/4$ , two instances of time, one midway through the contraction half of the cycle, and the other midway through the relaxation half of the cycle. It can be seen that the two velocity profiles are exactly opposite at  $t = T/4$  and  $t = 3T/4$ . In fact, for  $\theta_{12} = 0^\circ$ , the axial velocity profiles for any two time instances separated by a phase of  $180^\circ$  during the contraction cycle mirror each other in this

way, indicating that there is no net flow in the positive direction over a complete contraction cycle. Also, we observe that the flow is towards the left from the first contraction and towards the right from the second contraction with a stagnation region in between. In Fig. 2.4a we see that the maximum velocity values, which occur at the contraction sites, are lower for higher values of the slip parameter and higher for lower values of the slip parameter. However, away from the contraction regions the opposite trend can be seen. This is because in the current study the fluid flow is driven by two different factors: (a) shear stress due to the wall motion, and (b) the local pressure gradient created by the wall motions. In the contraction regions, the flow is dominated by the wall shear stress, while away from the contraction regions, its effect decreases and the flow is dominated by the local pressure gradient generated due to the contractions. For shear driven flows, the fluid velocity decreases with increasing slip, while for pressure driven flows, the opposite is true. This is because the gripping effect of the wall on the adjacent as well as the subsequent layers of fluids, decreases with the increase in slip. In Figs. 2.4b and 2.4c we show the static pressure and the pressure gradient, respectively, at  $t = T/4$  and  $t = 3T/4$ . Again we see that the graphs are symmetric and opposite to each other, as expected for the  $0^\circ$  phase lag case. At  $t = T/4$ , there is a positive pressure gradient in the first contraction region and a negative pressure gradient in the second contraction region, which indicates a flow towards the left from the first contraction and towards the right from the second contraction. There is a zero pressure gradient region between the two contraction sites where there is no flow.

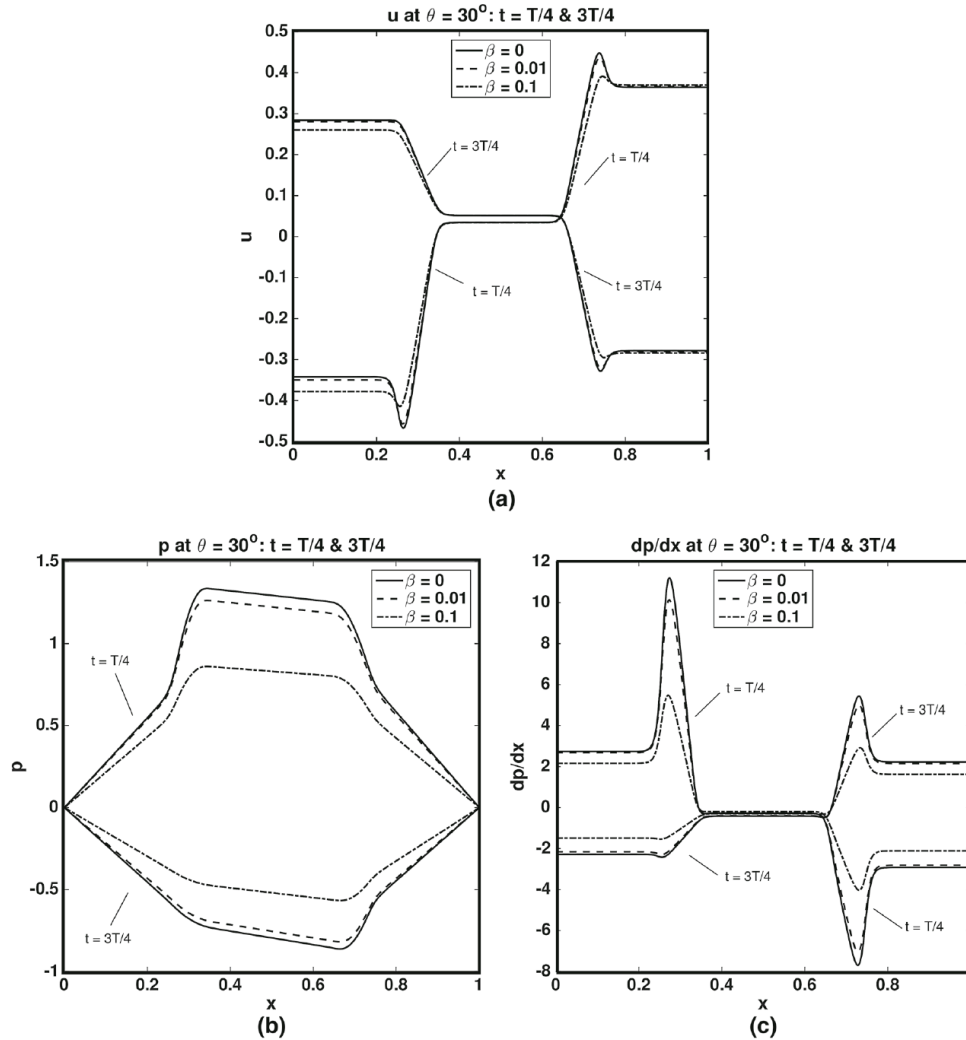


Figure 2.5: Comparison of  $u$ ,  $p$ , and  $dp/dx$  for  $\theta_{12} = 30^\circ$  at  $t = T/4$  and  $t = 3T/4$ . Three representative cases are shown: no slip ( $\beta = 0$ ), low slip ( $\beta = 0.01$ ) and high slip ( $\beta = 0.1$ ).

Fig. 2.5a shows the comparison of the axial velocity profiles at  $t = T/4$  and  $t = 3T/4$ , when there is phase lag of  $30^\circ$  in the timing of the two contraction cycles. In this case, the velocity profiles are not symmetric opposites in the two cases. This asymmetry in the plots between the collapse and relaxation phases indicates a net flow over an entire cycle. It can be seen from Fig. 2.5a that the magnitude of the axial velocity is non-zero in the region between the contractions, which means that, in this case, the flows from the two contraction regions

traveling towards the central region do not cancel each other and the stagnation region seen in the  $0^\circ$  phase lag case, is absent. Thus, there is a net unidirectional flow towards the positive direction or from left to right. Similarly, asymmetric behavior is also seen in Figs. 2.5b and 2.5c, where the static pressure and the pressure gradients are plotted along the channel axis. All the plots at  $t = T/4$  are significantly different from those at  $t = 3T/4$ . Though, as seen earlier in the  $0^\circ$  phase lag case, here too, the magnitude of the axial velocity decreases with increasing slip ( $\beta$ ) values in the wall contraction regions while the reverse happens away from the contraction regions. Recalling our earlier explanation that in the wall-shear driven regions of flow field, the axial velocity decreases with increase of slip values, whereas in the regions dominated by the local pressure gradient the velocity increases with increase in slip, we note that when the wall contractions are high enough in magnitude, the pressure gradient generated by them is also high and thus it can take over as the main driving factor in some regions of the flow domain, and vice versa. This explains the behavior we see in the upper left hand side of Fig. 2.5a. at  $t = 3T/4$ . Here, at the first contraction region, the wall contraction is very low in magnitude, as is evident from the streamline plots shown in Figs. 2.12, 2.13 and 2.14. Thus, the pressure gradient generated due to the wall contraction is very weak and is not enough to take over as the main driving factor of the fluid flow away from the contraction regions. Therefore, we can see that this region exhibits the trend seen in case of wall shear driven flows that is, decrease in the magnitude of axial velocity with increase in the value of slip. Different phase lag values produce different amounts of unidirectional flow which will be addressed in subsequent sections. For the time being we can conclude that a phase or time lag between two consecutive channel wall contractions is necessary to maintain an unidirectional flow in the channel and that the axial velocity can be varied by changing the slip parameter,  $\beta$ .

### 2.5.4 Comparison of streamlines

**Streamlines for three different slip values ( $\beta = 0, 0.01, 0.1$ ) at  $t = T/4$  and  $\theta_{12} = 0^\circ$**

Figs. 2.6, 2.7 and 2.8 show the streamlines within the channel for the three different slip parameter values at  $t = T/4$  for  $0^\circ$  phase lag. It can be seen that the fluid flows towards the left from the first contraction site and towards the right from the second contraction site. Thus, there is no flow in the space between the contractions due to cancellation of flows from both sides, and a stagnation region is created. The flow is also symmetric along the central axis (shown as a dotted line) of the channel at  $y = 0$ . There are some differences in the flow patterns between the high slip case and the other two slip values. For the high slip value ( $\beta = 0.1$ ), the streamlines are densely packed near the walls to the left of the first contraction and to the right of the second contraction, indicating higher velocity values at the wall region compared to the low slip cases. This can be verified visually by counting the number of streamlines above a certain point along the channel depth. For example the number of streamlines to the left of the first contraction above the mark  $y = 0.4$  are 2, 3 and 5 for the cases  $\beta = 0$ ,  $\beta = 0.01$  and  $\beta = 0.1$  respectively.

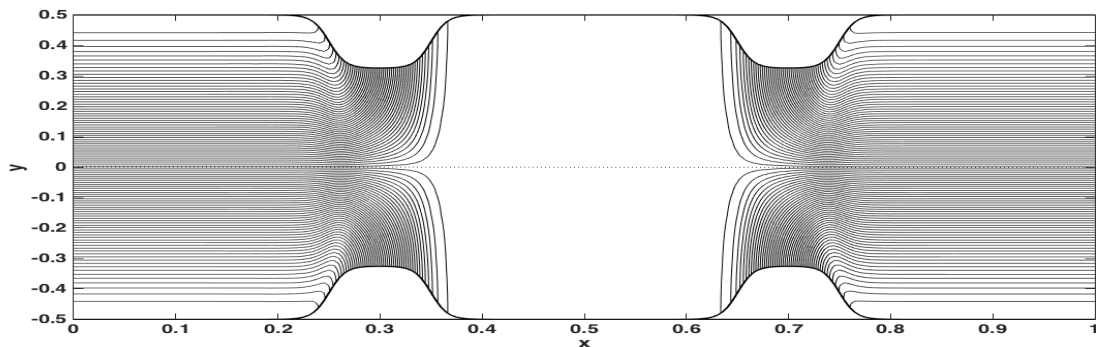


Figure 2.6: Streamlines for no slip ( $\beta = 0$ ) at  $t = T/4$  and  $\theta_{12} = 0^\circ$ .

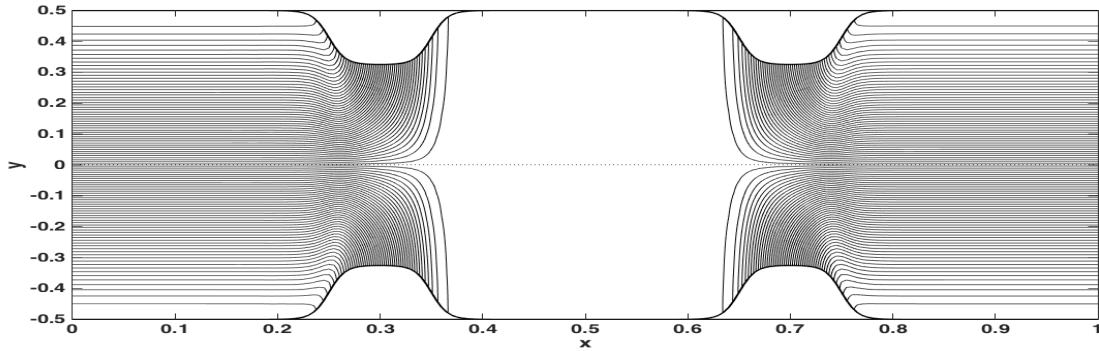


Figure 2.7: Streamlines for low slip ( $\beta = 0.01$ ) at  $t = T/4$  and  $\theta_{12} = 0^\circ$ .

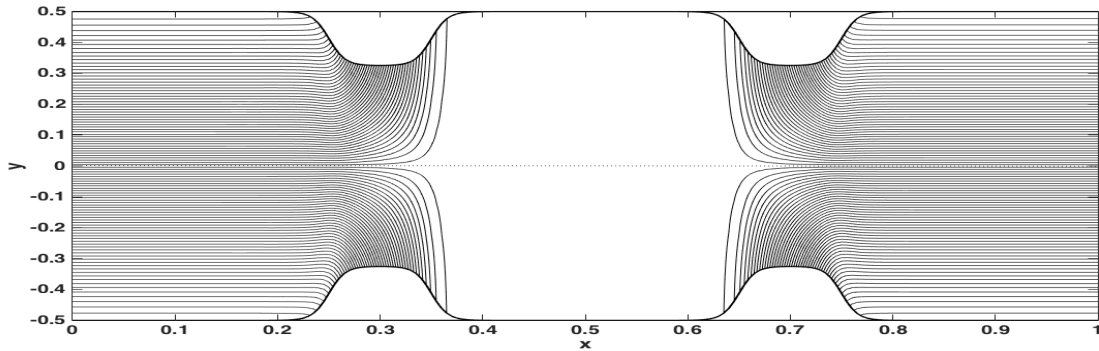


Figure 2.8: Streamlines for high slip ( $\beta = 0.1$ ) at  $t = T/4$  and  $\theta_{12} = 0^\circ$ .

### Streamlines for three different slip values ( $\beta = 0, 0.01, 0.1$ ) at $t = T/4$ and $\theta_{12} = 30^\circ$

Figs. 2.9, 2.10 and 2.11 show the streamlines for the three slip values at  $t = T/4$  with a  $30^\circ$  phase lag between the two wall contraction timings. The amplitudes of the first and second contractions are not the same at this point in the contraction cycle and as a result there is fluid flow in the region between the contractions. As before, this asymmetry results in a net unidirectional flow, towards the right in this case. As in the  $0^\circ$  phase lag scenario, some differences in the fluid flow patterns are visible between the three slip cases. As before, the streamlines are more densely packed at the wall away from the contractions and central zone between the contractions for the high-slip case. This can be again verified visually

by counting the number of streamlines to the left of the first contraction above the point  $y = 0.4$ , which are 2, 3 and 5 for the cases  $\beta = 0$ ,  $\beta = 0.01$  and  $\beta = 0.1$ , respectively. In the central zone, however, the opposite is true: for the high slip case, the streamlines are visibly less dense in the central region than that for the two low-slip cases, indicating a relatively lower velocity. This can be verified by counting the number of streamlines above or below the point  $y = 0$  (central axis), which are 5, 5 and 4 for the cases  $\beta = 0$ ,  $\beta = 0.01$  and  $\beta = 0.1$  respectively. This behavior suggests that the dominant force driving the flow differs in the two regions of the channel: in the contraction region (including the central zone between the contractions) the flow appears to be driven mainly by the wall motions, while outside the contraction region, the transient pressure gradients appear to be the main flow driver. At the instant of time shown in these figures the flow is both towards the left and right from the first contraction and only towards right from the second contraction.

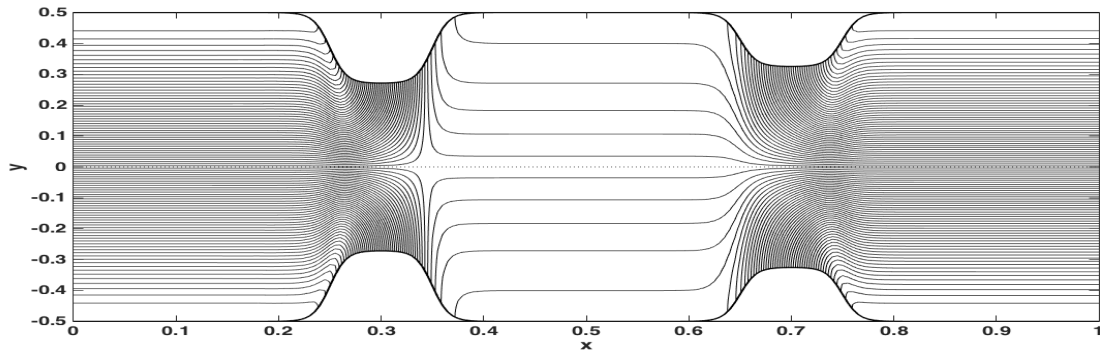


Figure 2.9: Streamlines for no slip ( $\beta = 0$ ) at  $t = T/4$  and  $\theta_{12} = 30^\circ$ .

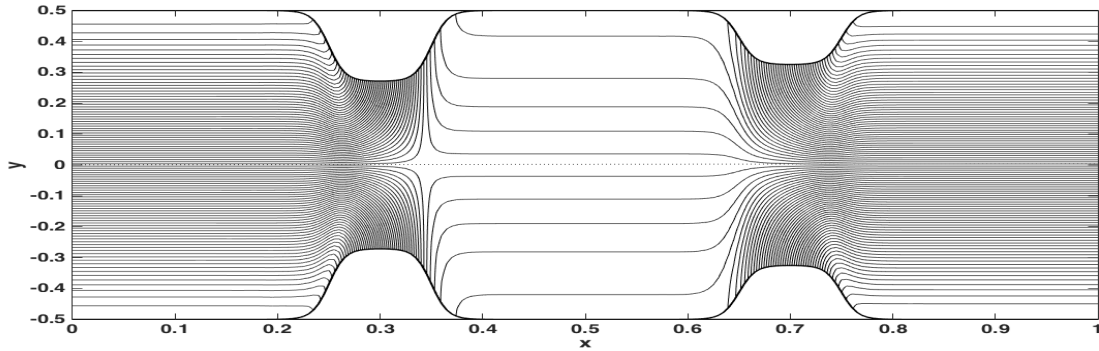


Figure 2.10: Streamlines for low slip ( $\beta = 0.01$ ) at  $t = T/4$  and  $\theta_{12} = 30^\circ$ .

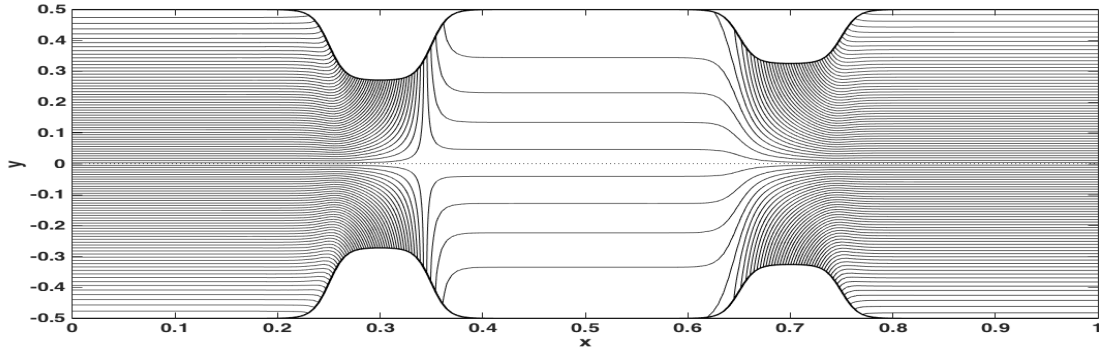


Figure 2.11: Streamlines for high slip ( $\beta = 0.1$ ) at  $t = T/4$  and  $\theta_{12} = 30^\circ$ .

**Streamlines for three different slip values ( $\beta = 0, 0.01, 0.1$ ) at  $t = 3T/4$  and  $\theta_{12} = 30^\circ$**

Figs. 2.12, 2.13 and 2.14 show the velocity streamline plots for the three slip parameter values at  $t = 3T/4$  for  $30^\circ$  phase lag between the contractions. The main notable features in these plots are the differences in the contraction amplitudes from those at  $t = T/4$ . The density of streamlines and hence flow rate in the central region between the contractions is much higher than that at  $t = T/4$ , highlighting the pulsatile nature of the flow. This is evident from the fact that the number of streamlines above or below the point  $y = 0$  (central axis) are 9, 9, and 9 for the cases  $\beta = 0$ ,  $\beta = 0.01$ , and  $\beta = 0.1$  respectively. Also, as

in the previous two cases, the number of streamlines near the wall, to the left of the first contraction and above the point  $y = 0.4$  are 2, 3 and 5 for the three cases  $\beta = 0$ ,  $\beta = 0.01$  and  $\beta = 0.1$  respectively.

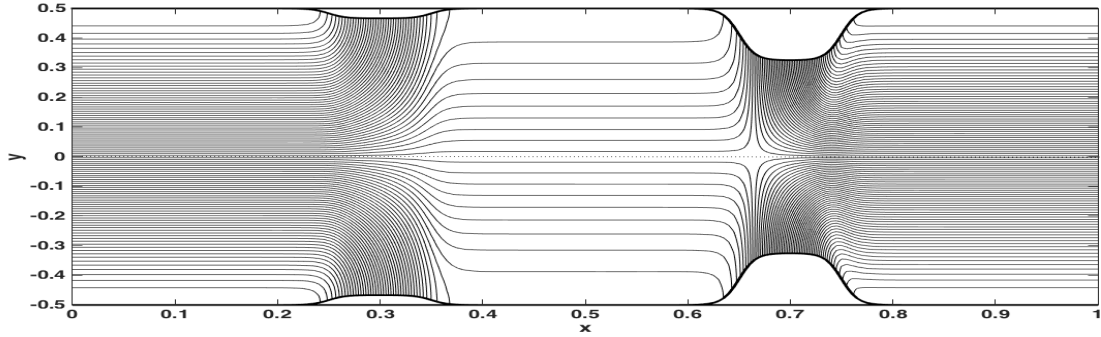


Figure 2.12: Streamlines for no slip ( $\beta = 0$ ) at  $t = 3T/4$  and  $\theta_{12} = 30^\circ$ .

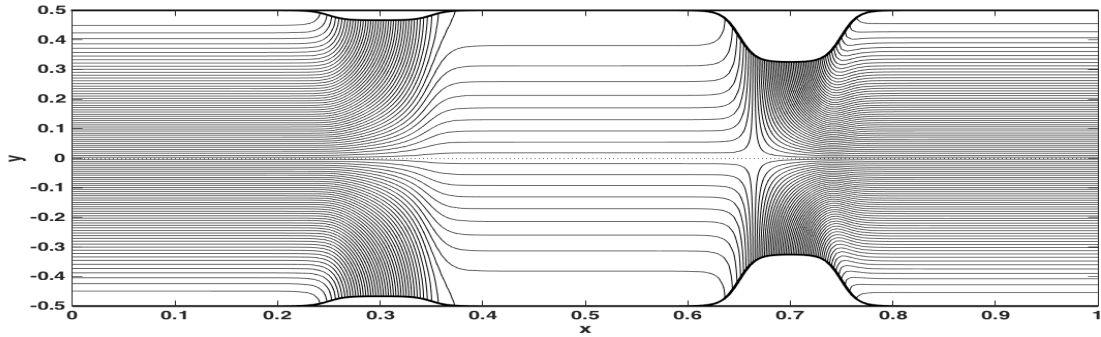


Figure 2.13: Streamlines for low slip ( $\beta = 0.01$ ) at  $t = 3T/4$  and  $\theta_{12} = 30^\circ$ .

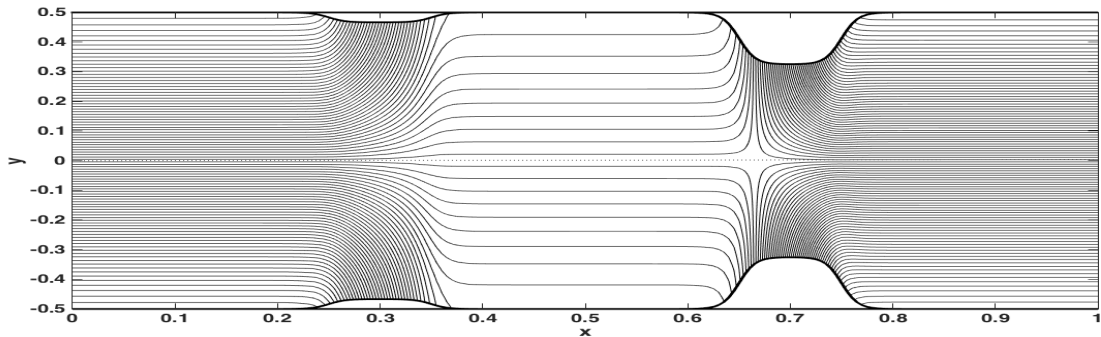


Figure 2.14: Streamlines for high slip ( $\beta = 0.1$ ) at  $t = 3T/4$  and  $\theta_{12} = 30^\circ$ .

### 2.5.5 Net flow produced

The effect of the phase lag values on the net volumetric flow rate in the positive  $x$  direction is studied in this section. The objective of this study is to investigate the possibility of using this novel fluid flow actuation mechanism in a channel with zero pressure drop across its ends. In order to determine the time averaged net flow we need to integrate the instantaneous flow rate over a complete contraction cycle as follows

$$Q_T(x) = \frac{1}{T} \int_0^T Q(x, t) dt \quad (2.17)$$

where,  $T = 1/St = 1$  is the time period. The value of  $Q_T(x)$  has been plotted in Fig. 2.15 for different phase lag values at a location of  $x = 0.5$ , for the three different slip parameter values considered in this study.

Fig. 2.15 compares the time averaged net flow rate plotted as a function of phase lag for the three values of the slip flow parameter  $\beta$ . It can be seen that the volumetric flow rate decreases with increasing slip. This is in agreement with the results of previous studies where the authors have investigated the variations of the volumetric flow rate with slip boundary conditions for a pressure driven flow, for example, in [16], where the volumetric flow rate decreases with an increase in the Knudsen number through the slip and transitional regimes until a value of  $Kn = 1$  is reached, where it is at a minimum. After that, the flow rate starts increasing in the free molecular flow regime.

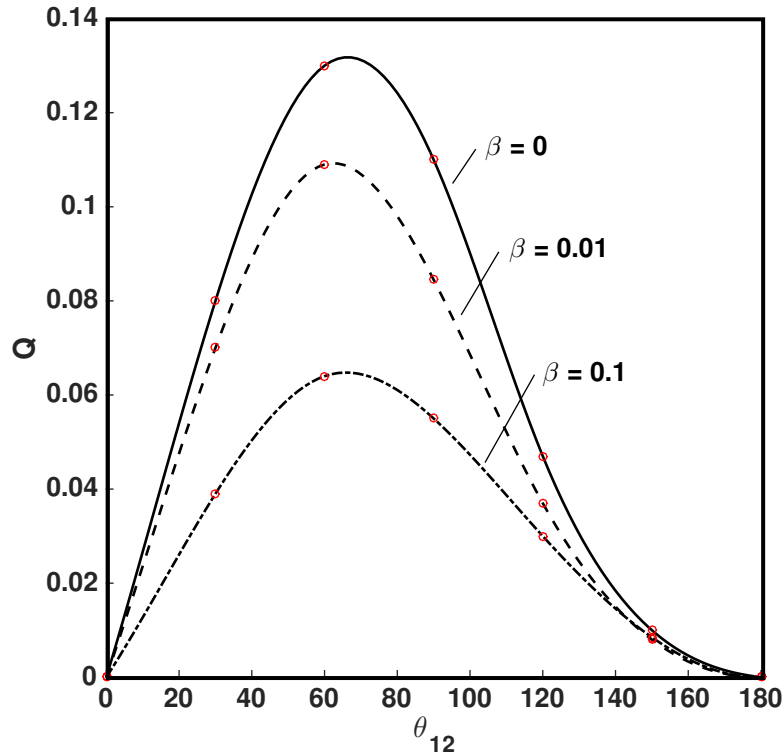


Figure 2.15: Time averaged net flow rate plotted for different phase lag values over an entire cycle at  $x = 0.5$ . Three cases are shown: no slip ( $\beta = 0$ ), low slip ( $\beta = 0.01$ ) and high slip ( $\beta = 0.1$ ). The circles on the plots represent the data points from calculations using Eq. 2.9. The solid and dashed curves are cubic splines fit to the calculated points in order to demonstrate the trend of the calculations.

It can be seen from Fig. 2.15, that the peak flow rate value for the high slip case is about half the corresponding value for the no-slip case. It can also be seen that the range of phase lag which produces the maximum flow is between  $63^\circ$  and  $67^\circ$  in both slip cases, which is close to the no-slip optimum phase lag value of  $63^\circ$ . The flow rate starts from zero at  $0^\circ$  phase lag and increases until  $60^\circ$  to  $70^\circ$  where it reaches a maximum, and then again starts decreasing and becomes zero again at  $180^\circ$  phase lag. Interestingly, while the maxima for the no slip and high slip cases are almost identical (around  $66.5^\circ$ ), the maximum for the low slip value is at about  $63^\circ$ , about  $3.5^\circ$  lower.

## 2.6 Conclusions

In this study the Navier-Stokes equations have been solved within microscale and lubrication theory approximations to derive the pressure gradient and the axial velocities of fluid flow in a microchannel driven by symmetric, non-peristaltic lower and upper wall contractions at two different axial locations in the slip flow regime. The contractions in the lower and upper channel walls are spatially symmetric upon reflection over the channel ( $x$ ) axis, and are inspired by contractions observed in entomological respiratory systems. The model used here was validated against the single wall contraction, no-slip results presented in [7]. First-order accurate slip boundary conditions were implemented and three different values of the slip flow parameter were used, representing no slip, and the minimum and maximum slip parameter values bounding the slip flow regime. The effects of introducing slip boundary conditions on the fluid flow were studied. Different phase lag values between the two contraction cycles and their effects on the fluid flow were studied. The time averaged fluid flow rate over an entire contraction cycle was computed for several different phase lag values, and the optimum phase lag value was found to be in the range of approximately  $63^\circ$ - $66.5^\circ$ . Thus, the phase lag between the contractions can be manipulated to vary the amount of net flow. It was observed that for the regions of the flow dominated by wall shear stress, the magnitude of the axial velocity decreases with an increase in the value of the slip flow parameter. But for regions dominated by the local pressure gradient the reverse trend is seen, the magnitude of the axial velocity increases with the increase in the value of the slip flow parameter. In spite of these local differences in response to slip boundary conditions, the overall result of adding slip in this study was to reduce the net volumetric flow rate compared to the no-slip case. Interestingly this result is in contrast to that obtained using slip boundary conditions for pressure driven flows (e.g. [36]). An exciting future investigation could be to compute flows in a very long channel so that the portion of the channel that is dominated by

wall shear stresses is very small compared to the rest of the channel. Another study could be to investigate the effect of slip boundary conditions on a flow driven by axisymmetric contractions in a microtube with a circular cross section, which is closer to the insect tracheal tubes whose contractions inspire this study.

# References

- [1] Socha, J.J., Lee, W.K., Harrison, J.F., Waters, J.S., Fezzaa, K., Westneat, M.W.: Correlated patterns of tracheal compression and convective gas exchange in a carabid beetle. *J. Exp. Biol.* **211**, 3409-3420 (2008)
- [2] Uchida, A. Aoki, H.: Unsteady flows in a semi-infinite contracting or expanding pipe. *J. Fluid Mech.* **82**, 371-387 (1977)
- [3] Secomb, T.W.: Flow in a channel with pulsating walls. *J. Fluid Mech.* **88**, 273-288 (1978)
- [4] Zhang, T., Jia, L., Wang, Z.: Validation of Navier-Stokes equations for slip flow analysis within transition region. *Int. J. Heat and Mass Trans.* **51**, 6323-6327 (2008)
- [5] Arkilic, E.B., Schmidt, M.A.: Gaseous slip flow in long microchannels. *J. Microelectromech. Syst.* **6**(2) (1997)
- [6] Agrawal, A.: A comprehensive review on gas flow in microchannels. *Int. J. Micro-Nano Sc. Trans.* **2**(1), 1-40 (2011)
- [7] Aboelkassem, Y., Staples, A.E.: Flow transport in a microchannel induced by moving wall contractions: a novel micropumping mechanism. *Acta Mech.* **223**, 463-480 (2012)
- [8] Meijing, L., Brasseur, J.G.: Non-steady peristaltic transport in finite-length tubes. *J. Fluid Mech.* **248**, 129-151 (1993)
- [9] Aboelkassem, Y., Staples, A.E., Socha, J.J.: Microscale flow pumping inspired by rhythmic tracheal compressions in insects. In: *Proc. ASME Press. Vessels Piping Conf., PVP2011*, 57061 (2011)

- [10] Singh, P., Radhakrishnan, V., Narayan, K.A.: Squeezing flow between parallel plates. *Ingenious Arch.* **60**, 274-281 (1990)
- [11] Kwang-Hua Chu, A.: Transport control within a microtube. *Phys. Rev. E* **70**, 061902 (2004)
- [12] Ralph, M.E., Pedley, T.J.: Flow in a channel with moving indentation. *J. Fluid Mech.* **190**, 87-112 (1988)
- [13] Ramachandra Rao, A., Mishra, M.: Nonlinear and curvature effects on peristaltic flow of a viscous fluid in an asymmetric channel. *Acta Mech.* **168**, 35-59 (2004)
- [14] Macagno, E.O., Christensen, J.: Fluid mechanics of the duodenum. *Ann Rev. Fluid Mech.* **12**, 139-158 (1980)
- [15] Macagno, E.O., Christensen, J., Lee, L.: Modeling the effect of wall movement on absorption in the intestine. *Am. J. Physiol.* **243**, G541-G550 (1982)
- [16] Dongari, N., Agarwal, A.: Analytical solution of gaseous slip flow in long microchannels. *Int. J. Heat Mass Transfer* **50**, 3411-3421 (2007)
- [17] Ebaid, A.: Effects of magnetic field and wall slip conditions on the peristaltic transport of a newtonian fluid in an asymmetric microchannel. *Phys. Lett. A.* **372**, 4493-4499 (2008)
- [18] Westneat, M.W., Betz, O., Blob, R.W., Fezzaa, K., Cooper, W.J., Lee, W.K.: Tracheal respiration in insects visualized with synchrotron X-ray imaging. *Science* **299**, 558-560 (2003)
- [19] Aboelkassem, Y., Staples, A.E.: Selective pumping in a network: Insect-style microscale flow transport. *Bioinspir. Biomim.* **8**, 026004 (2013)

- [20] Aboelkassem, Y., Staples, A.E.: Bioinspired pumping model for flow in a microtube with rhythmic wall contractions. *J. Fl. Str.* **42**, 187-204 (2013)
- [21] San, O., Staples, A.E.: Dynamics of pulsatile flows through elastic microtubes. *Int. J. Appl. Mechanics.* **04** 1250006 (2012)
- [22] Skalak, F.M., Wang, C.Y.: On the unsteady squeezing of a viscous fluid from a tube. *J. Aust. Math. Soc. (Series B)* **21**, 65-74 (1979)
- [23] Shapiro, A.H., Jaffrin, M.Y., Weinberg, S.L.: Peristaltic pumping with long wavelengths at low Reynolds number. *J. Fluid. Mech.* **37**, 799-825 (1969)
- [24] Tretheway, D.C., Liu, X., Meinhart, C.D.: Analysis of slip flow in microchannels. In: *Proc. 11th Inter. Symp. Appl. Laser Tech. to Fluid Mech.*, Lisbon, 8-11 (2002)
- [25] Davey, A.: On the stability of flow in an elliptic pipe which is nearly circular. *J. Fluid Mech.* **87**(2), 233-241 (1978)
- [26] Prusa, V.: On the influence of boundary condition on stability of Hagen-Poiseuille flow. *Comp. Math. Appl.* **57**(5), 763-771 (2009)
- [27] Aboelkassem, Y., Staples, A.E.: Stokeslets-meshfree computations and theory for flow in a collapsible microchannel. *Theor. Comput. Fluid Dyn.* **27**(5), 681-700 (2013)
- [28] Aboelkassem, Y., Staples, A.E.: A three-dimensional model for flow pumping in a microchannel inspired by insect respiration. *Acta Mech.* **225**(2), 493-507 (2014)
- [29] Huh, D., Kim, H.J., Fraser, J.P., Shea, D.E., Khan, M., Bahinski, A., Hamilton, G.A., Ingber, D.E.: Microfabrication of human organs-on-chips. *Nature America, Inc.* **8**(11), 2135-2157 (2013)

- [30] Dittrich, P.S., Manz, A.: Lab-on-a-chip: microfluidics in drug discovery. *Nature*.**5**, 210-218 (2006)
- [31] Grinias, J.P., Kennedy, R.T.: Advances in and prospects of microchip liquid chromatography. *Trends Analyt Chem.* **81**, 110-117 (2016)
- [32] Unger, M.A., Chou, H.P., Thorsen, T., Scherer, A., Quake, S.R.: Monolithic Microfabricated Valves and Pumps by Multilayer Soft Lithography. *Science*. **288**(5463), 113-116 (2000)
- [33] Thorsen, T., Maerkl, S.J., Quake, S.R.: Microfluidic Large-Scale Integration. *Science*. **298**(5593), 580-584 (2002)
- [34] Agrawal, A., Prabhu, S.V.: Survey on measurement of tangential momentum accommodation coefficient. *J. Vac. Sci. Technol. A.* **26**(4), 634-645 (2008)
- [35] Socha, J. J., Forster, T. D., Greenlee, K. J.: Issues of convection in insect respiration: insights from synchrotron X-ray imaging and beyond. *Resp. Physiol. Neurobi.* **173**, S65-S73 (2010)
- [36] Lauga, E., Stone, H. A.: Effective slip in pressure-driven Stokes flow. *J. Fluid Mech.* **489**, 55-77 (2003)

# Chapter 3

## Slip flow in a microtube driven by rhythmic wall collapses

### Publication information

The contents of this chapter are being prepared as a manuscript to be submitted for peer review as:

Chatterjee, K., & Staples, A.. Slip flow in a microtube driven by rhythmic wall collapses.

### 3.1 Abstract

In this study we mathematically modeled the fluid flow in parts of insect tracheal tubes which are in the slip flow regime and undergo rhythmic collapse. For this, a long microtube has been considered, the flow through which is driven by two consecutive wall contractions with time lag in between them, a mechanism which has been hypothesized to drive the flow in insect respiratory systems. First order accurate slip boundary conditions have been incorporated in order to determine their effect on the unidirectional volumetric flow. Published intratracheal pressure data for a blow fly (*Calliphora vicina*) has been used to model the pressure boundary conditions. The two-dimensional Navier-Stokes equations have been solved with lubrication theory and microscale assumptions. The variations of the axial velocity, pressure gradient and static pressure along the axial direction have been plotted for different time instances

and three different Knudsen number values which span the continuum and slip flow regimes. It was observed that the resulting volumetric flow rate decreased with an increase in Knudsen number and the phase lag that produced maximum flow rate was in the range of  $60^\circ - 70^\circ$ . Additionally, flows in the negative direction were observed at approximately  $0^\circ - 20^\circ$  and  $120^\circ - 180^\circ$  phase lag values, which demonstrated that the flow direction can be controlled via the actuation phase lag parameter alone.

## 3.2 Introduction

Over the last couple of decades, microfluidics has seen immense advancements in terms of application areas, increases in efficiency, and the miniaturization and portability of devices. Though it is not entirely possible to capture the full spectrum of developments, in this section, we will try to address some of the most critical and influential advancements made in the field of microfluidics in the recent times. One of the most remarkable applications of microfluidics has been in the domain of organs-on-a-chip. Attempts are being made to create the perfect biomimetic microenvironment that captures the essential functional features of the alveolar-capillary interface of human lung and mechanical, structural and physiological properties of human intestine [1],[2]. Hu et. al. in [1], have created a microsystem that reproduced organ level responses to bacteria and cytokines. Their microdevices have the potential to act as the basis for future improvements in cell culture models and cheaper alternatives to animal and clinical studies. Kim et. al. [2] have fabricated a human lung-on-a-chip model composed of microfluidic channels with a porous membrane in between, lined by human intestinal epithelial cells. Thus they were able to recreate the human intestinal microenvironment that mimics its essential physical and functional features, suitable for studies on transport, absorption and toxicity. The field of neuroscience has also seen a

wide variety of applications of microfluidics. In this context one of the earliest and most important studies has been conducted by Taylor et. al. in 2002 [3]. The authors in their investigation, have outlined a methodology for fabricating a multicomponent microfluidic device specially targeted towards neuronal culture. They used PDMS (Polydimethylsiloxane) based soft lithography techniques for the fabrication of a double chambered device with a physical barrier with grooves, separating the two chambers. The cells placed in one of the chambers extended into the other compartment via the grooves after 3-4 days. With their devices, the authors were also able to direct and orient the sites of neuronal attachment and neurite outgrowth thus proving that their device had significant advantage over the open culture and other conventional methods. Microfluidics have often been employed for single cell analysis techniques. Wheeler et. al [4] developed a PDMS based microfluidic network equipped with valves and pumps, with the capability of passive cell separation from a bulk suspension and delivering nanoliter volume of reagents to it. The electrophoretic separation and preconcentration of double stranded DNA fragments were performed in microfluidic devices by Wainright et. al [5]. A zone electrophoretic (ZE) separation step was coupled with a preconcentration step based on isotachopheresis (ITP) in order to increase the detection concentration limit. Microfluidic technology has been extensively employed in the field of drug discovery. Dittrich et. al. in [6] have provided a detailed review of the current and future applications of microfluidic chips in drug discovery. The authors argued that in spite of the identical molecular reactions as the macroscale, surface per volume scaling laws, molecular diffusion and heat transport increases the throughput in the microfluidic devices. Other than the biological and biomedical fields, microfluidics have witnessed a plethora of applications in other areas as well. For example microscale chemical analyses using microfluidic devices, chips and cards have significant advantages over their macroscale counterparts in portability, accessibility, cost and sample requirements. For this reason, microscale chemical analyzers have been extensively in hazardous and extra-terrestrial en-

vironments [7], [8], [9], [10]. Pumping at the microscale is a critical topic that has been the subject of investigation because of its diverse applications. A lot of research has been conducted on the operational mechanisms, performances, efficiencies and flow rates of micropumps. In their article [11], Laser et. al. have reviewed the development, operational procedures and performances of different types of displacement (for example, reciprocating, rotary, and aperiodic) and dynamic (for example, centrifugal, electrohydrodynamic, electroosmotic, magnetohydrodynamic, acoustic streaming, and special effect) micropumps. In the context of micropumps the study of Unger et. al. [12] on monolithic microfabricated valves and pumps needs a special mention. The authors used multilayer soft lithography to fabricate active microfluidic systems consisting of different types of valves and pumps which were built of elastomer. Thus, in this article the authors highlighted different advantages of the soft lithography process. Lastly, one of the most complicated recent developments is the concept of microfluidic large-scale integration by Thorsen et. al. ([13]). The authors fabricated microfluidic pumping networks with multiple micromechanical valves and chambers, analogous to electronic integrated circuits. They used fluidic multiplexor which can perform complex fluidic manipulations thus exponentially increasing the processing power of the network.

Since the present study investigates rarefied flow in microtubes, it is necessary to highlight the relevant studies on this subject. In [14], Cui et. al. investigated the liquid flow characteristics in microtubes driven by high pressure of 1 MPa to 30 MPa. Apart from studying the normalized friction coefficient, the authors highlighted the role of viscosity at high pressure by analyzing liquid compressibility, tube deformation, viscous heating, and wall slip. Flow characteristics of water in microtubes were analyzed by measuring the pressure drop and flow rates in [15]. The study indicated significant departure from the predictions of conventional microtube theory. It was concluded that Poiseuille flow theory failed to pre-

dict the pressure gradient at high Reynolds number. The study also revealed a dependence of the flow behavior on the microtube material. The transition from laminar to turbulent flow of different polarity liquids in glass microtubes has been studied in [16]. From pressure drop and micro-PIV measurements, it was evident that the transition occurred at Reynolds numbers of 1,800 - 2,000. For Reynolds numbers less than 1,800, the pressure drop versus flow rate data confirmed the macroscopic results from Poiseuille flow equations for laminar flow resistance within  $\pm 2.5\%$  rms and  $-1\%$  systematic error. Numerical investigation of the effects of viscous heat dissipation and slip on the friction number of water flow in microtubes was performed in [17]. It was found that there was a decrease in friction number with a reduction in dynamic viscosity. The friction number also decreased with the wall slip with increased aspect ratio. Velocity profiles, shear stresses, friction factors, and momentum flux have been derived by the integral transform technique in [18] to analyze laminar slip flow in rectangular ducts. The authors showed that the results match perfectly with those of macroscale fluid dynamics in the limit of  $\text{Kn} \rightarrow 0$ . The steady flow of gas through rectangular microducts with second order accurate slip boundary conditions was analytically modeled by Aubert et. al. in [19]. The study reveals an underestimated mass flow rate value when second order terms are discarded, especially when the cross sectional geometry of the microduct tends to a square. Physics-based models of rarefied flow of gas in smooth surfaced pipe channels and ducts have been developed in [20]. In order to include the effects of reduced momentum and heat exchange, the authors propose a second order accurate general slip boundary condition. A unified model was developed to predict the pressure distribution and mass flow rate in entire Knudsen number regime. The accuracy of the model was tested by comparing the results with those from linearized Boltzmann solutions, experimental data, and Direct Simulation Monte Carlo (DSMC). Sparrow et. al. analytically investigated the laminar flow in tubes with slip boundary conditions, for low-density phenomenon effects on heat transfer characteristics [21]. The slip-flow Nusselt numbers were found to be lower than

those in the continuum regime and were inversely proportional to the mean free path. In [22], the authors used perturbation method analysis to investigate the low Reynolds number slip flow of gas in microtubes. They used first order accurate Maxwell boundary conditions and solve Navier-Stokes equations to obtain the results which showed good agreement with those from experimental studies.

The motivation behind the mathematical modeling in the present study are the seminal studies by Westneat et. al. [23], [25]. Earlier it was believed that the insects breathe by diffusion of respiratory gases through pores in the cuticle known as spiracles. But in [23], the authors used synchrotron X-ray imaging to view the respiration mechanism inside live insects which revealed rapid cycles of compression and expansion in the tracheal tubes of head and thorax. Similarly in [24], Socha et. al. used flow-through respirometry and synchrotron X-ray imaging to visualize the respiration process of ground beetle *Pterostichus stygicus* to find a correlation between tracheal compression and excurrent gas exchange. The study concluded that the tracheal compression, which is the driving factor behind trans-spiracular and intratracheal convection of air, plays a major role in the ventilation for many insects.

Finally, some initial studies on microscale flows inspired by insect respiration mechanisms have been carried out. Aboelkassem et. al. conducted a number of analytical and computational investigations on insect respiratory system inspired flows in 2D and 3D microchannels [28],[29], [30]. In [26] Aboelkassem and Staples put forward a bioinspired pumping model for microtube flow. The authors started with an analytical investigation of flow in a microtube driven by wall collapses with a time lag between them in order to mimic the wall contraction kinematics of insect tracheal tubes. After that they validated the analytical model by Stokeslets-meshfree computational method and concluded that this particular driving mechanism is capable of producing a unidirectional flow. Chatterjee and Staples also analytically investigated the effects of first order accurate slip boundary conditions on fluid flow in a

microchannel driven entirely by the same wall collapse mechanism as mentioned earlier [31]. The present study builds upon the mathematical model used in [31] and [26], and incorporates first order accurate slip boundary conditions following [27] and [21] to investigate the effects of rarefaction on the insect mimetic microtube flow.

### 3.3 Mathematical modeling

A mathematical model describing the flow characteristics in the simplified tracheal tube geometry driven by rhythmic, axisymmetric, and non-peristaltic wall contractions has been derived. Microscale and lubrication theory assumptions have been taken into account ([32], [33], and [34]) to derive simplified versions of Navier-Stokes equations for Newtonian, incompressible flow with constant viscosity  $\mu$ . The velocity field of the fluid flow can be described as  $\mathbf{V} = (V_r, 0, V_x)$ . The other parameters have been non-dimensionalized according to the following convention  $x = x^*/L$ ,  $r = r^*/R$ ,  $H = H^*/R$ ,  $t = t^*/(L/u_o)$ ,  $V_x = V_x^*/u_o$ ,  $V_r = V_r^*/\delta u_o$ ,  $p = p^*R^2/(\mu u_o L)$ ,  $Q = Q^*/(u_o \pi R^2)$ , and  $Re = \rho u_o R/\mu$ . In this non-dimensionalization scheme  $V_r$  and  $V_x$  are the radial (r) and the axial (x) components of the velocity,  $p$  static pressure,  $Q$  is volumetric flow rate,  $Re$  is the Reynolds number, and  $t$  is the time scale. An arbitrary reference velocity  $u_o$  has been used to non-dimensionalize the parameters.  $u_o$  can be chosen as the inlet or the outlet velocity. Now using the mentioned scheme and following [26] the Navier-Stokes equations in cylindrical coordinate system can be reduced to

$$\frac{1}{r} \frac{\partial}{\partial r} (r V_r) + \frac{\partial V_x}{\partial x} = 0 \quad (3.1)$$

$$\frac{\partial p}{\partial r} = 0 \quad (3.2)$$

$$\frac{1}{r} \frac{\partial}{\partial r} \left( r \frac{\partial V_x}{\partial r} \right) = \frac{\partial p}{\partial x}. \quad (3.3)$$

The above simplified equations can be solved using the following boundary conditions where the slip flow parameter,  $\beta = \frac{2-\sigma}{\sigma} \frac{Kn}{1-bKn}$ . Here,  $\sigma$  is the tangential momentum accommodation coefficient whose value has been assumed to be 1 following conventional practice and  $Kn$  is the Knudsen number, which is a dimensionless quantity and can be defined as  $Kn = \lambda/l$  where  $l$  is the characteristic length scale and  $\lambda$  is the mean free path of the fluid molecules. Following [20], assuming first order accurate slip boundary conditions, the value of  $b$  has been assumed to be zero. Thus for this study the slip flow parameter  $\beta$  is identically equal to the Knudsen number  $Kn$ . The slip boundary conditions have been assumed following [27] and [21].

- (i) at  $r = 0$ ,  $V_r = 0$ ,  $\frac{\partial V_x}{\partial r} = 0$
- (ii) at  $r = H(x, t)$ ,  $V_r = \frac{\partial H}{\partial t}$ ,  $V_x = -\beta \frac{\partial V_x}{\partial r}$
- (iii) at  $x = 0$ ,  $p = p_o(t)$
- (iv) at  $x = L$ ,  $p_L = F(t)$ .

Integrating Eq. 3.3 twice with respect to  $r$  and using boundary conditions (i) and (ii) the following expression for the axial velocity,  $V_x$  can be derived.

$$V_x = \frac{1}{4} \frac{\partial p}{\partial x} (r^2 - 2\beta H - H^2) \quad (3.4)$$

Using equations 3.1 and 3.4 along with the boundary condition (i) we derive an expression for the radial velocity,  $V_r$ , which is as follows.

$$V_r = \frac{r}{4} \frac{\partial^2 p}{\partial x^2} \left( \frac{H^2}{2} - \frac{r^2}{4} + \beta H \right) + \frac{r}{4} \frac{\partial H}{\partial x} \frac{\partial p}{\partial x} (H + \beta) \quad (3.5)$$

Applying boundary condition (ii) to Eq. 3.5 and rearranging we derive the following partial differential equation.

$$\frac{\partial^2 p}{\partial x^2} = \frac{16}{(H^3 + 4\beta H^2)} \frac{\partial H}{\partial t} - \frac{4H(\beta \frac{\partial H}{\partial x} + H \frac{\partial H}{\partial x})}{(H^3 + 4\beta H^2)} \frac{\partial p}{\partial x} \quad (3.6)$$

Equation 3.6 has been solved numerically along with a simplified version of the intratracheal pressure boundary condition information obtained from Wasserthal et. al in figure 11(A) [35]. The entire breathing cycle of the insect consists of different types of intratracheal pressure signals as depicted in figure 11(A). Only a small portion of this breathing cycle, which lasts for 1 second, has an abdominal contraction. It is unknown whether tracheal collapse happens in this insect. But in order to create an improved model of the tracheal pathway (compared to the model in previous chapter), it has been assumed in the present study that the intratracheal pressures measured in [35] are in a physiologically relevant range for insects in which tracheal collapse does occur. Thus, all the results for the current study have been generated for this particular 1 second where it has been assumed that there is wall collapse as well as a pressure difference across the ends of the tracheal tube.

$$Q = \int_0^H V_x r dr \quad (3.7)$$

Integrating the Eq. 3.7 we get the final expression for instantaneous volumetric flow rate  $Q$ , which is as follows.

$$Q = -\frac{H^3}{16} \frac{\partial p}{\partial x} (H + 4\beta) \quad (3.8)$$

The time-averaged volumetric flow rate,  $Q_T(x)$  can be calculated by integrating Eq. 3.8 at any location along the axis.

## 3.4 Results

### 3.4.1 Wall contraction profiles

The axisymmetric collapse of the microtube wall is governed by the following function

$$H(x, t) = 1 + \sum_{i=1}^{N_c} A_i f_i(x) g_i(t) \quad (3.9)$$

where  $f_i(x)$  and  $g_i(t)$  are the spatial and the temporal wall collapse functions, and  $A_i$  is the amplitude of the wall collapse. The mathematical forms of the spatial and temporal parts of the wall collapse function in the present study have been chosen in such a way that they closely resemble the discrete wall collapses which have been hypothesized to be the driving factor of respiratory gases in the insect tracheal tubes. The function  $f_i(x)$  has been defined as

$$f_i(x) = \tanh(\alpha(x - x_i)) - \tanh(\alpha(x - (x_i + d_i))) \quad (3.10)$$

where  $\alpha = 2\pi/\delta$ . The beginning and end of each wall collapse is defined by  $x_i$  and  $(x_i + d_i)$ , respectively. In the present study two consecutive wall contractions have been chosen, where the first wall collapse is located at  $x_1 = 0.25$  and  $x_1 + d_1 = 0.35$  and the second wall collapse

is located at  $x_2 = 0.65$  and  $x_2 + d_2 = 0.75$ . The temporal variations of the first and second contraction sites are given by

$$g_1(t) = \begin{cases} \frac{1}{2} (1 - \cos(2\pi t \beta_p St)), & 0 \leq t \leq 1/\beta_p St \\ 0 & 1/\beta_p St < t \leq 1/St \end{cases} \quad (3.11)$$

and

$$g_2(t) = \frac{1}{2} (1 - \cos(2\pi t St)), \quad 0 \leq t \leq 1/St. \quad (3.12)$$

In the above equations  $\beta_p$  is the non-dimensional phase lag parameter and is related to the phase lag  $\theta_{12}$  by the relation,  $\theta_{12} = \pi(1 - 1/\beta_p)$ , where  $\theta_{12}$  is the phase lag between the first and second contractions. Both the contractions have time period  $T = 1/St = 1$ . Thus, for  $\beta_p = 1$  there is  $0^\circ$  phase lag between the two contractions. Each of the wall collapses has been chosen in such a way that it starts at  $t = 0$ , reaches its maximum amplitude at  $t = T/2$  and then comes back to its original position at  $t = T$ . In the current study, results are presented for two instances of time during the complete collapse and re-expansion cycle: at  $t = T/4$ , when the contraction is midway through the collapse half of the cycle, and then at  $t = 3T/4$  when the contraction is midway through the re-expansion part of the cycle. We have used three different values of the slip flow parameter  $\beta$ , which is identically equal to the Knudsen number  $Kn$  in the present study. These three values are  $\beta = 0$  (no slip),  $\beta = 0.01$  (intermediate slip), and  $\beta = 0.1$  (high slip). The values of  $\beta$  or  $Kn$  have been chosen in such a way that the results span from the no slip ( $\beta = 0$ ) to the highest value of slip in the slip flow regime ( $\beta = 0.1$ ). One nonzero value of the phase lag  $\beta_p$ , of  $30^\circ$ , has been chosen to generate results in the present study. The  $0^\circ$  phase lag case has been left out as it has been seen earlier from Figures 4 (a), (b), and (c) in [31] that there is no unidirectional

flow due to the formation of a stagnation region in between the two wall collapses, where the symmetric flows from both the directions cancel each other. Those results hold for this study as well. In contrast to the previous study, here we have modeled a part of insect tracheal tubes where there is wall collapse as well as a pressure gradient along the length. Though, from the intratracheal pressure versus time plot in Figure 11(a) in [35], it can be seen that different types of pressure drops exist across the tracheal tubes at different times of the same breathing cycle, but we have modeled only that part of the cycle where there is a co-existence of both the wall contractions as well as a constant pressure difference across the ends. All the plots in this study have been generated at a radial position of  $r = 0$  which is the axis of the tube.

### 3.4.2 Velocity and pressure

Figures 3.1(a) and 3.1(b) show the  $V_x$  velocity profiles at the axis of the tube for a phase lag of  $\theta_{12} = 30^\circ$  at  $t = T/4$  and  $t = 3T/4$ , respectively. Three different values of the slip flow parameter  $\beta = 0, 0.01, \text{ and } 0.1$ , have been used to generate these plots. It can be seen that the two  $V_x$  velocity plots at  $t = T/4$  and  $T = 3T/4$  are not symmetric. It is this temporal asymmetry that causes a net unidirectional flow towards the right (the positive direction) in the  $30^\circ$  phase lag case. Unlike the  $0^\circ$  phase lag case, where there is a stagnation region at the center between the two contractions, in the  $30^\circ$  phase lag case a positive, non-zero velocity exists at the center. This is evident from Figures 3.1(a) and 3.1(b) where we see an non-zero value of  $V_x$  in the middle of the tube between the two contractions. One of the most remarkable features of these plots is that in the wall contraction dominated regions, i.e.,  $x = 0.2$  to  $x = 0.4$  and  $x = 0.6$  to  $x = 0.8$  in Fig. 3.1(a) and  $x = 0.6$  to  $x = 0.8$  in Fig. 3.1(b), we see that the magnitude of the axial velocity increases with a decrease of the value of the slip flow parameter. Whereas, in the pressure gradient dominated regions, i.e.,

$x = 0$  to  $x = 0.2$  and  $x = 0.8$  to  $x = 1$  in Fig. 3.1(a) and  $x = 0.8$  to  $x = 1$  in Fig. 3.1(b), the magnitude of the axial velocity decreases with decrease of slip. Thus, the relationship between the value of the slip flow parameter and the axial velocity depends on the dominant factor driving the flow in that particular region of the tube.

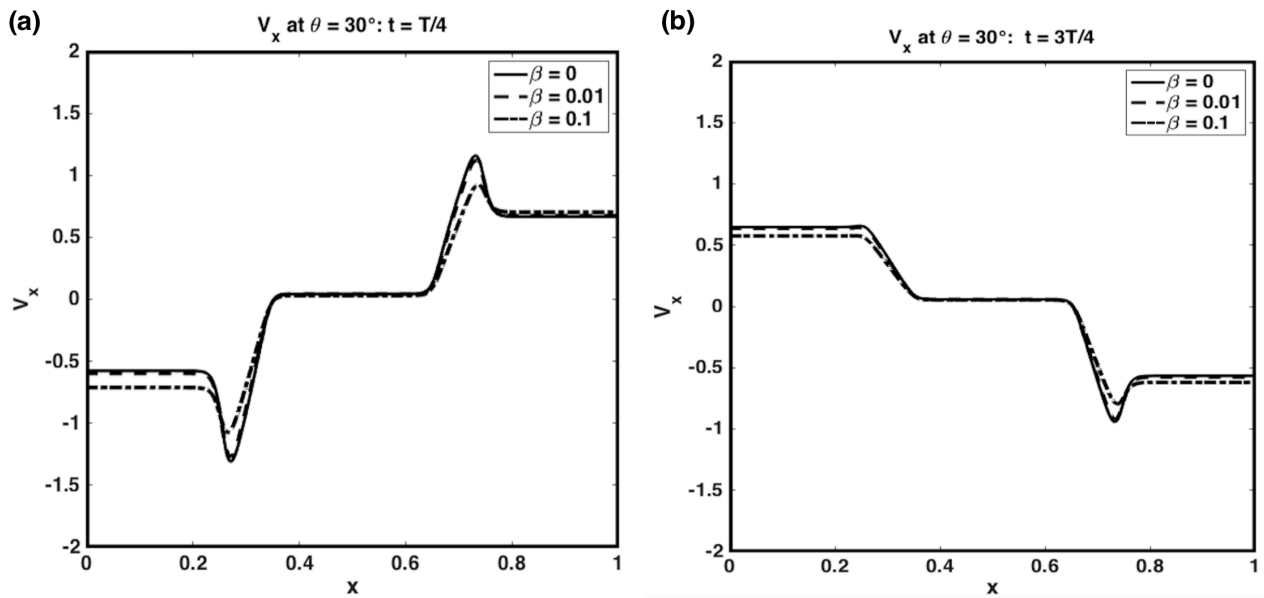


Figure 3.1: Comparison of  $V_x$  for  $\theta_{12} = 30^\circ$  at  $t = T/4$  and  $t = 3T/4$ . Three representative cases are shown: high slip ( $\beta = 0.1$ ), low or intermediate slip ( $\beta = 0.01$ ), and no slip ( $\beta = 0$ ).

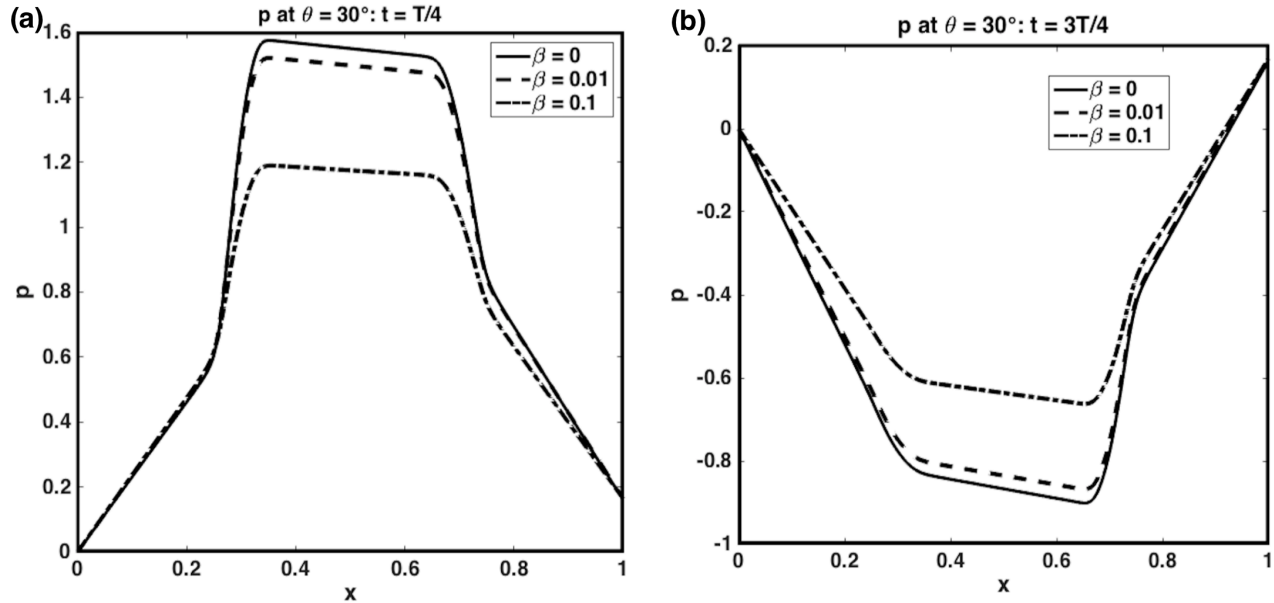


Figure 3.2: Comparison of  $p$  for  $\theta_{12} = 30^\circ$  at  $t = T/4$  and  $t = 3T/4$ . Three representative cases are shown: high slip ( $\beta = 0.1$ ), low or intermediate slip ( $\beta = 0.01$ ), and no slip ( $\beta = 0$ ).

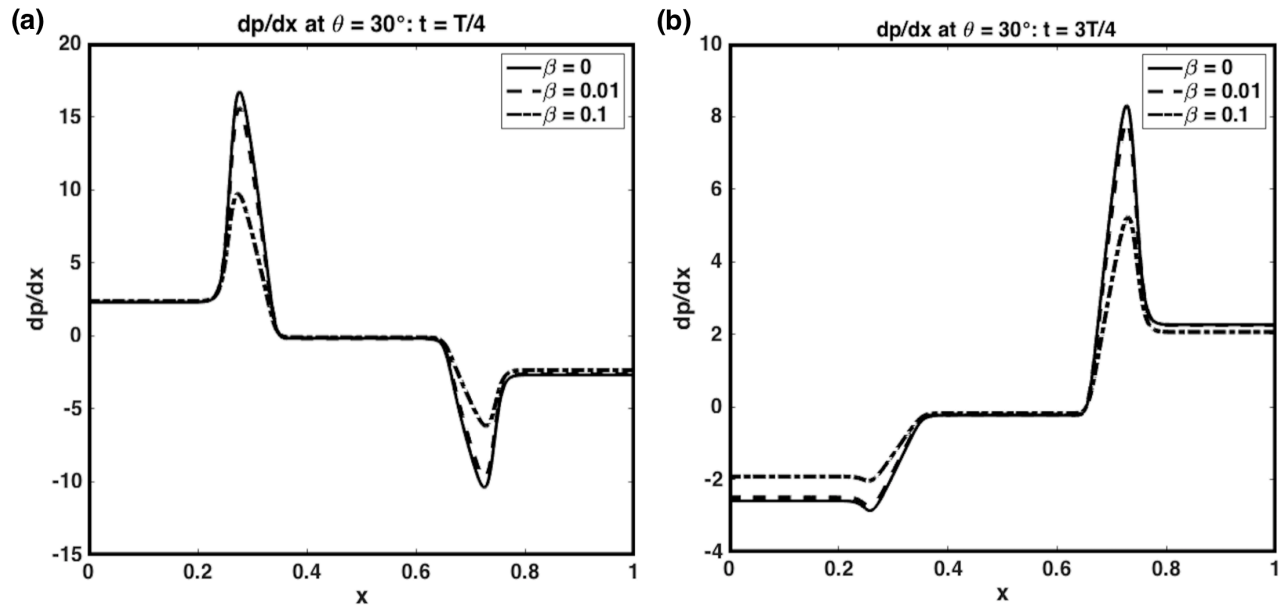


Figure 3.3: Comparison of  $dp/dx$  for  $\theta_{12} = 30^\circ$  at  $t = T/4$  and  $t = 3T/4$ . Three representative cases are shown: high slip ( $\beta = 0.1$ ), low or intermediate slip ( $\beta = 0.01$ ), and no slip ( $\beta = 0$ ).

When the magnitude of the wall contraction is high enough, the resulting pressure gradient

generated by it is also high. So, it can act as the main driving factor in certain regions of the flow domain. This explains the behavior that can be seen from  $x = 0$  to  $x = 0.2$  in Fig. 3.1(b), where the effect of the extremely large wall collapse and resulting pressure gradient, as evident from the pressure gradient plot in 3.3(a), takes over as the main driving mechanism of the flow.

Figures 3.2 (a) and (b) show the variations of the static pressure  $p$  along the axis of the tube at  $t = T/4$  and  $t = 3T/4$ , respectively. One interesting feature of this plot is the non-zero value of the static pressure at  $x = 1$ , which has been externally imposed as the pressure boundary conditions as discussed earlier. Thus, in this study, the fluid flow is driven by a combination of wall contractions and pressure drop across the ends. Also, the magnitudes of the static pressure at both  $t = T/4$  and  $t = 3T/4$  increase with decreasing slip. The axial pressure gradient  $dp/dx$  has been plotted along the  $x$  direction in Figs. 3.3(a) and 3.3(b). The magnitude of the pressure gradient mostly increases with a decrease in the value of the slip flow parameter  $\beta$ .

### 3.4.3 Net flow produced

The instantaneous volumetric flow rate  $Q(x, t)$  has been integrated over an entire contraction-re-expansion cycle in order to obtain the net flow produced, using the following equation

$$Q_T(x) = \frac{1}{T} \int_0^T Q(x, t) dt. \quad (3.13)$$

The time-averaged volumetric flow rate has been plotted for different phase lag values in Fig. 3.4. The results for two different values of  $\beta$  are compared. It can be seen from Fig. 3.4 that the volumetric flow rate over an entire cycle increases with decreasing slip, a trend which has

already been observed in [31]. The results are in agreement with those obtained from [36] where the authors analyzed the variation of the volumetric flow rate for a pressure driven flow with slip boundary conditions. It can be seen from Fig. 3.4 that the maximum flow occurs for a phase lag of 70-75°. Another interesting feature as is evident from Fig. 3.4 is the existence of negative flow rates for very low ( $0^\circ$  to  $20\text{-}30^\circ$  and very high ( $110\text{-}130^\circ$  to  $180^\circ$ ) phase lag values, which demonstrates phase lag-based flow reversal in an insect respiratory tract-inspired microtube model.

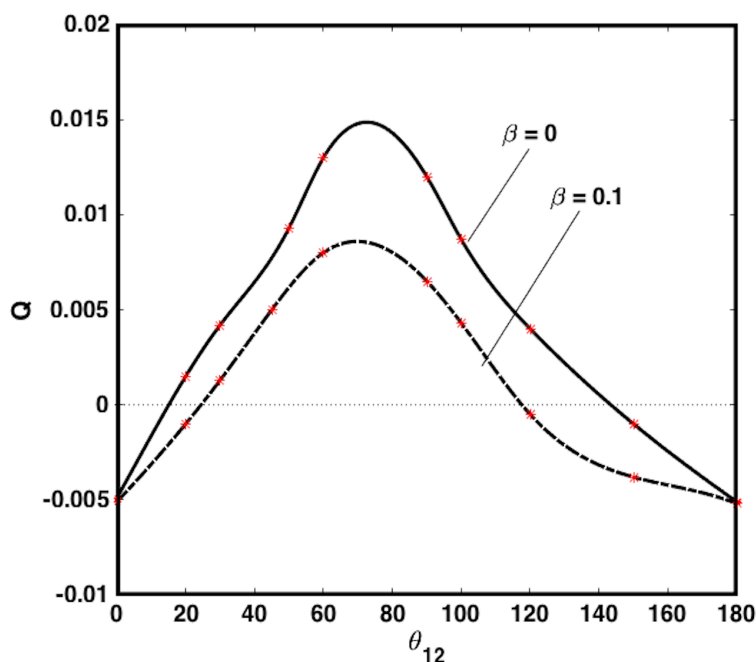


Figure 3.4: Time-averaged net flow rate plotted against phase lag values over an entire contraction-relaxation cycle at  $x = 0.5$ . Three representative cases are shown: high slip ( $\beta = 0.1$ ), low or intermediate slip ( $\beta = 0.01$ ), and no slip ( $\beta = 0$ ). The asterisk marks on the plots represent the data points. The solid solid and the dashed lines are cubic splines fit to the data points showing the trend of calculations.

## 3.5 Conclusions

In the present study, the fluid flow through a portion of a simplified insect tracheal tube in which the flow is driven by a pressure difference across the ends of the tube as well as cyclical wall collapse has been mathematically modeled. The Navier-Stokes equations in cylindrical coordinates have been solved with microscale and lubrication theory assumptions along with first order accurate wall slip boundary conditions to derive the expressions for axial velocity, pressure gradient and static pressure. Three different values of the slip flow parameter  $\beta$  (identically equal to the Knudsen number,  $Kn$ ) have been used in order to span the continuum and slip flow regimes. The axial velocity, pressure gradient, and static pressure have been plotted along the axis of the tube at two different instances of time,  $t = T/4$  (halfway collapsed) and  $t = 3T/4$  (halfway re-expanded), during the contraction-relaxation cycle. In order to present a more physiologically relevant model compared to that in the previous chapter, published intratracheal pressure values in the blow fly were used as the distal pressure boundary condition. It was seen that, following the trends of the study in the previous chapter, here also, an increase in slip decreases the axial velocity in wall contraction (shear) dominated regions, whereas the reverse happens in pressure gradient dominated regions. Other than that it was observed that increasing slip decreases the volumetric flow rate over an entire cycle and that the maximum flow occurs for a phase lag of 70-75°. Lastly, the existence of negative flow was observed for very low and very high values of the phase lag parameter. Thus, it was demonstrated that using suitable combinations of the phase lag parameter and the pressure difference across the ends of a model tracheal tube, both the direction and the magnitude of the flow rate can be varied via the phase lag parameter alone. The knowledge gained from this study can potentially be used to fabricate insect-mimetic microfluidic devices with geometric features that produce built-in phase lags between the adjacent collapse sites that drive the flow. In such devices the magnitude and direction of

flow could be controlled by varying the actuation frequency alone, instead of by using a complicated system of valves and pumps. Such devices are the subject of the next chapter.

# References

- [1] Huh, D., Matthews, B. D., Mammoto, A., Montoya-Zavala, M., Hsin, H. Y., & Ingber, D. E. (2010). Reconstituting organ-level lung functions on a chip. *Science*, 328(5986), 1662-1668.
- [2] Kim, H. J., Huh, D., Hamilton, G., & Ingber, D. E. (2012). Human gut-on-a-chip inhabited by microbial flora that experiences intestinal peristalsis-like motions and flow. *Lab on a Chip*, 12(12), 2165-2174.
- [3] Taylor, A. M., Rhee, S. W., Tu, C. H., Cribbs, D. H., Cotman, C. W., & Jeon, N. L. (2003). Microfluidic multicompartiment device for neuroscience research. *Langmuir*, 19(5), 1551-1556.
- [4] Wheeler, A. R., Thronset, W. R., Whelan, R. J., Leach, A. M., Zare, R. N., Liao, Y. H., ... & Daridon, A. (2003). Microfluidic device for single-cell analysis. *Analytical chemistry*, 75(14), 3581-3586.
- [5] Wainright, A., Nguyen, U. T., Bjornson, T., & Boone, T. D. (2003). Preconcentration and separation of double-stranded DNA fragments by electrophoresis in plastic microfluidic devices. *Electrophoresis*, 24(21), 3784-3792.
- [6] Dittrich, P. S., & Manz, A. (2006). Lab-on-a-chip: microfluidics in drug discovery. *Nature Reviews Drug Discovery*, 5(3), 210.
- [7] Mora, M. F., Greer, F., Stockton, A. M., Bryant, S., & Willis, P. A. (2011). Toward total automation of microfluidics for extraterrestrial in situ analysis. *Analytical chemistry*, 83(22), 8636-8641.

- [8] Ueland, M., Blanes, L., Taudte, R. V., Stuart, B. H., Cole, N., Willis, P., ... & Doble, P. (2016). Capillary-driven microfluidic paper-based analytical devices for lab on a chip screening of explosive residues in soil. *Journal of Chromatography A*, 1436, 28-33.
- [9] Henares, T. G., Yamada, K., Takaki, S., Suzuki, K., & Citterio, D. (2017). “Drop-slip” bulk sample flow on fully inkjet-printed microfluidic paper-based analytical device. *Sensors and Actuators B: Chemical*, 244, 1129-1137.
- [10] Butterworth, A. L., Stockton, A. M., Turin, P., Ludlam, M., Diaz-Aguado, M., Kim, J., ... & Mathies, R. A. (2015, March). Lab-on-a-chip organic analyzer: instrumentation and methods for detecting trace organic molecules and amino acid chirality in planetary science. In *Lunar and Planetary Science Conference* (Vol. 46, p. 2813).
- [11] Laser, D. J., & Santiago, J. G. (2004). A review of micropumps. *Journal of micromechanics and microengineering*, 14(6), R35.
- [12] Unger, M. A., Chou, H. P., Thorsen, T., Scherer, A., & Quake, S. R. (2000). Monolithic microfabricated valves and pumps by multilayer soft lithography. *Science*, 288(5463), 113-116.
- [13] Thorsen, T., Maerkl, S. J., & Quake, S. R. (2002). Microfluidic large-scale integration. *Science*, 298(5593), 580-584.
- [14] Cui, H. H., Silber-Li, Z. H., & Zhu, S. N. (2004). Flow characteristics of liquids in microtubes driven by a high pressure. *Physics of fluids*, 16(5), 1803-1810.
- [15] Mala, G. M., & Li, D. (1999). Flow characteristics of water in microtubes. *International journal of heat and fluid flow*, 20(2), 142-148.
- [16] Sharp, K. V., & Adrian, R. J. (2004). Transition from laminar to turbulent flow in liquid filled microtubes. *Experiments in fluids*, 36(5), 741-747.

- [17] El-Genk, M. S., & Yang, I. H. (2009). Numerical analysis of laminar flow in micro-tubes with a slip boundary. *Energy Conversion and Management*, 50(6), 1481-1490.
- [18] Spiga, G. M. M. (1998). Slip flow in rectangular microtubes. *Microscale Thermophysical Engineering*, 2(4), 273-282.
- [19] Colin, C. A. S. (2001). High-order boundary conditions for gaseous flows in rectangular microducts. *Microscale Thermophysical Engineering*, 5(1), 41-54.
- [20] Beskok, A., & Karniadakis, G. E. (1999). Report: a model for flows in channels, pipes, and ducts at micro and nano scales. *Microscale Thermophysical Engineering*, 3(1), 43-77.
- [21] Sparrow, E. M., & Lin, S. H. (1962). Laminar heat transfer in tubes under slip-flow conditions. *Journal of Heat Transfer*, 84(4), 363-369.
- [22] Radenković, D. R., Milićev, S. S., & Stevanović, N. D. (2016). Rarefied gas flow in microtubes at low Reynolds numbers. *FME Transactions*, 44(1), 10-15.
- [23] Westneat, M. W., Betz, O., Blob, R. W., Fezzaa, K., Cooper, W. J., & Lee, W. K. (2003). Tracheal respiration in insects visualized with synchrotron X-ray imaging. *science*, 299(5606), 558-560.
- [24] Socha, J. J., Lee, W. K., Harrison, J. F., Waters, J. S., Fezzaa, K., & Westneat, M. W. (2008). Correlated patterns of tracheal compression and convective gas exchange in a carabid beetle. *Journal of Experimental Biology*, 211(21), 3409-3420.
- [25] Westneat, M. W., Socha, J. J., & Lee, W. K. (2008). Advances in biological structure, function, and physiology using synchrotron X-ray imaging. *Annu. Rev. Physiol.*, 70, 119-142.
- [26] Aboelkassem, Y., & Staples, A. E. (2013). A bioinspired pumping model for flow in a microtube with rhythmic wall contractions. *Journal of Fluids and Structures*, 42, 187-204.

- [27] Yang, Z., & Garimella, S. V. (2009). Rarefied gas flow in microtubes at different inlet-outlet pressure ratios. *Physics of Fluids*, 21(5), 052005.
- [28] Aboelkassem, Y., & Staples, A. E. (2012). Flow transport in a microchannel induced by moving wall contractions: a novel micropumping mechanism. *Acta Mechanica*, 223(3), 463-480.
- [29] Aboelkassem, Y., & Staples, A. E. (2013). Stokeslets-meshfree computations and theory for flow in a collapsible microchannel. *Theoretical and Computational Fluid Dynamics*, 27(5), 681-700.
- [30] Aboelkassem, Y., & Staples, A. E. (2014). A three-dimensional model for flow pumping in a microchannel inspired by insect respiration. *Acta Mechanica*, 225(2), 493-507.
- [31] Chatterjee, K., & Staples, A. (2018). Slip flow in a microchannel driven by rhythmic wall contractions. *Acta Mechanica*, 1-17.
- [32] Batchelor, G. K. (2000). *An introduction to fluid dynamics*. Cambridge university press.
- [33] Jaffrin, M. Y., & Shapiro, A. H. (1971). Peristaltic pumping. *Annual Review of Fluid Mechanics*, 3(1), 13-37.
- [34] Li, M., & Brasseur, J. G. (1993). Non-steady peristaltic transport in finite-length tubes. *Journal of Fluid Mechanics*, 248, 129-151.
- [35] Wasserthal, L. T. (2012). Influence of periodic heartbeat reversal and abdominal movements on hemocoelic and tracheal pressure in resting blowflies *Calliphora vicina*. *Journal of Experimental Biology*, 215(2), 362-373.
- [36] Lauga, E., & Stone, H. A. (2003). Effective slip in pressure-driven Stokes flow. *Journal of Fluid Mechanics*, 489, 55-77.

# Chapter 4

## Frequency-specific, single-actuation flow control in insect-mimetic valveless microfluidic devices

### Publication information

The contents of this chapter are ready to be submitted for peer review as:

Chatterjee, K., Graybill, P., Davalos, R., Socha, J., & Staples, A.: Frequency-specific, single-actuation flow control in insect-mimetic valveless microfluidic devices.

### 4.1 Abstract

Microfluidic technology is expected to play a critical role in the cooling of integrated circuits, allowing Moore's law to persist past 2021 [1, 2], and in other vitally important applications like lab-on-a-chip interventions in global health [3]. But fundamental topics like efficient strategies for mixing and flow control at the microscale are still poorly understood. As a result, microfluidic technology suffers from an actuation overhead problem in which microfluidic chips are tethered to extensive off-chip actuation hardware. State-of-the-art microfluidic large-scale integration (mLSI) and microfluidic very-large-scale integration (mVLSI) devices

contain thousands of flow channels that each require three separate actuations [4, 5]. However, insects and other terrestrial arthropods have been actively and efficiently handling air in complex networks of thousands of microscale tracheal pathways for millennia with the benefit of evolutionary refinements. Here we demonstrate that by using some basic entomological respiratory kinematic strategies for handling fluids at the microscale the actuation overhead for microfluidic devices can be drastically reduced. We performed a series of tests using insect-mimetic microfluidic devices fabricated using standard soft lithography techniques and found that the actuation overhead for device operation could be reduced from three actuators per flow channel to one single actuator per device. Furthermore, the flow rate and direction through individual channels could be precisely controlled by actuation frequency alone, a feature never before realized in a valveless microfluidic device. Our results demonstrate that entomological and entomomimetic microfluidics may provide an important testbed for understanding efficient strategies for handling fluids at the microscale. We anticipate our devices to be a starting point for more complex microfluidic devices that can scale these results up to full mLSI and vLSI dimensions.

## 4.2 Introduction

Great progress has been made both in scaling up microfluidic chips to the vLSI scale and in reducing the amount of peripheral actuation machinery associated with microfluidic devices. The largest microfluidic chips are now millions of valves per square centimeter [4, 5, 6, 7] and actuation strategies have been designed that reduce the required actuation load for the types of pneumatically actuated passive elastomeric microfluidic devices that mLSI and vLSI chips are based on from three actuations per flow channel to one actuation per chip, when combined with check valves [8, 9]. In contrast to these engineering efforts, insects are nature's

testbed for the active handling of fluids at the microscale. The honeybee, as an example, expertly manipulates air, water, nectar, honey, wax, and hemolymph at the microscale. Insect flight is the most demanding exercise known, and the aerobic scope of insects is unrivaled in the animal kingdom [10]. The ratio of maximum to basal rate of respiration in many species of locusts, bees, and flies is in the range 70-100 [10, 11] while in humans this ratio approaches 20 maximally and other small mammals and birds attain only about a 7- to 14-fold increase in metabolic rate during maximum exertion [10, 12]. Among many reasons for their superior performance, such as very effective coupling of adenosine triphosphate (ATP) hydrolysis and regeneration in the working flight muscles [10], the insects, unlike all other higher multicellular organisms, do not use blood as an intermediate oxygen carrier, but instead transport freshly oxygenated air from a series of spiracular openings around the body, directly to the tissues through a complex network of thousands of respiratory tracts called tracheae which ramify and decrease in size as they approach the tissue. While engineered microfluidic device flow channel densities have approached entomological levels, actuation efficiency and device performance lag far behind.

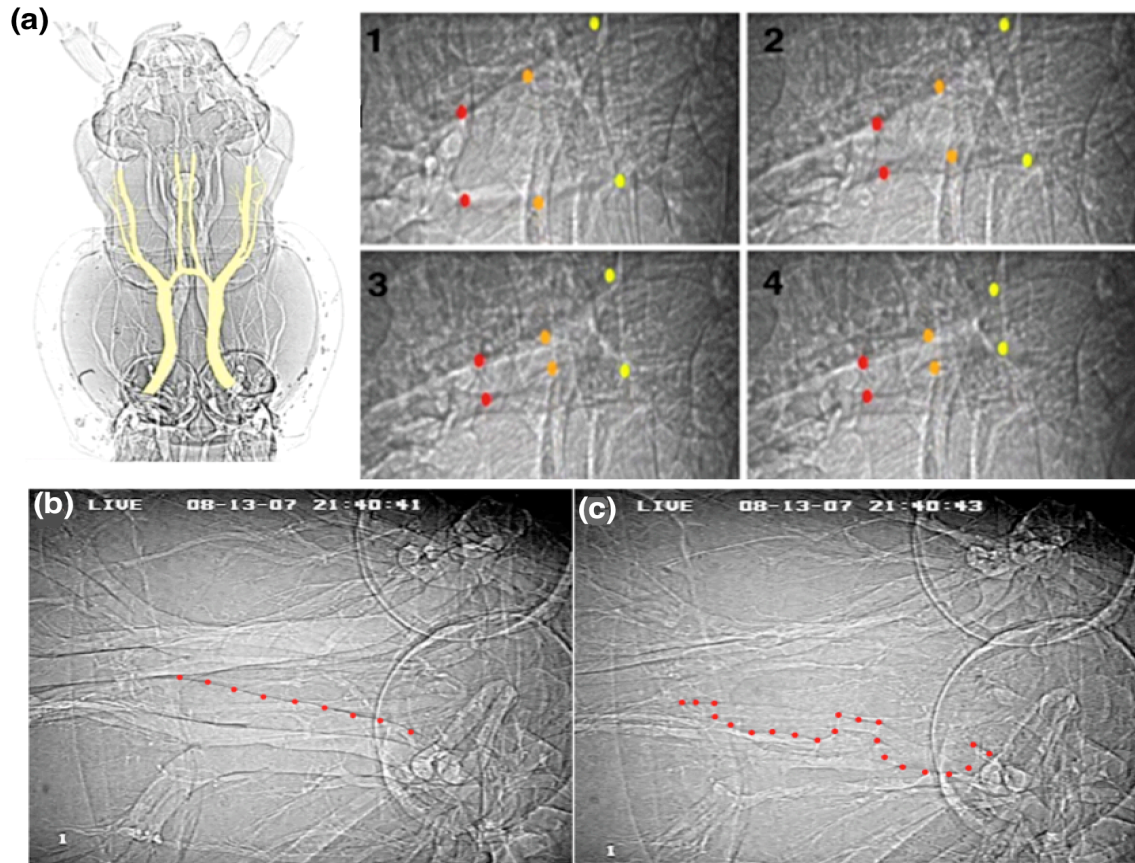


Figure 4.1: **a**, Synchrotron X-ray image of *Platynus decentis* (top view) head and thorax with largest thoracic respiratory tracts highlighted (modified by J.J. Socha with permission from [26]). *Inset 1 – 4*: Time series images of directional tracheal collapse in the bess beetle, *Odontotaenius disjunctus*. Collapse propagates from lower left of image (red point pair) to upper right (yellow point pair).([18]). **b**, Synchrotron X-ray image of the largest thoracic tracheae, fully inflated, in *Pterostichus stygicus*. **c**, Synchrotron X-ray image of the largest thoracic tracheae, fully collapsed with discrete collapse location indicated ([14]).

Here, we sought to benefit from evolutionary advances made by insects in handling fluids at the microscale by incorporating some of the fundamental features of their unique respiratory systems into the design of a series of biomimetic microfluidic devices using the current state-of-the-art multilayer soft lithography techniques. We designed, fabricated, and tested a total of eleven single-channel devices (Fig. 4.2).

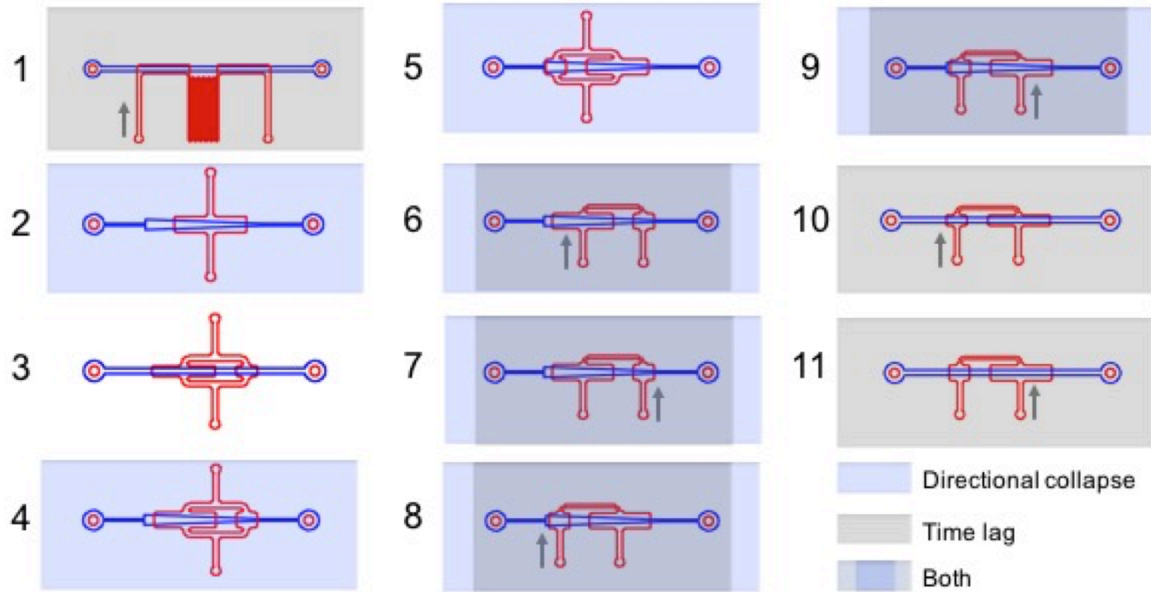


Figure 4.2: Schematics of the eleven single-channel devices fabricated and tested. Positive flow is in the direction of the ‘+’ symbol. The grey channels are the actuating channels, and the colored ones are fluid channels. The grey arrows show the direction of the pressurized gas inflow into the actuating channel. Devices S2 and S4-9 produce the directional collapse phenomenon observed in insects by incorporating a tapered flow channel. Devices S1 and S3-11 produce the discrete collapse phenomenon observed in insects by incorporating two discrete collapse locations. Devices S6-11 produce a time lag between discrete collapses by incorporating a u-shaped actuation channel.

These single-channel devices were meant to capture the fundamental kinematic and actuation strategies occurring in a single, proximal (to the spiracles) insect tracheal pathway. Tracheal pathway collapse, while pathological in other higher organisms, occurs during active respiration in insects [13]. The collapse is hypothesized to occur in response to the rhythmic abdominal contractions that pressurize the hemolymph in the animal’s body cavity, which surrounds the tracheae and causes them to buckle in localized regions [14, 15, 16, 17] (see Figs. 4.1(a)-(c)). The hemolymph pressure is a single scalar actuation input that appears to largely control the complex, passive dynamics of the entire respiratory network.

To mimic this feature, we extended current mLSI and VLSI three-layer PDMS technology

by connecting the overlying actuation channels in the top layer so that they are all actuated simultaneously by the same source. In addition to the using a single pressurized actuation chamber we incorporated both the directional and discrete collapse phenomenon that have been observed [14, 15, 16, 18] and modeled [19, 20, 21, 22, 23, 24] in insects.

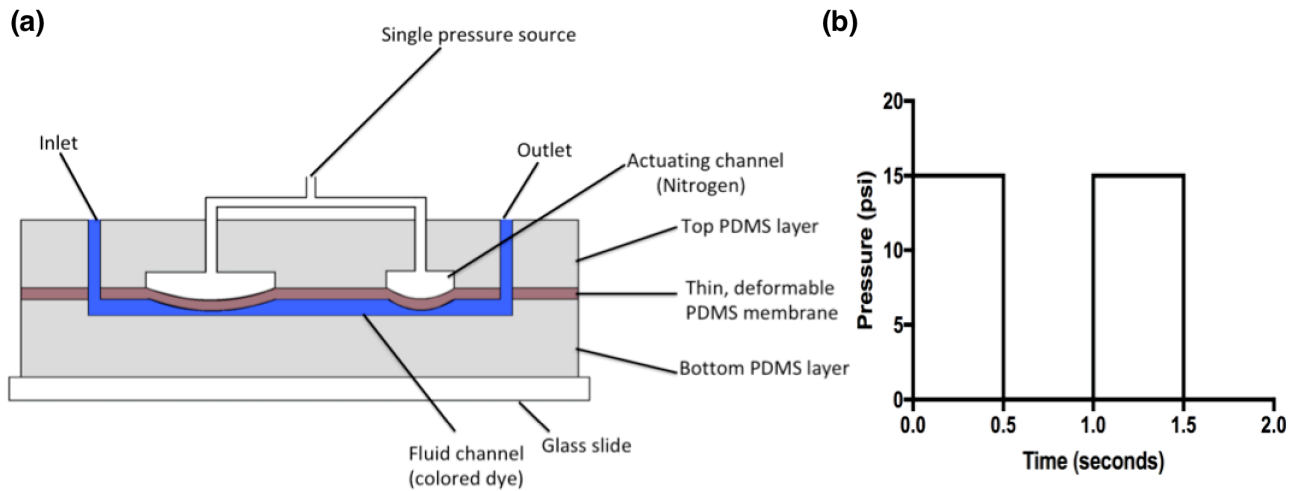


Figure 4.3: **a**, Schematic (side view) of three layer PDMS device. Bottom (clear) layer is a foundational layer consisting of a glass slide. Grey layers are cured PDMS. Blue layer is the flow channel (depth is  $80\ \mu\text{m}$  for all devices, width varies from  $100\text{-}1000\ \mu\text{m}$ ). Dark grey layer is the elastomeric membrane that serves as the flow channel ceiling (thickness  $14\text{-}20\ \mu\text{m}$ ). Clear top channels are the actuation channels into which pressurized gas is released and subsequently evacuated in order to collapse the flow channel ceiling. **b**, A representative pressure signal in the actuation channel.

Directional collapse (Fig 4.1(a)) is hypothesized to occur because of either a gradation in material strength along the axis of the respiratory tract, or because of pressure waves propagating through the hemolymph, or a combination of both features. Here, we added directionality to the channel ceiling collapse in some of the devices by fabricating tapered flow channels (devices S2 and S4-9). To produce discrete collapses (Fig. 4.1b-c), we fabricated devices with two discrete sections of elastomeric membrane (devices S1 and S3-11). Some of the discrete collapse devices (S6-11) exhibited a time lag between the occurrence of the first and second collapses in a contraction cycle. This was accomplished by incorporating

u-shaped actuation channels in these devices so that the pressurized gas (air or nitrogen) in the actuation channel would reach one collapse site slightly before the other due to the finite time required for the pressure wave to propagate through the gas.

### 4.3 Results and discussion

All eleven single-channel devices acted as hydrodynamic ratchets, rectifying the symmetric actuation input (Fig. 4.3) into a unidirectional flow. In all the devices, for a given actuation pressure, magnitude, and duty cycle (held constant at 0.50 for all experiments), the flow rate depended continuously on actuation frequency alone (see Fig. 4.4c). In one device (S4) we were also able to control the flow direction solely by actuation frequency. At an actuation pressure magnitude of 13 psi, device S4 produced a forward flow for actuation frequencies below a critical actuation frequency of about 4 Hz, and produced flow in the reverse direction for actuation frequencies above that critical frequency.

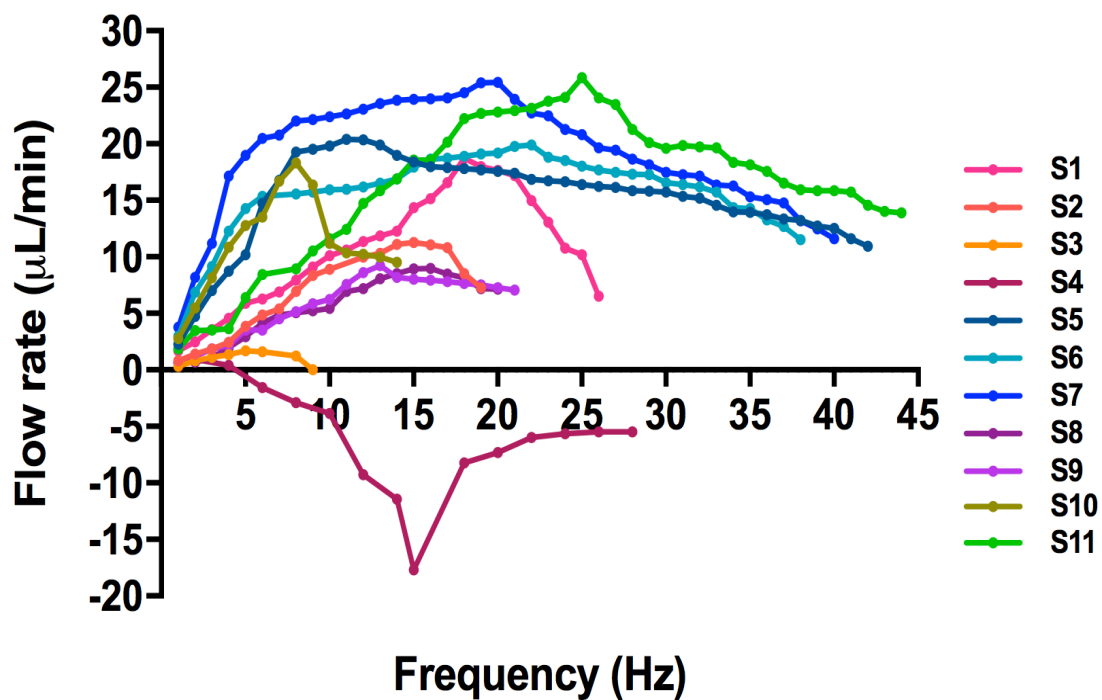


Figure 4.4: Volumetric flow rate versus actuation frequency for all eleven single-channel devices. All devices produce unidirectional flow in response to a single, symmetric actuation signal. Device S4 reverses the flow direction above a critical actuation frequency threshold of approximately 4 Hz.

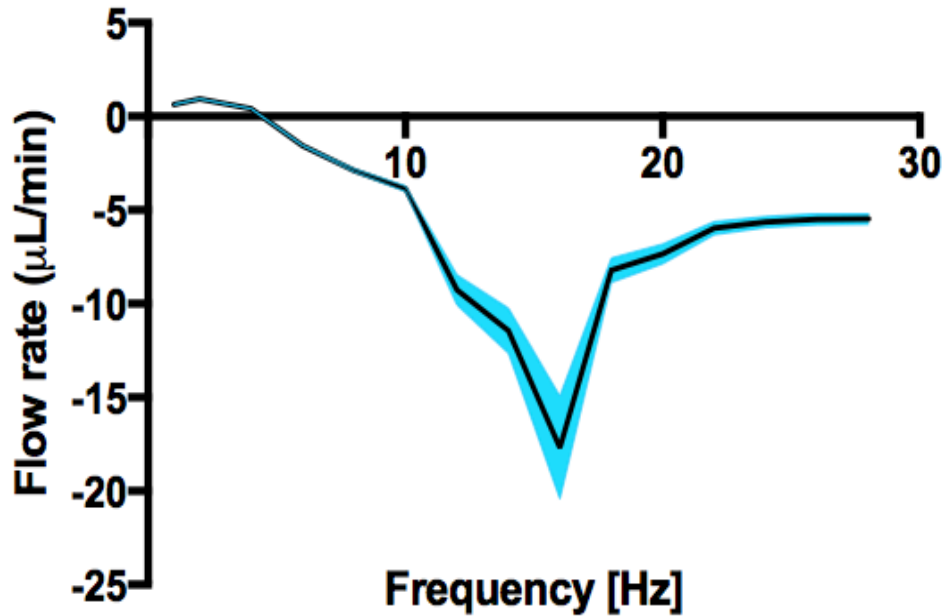


Figure 4.5: Volumetric flow rate versus actuation frequency for Device S4 with error envelope. The shading represents the uncertainty in the data due to measurement error and is calculated as the maximum possible error in the volumetric flow rate due to the resolution of the measurement of the time taken by the fluid front to travel a certain distance in the outlet tube.

We also held the actuation frequency and duty cycle constant and varied the actuation pressure amplitude in one device (S11) and found that the flow rate in the device could be varied continuously with actuation amplitude as well (Fig. 4.6). We hypothesize that the flow direction is determined by the relative balance of upstream versus downstream hydraulic resistance, as the momentum is injected via the channel ceiling motion roughly at the mid channel location. An observation with implications for the hydraulic resistance in the channel is that asymmetry was observed in the collapse and re-expansion of the elastomeric membrane. It was also observed that, apart from the actuation frequency, the flow reversal of device S4 depended on the actuation pressure as is evident from Fig. 4.9 where the

transition pressure range has been plotted against the actuation frequency. For each of the data sets, the frequency was kept constant while varying the pressure. It was observed that keeping the frequency constant, increasing the magnitude of the pressure above a certain threshold range reversed the flow direction. Also, the magnitude of the transition pressure range increased with an increase in frequency. This shows that the flow reversal for device S4 depends not only on the frequency but also on the pressure of the actuation. Figure 4.8 shows the variation of maximum deflection of the larger and smaller contractions of device S4 with actuation pressure, calculated using the following formula (from [25]) for maximum deflection of a rectangular PDMS membrane. Though the shape of the membranes in both the contraction sites in device S4 is trapezoidal, the following formula has been used to plot the maximum deflection for equivalent rectangular membranes with the same surface area as the trapezoidal ones.

$$\delta_{max} = \frac{w_m}{4} \left( \frac{3\Delta P w_m}{E t_m} \right)^{\frac{1}{3}} \quad (4.1)$$

Here,  $\delta_{max}$  is the maximum deflection and  $\Delta P$  is the pressure difference across the membrane. It is evident from the graph that the maximum deflection of the smaller contraction is less than the depth of the fluidic channel ( $80\mu\text{m}$ ) up to 7 psi whereas the larger contraction touches the channel floor even at a very low pressure of 0.11 psi. This can also be verified from Fig. 4.7 where it is clearly seen that both the smaller and larger contractions touch the fluid channel floor at a pressure of 15 psi. In order to get an estimate of the difference between the times taken by the larger and smaller contractions to reach their respective maximum deflections in device S4, the following formula was used from [25],

$$t = 3.5 \left( R_i + \epsilon \frac{\rho}{2} \frac{Q_v}{A_v^2} \right) C_o (\Delta P)^{-\frac{2}{3}} \quad (4.2)$$

In the above equation  $t$  is the response time and  $\Delta P$  is the corresponding pressure difference across the membrane for the two contractions. Using the dimensions, material properties, and hydraulic resistances for the two contraction regions, it was seen that for the same actuation pressure the time taken by the larger contraction to reach its maximum deflection was approximately 25 times the time taken by the smaller contraction. Thus, there is an inherent time lag between the two contractions in the device S4 even though there is no externally imposed one as can be seen in some of the other devices. Also, it was observed that both the larger and the smaller contractions touch the floor of the fluid channel up to frequencies in the range of 20-30 Hz, which is much higher than the transition frequency of device S4. Beyond 20-30 Hz the membranes at the contraction sites were not given enough time to collapse, thus decreasing the magnitude of the flow rate. So, it can be concluded that the difference in the hydraulic resistance pattern created by the contraction sites touching or not touching the floor of the channel does not play a role in the reversal of the flow direction in device S4.

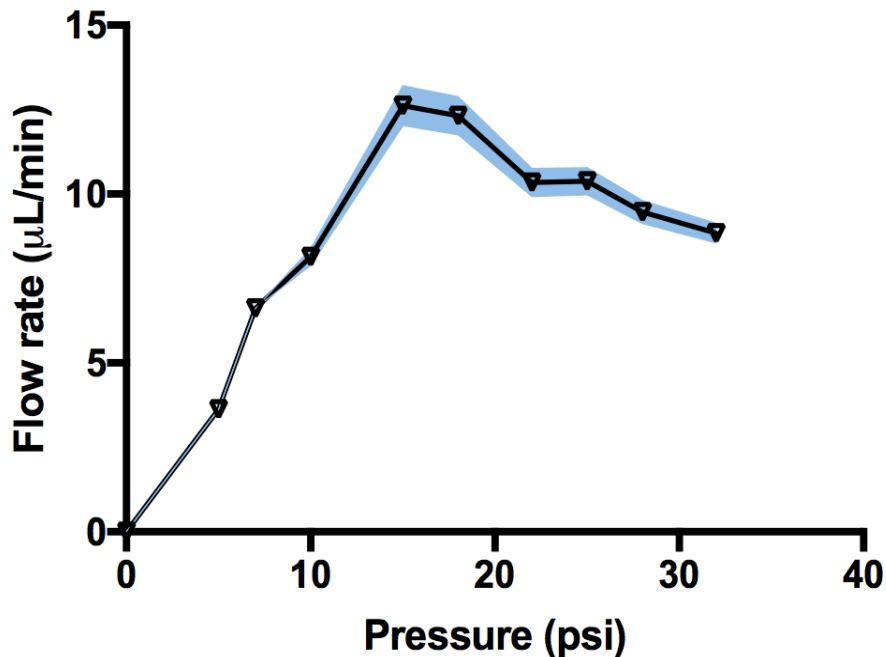


Figure 4.6: Volumetric flow rate versus actuation pressure magnitude for device S11. The shading represents the uncertainty in the data due to measurement error and is calculated as the maximum possible error in the volumetric flow rate due to the resolution of the measurement of the time taken by the fluid front to travel a certain distance in the outlet tube.

We observed that for the larger collapse sites in the tapered channel devices the membrane collapsed at the ends of the membrane first and the collapse propagated inward toward the membrane center during the collapse part of the cycle (see, e.g., Fig. 4.7, first column). During the re-expansion part of the cycle, however, the membrane re-expanded uniformly (Fig. 4.7, second column).

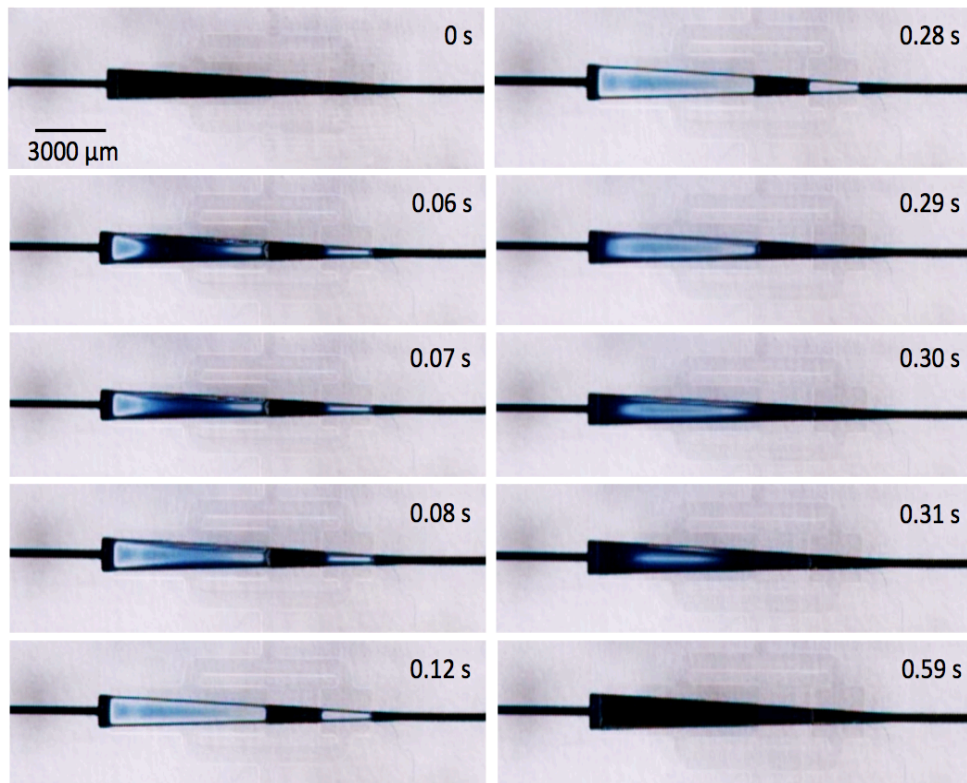


Figure 4.7: Top view of device S4 over a complete collapse and re-expansion cycle. Left column displays collapse images. Right column displays re-expansion images.

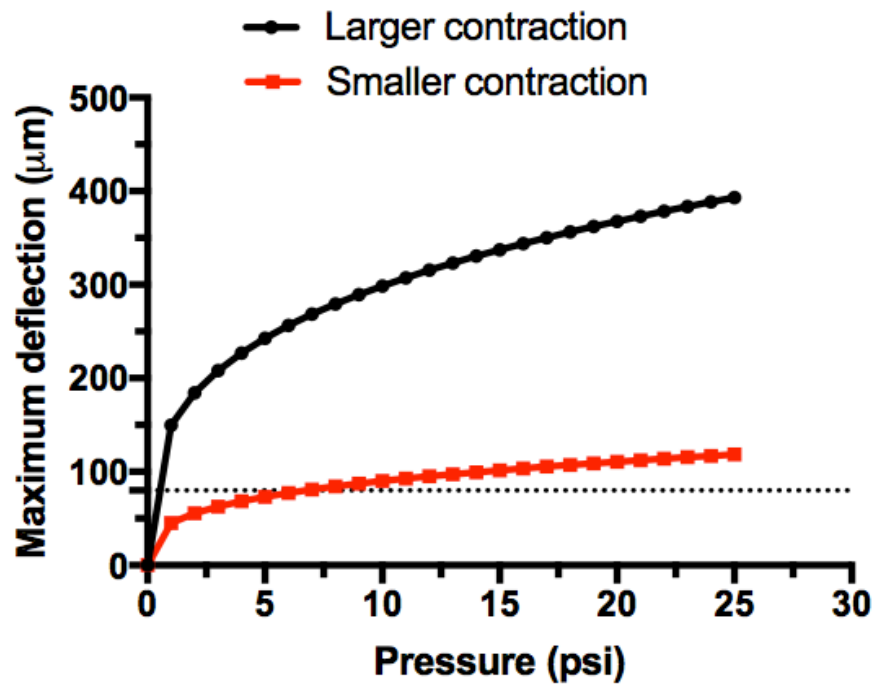


Figure 4.8: Maximum deflection versus actuation pressure for larger and smaller contractions of Device S4.

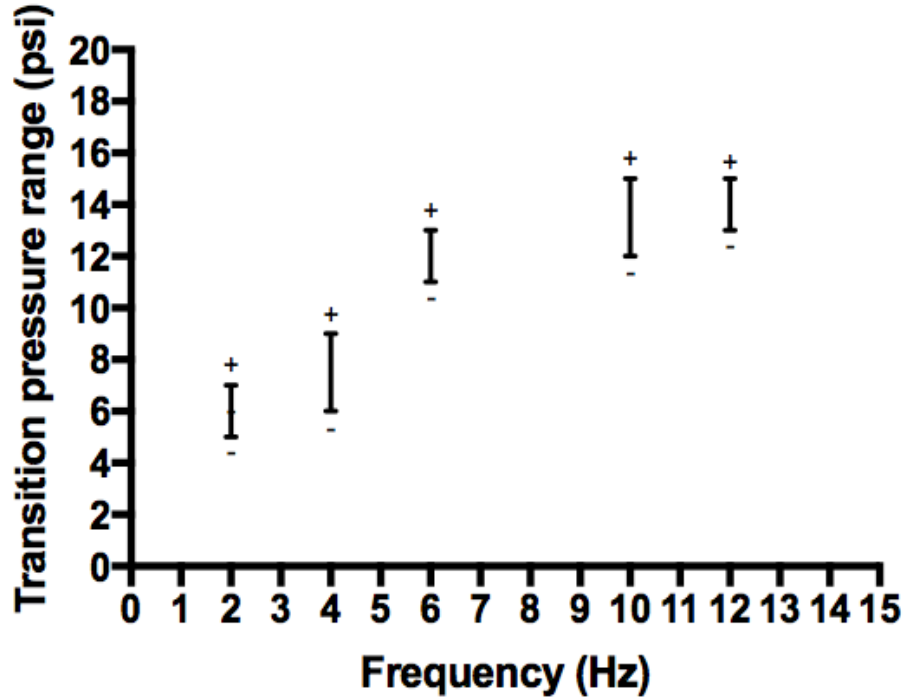


Figure 4.9: Pressure range of flow transition from one direction to the other plotted against actuation frequency for Device S4. The ‘+’ and the ‘-’ signs represent flows towards the positive and negative directions respectively.

Four multichannel devices were designed and fabricated (Figs. 4.11 and 4.12) that used the basic geometric structure of the main thoracic tracheal network found in many insect species (for example, in *Platynus decentis*, as shown in Fig. 4.1a), and whose individual flow channels were designed after analyzing the results of the single-channel device flow rate experiments.

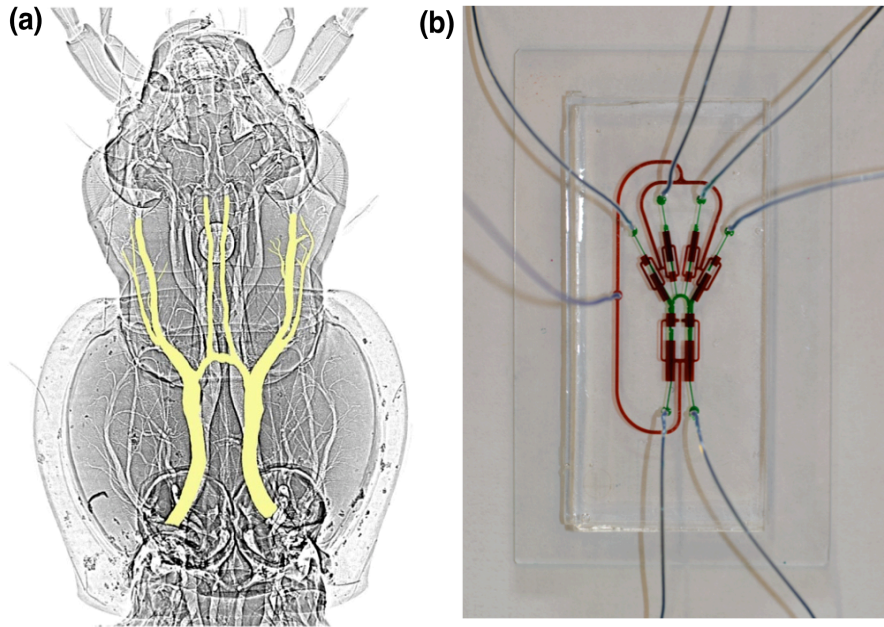


Figure 4.10: **a**, Synchrotron X-ray image of *Platynus decentis* (top view) head and thorax with largest thoracic respiratory tracts highlighted (modified by J.J. Socha with permission from [26]). **b**, Photograph of fabricated microfluidic network device mimicking the highlighted part as shown in Fig. 4.10(a) with green dye in the flow channel and red dye in the overlying actuation channel for visualization purposes.

One aim of the designs was to be able to direct flow into specific branches of the network based on actuation frequency alone by using individual channel designs based on the single-channel device S4, which displayed flow direction reversal. (The exception to this was in device M1, where the daughter channels were not based on single-channel device designs.) Relying on symmetry, the experiments were performed in half the left-right symmetric device in order to double the number of experiments. This was accomplished by etching away the connecting bridge between the channels labeled “B” in Figs. 4.11 and 4.12, resulting in the half devices shown at the tops of the columns of images in Figs. 4.13 and 4.14.

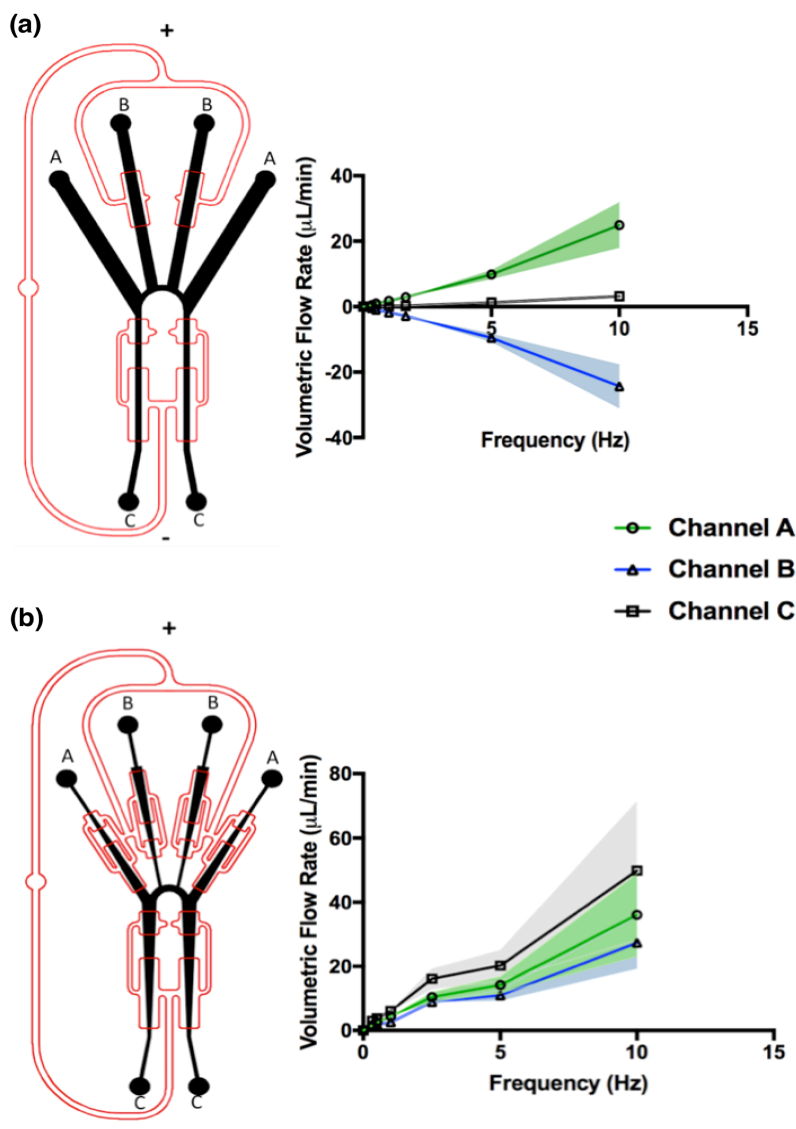


Figure 4.11: Schematics and flow rate data for two multichannel microfluidic devices. Both the devices are left-right symmetric. Positive flow is toward the top of the device, in the direction of the '+' symbol. The shading represents the uncertainty in the data due to measurement error and is calculated as the maximum possible error in the volumetric flow rate due to the resolution of the measurement of the time taken by the fluid front to travel a certain distance in the outlet tube. **a**, Device M1 displays frequency-dependent channel selectivity. Below a critical actuation frequency, there is no flow produced through channel C, positive flow through channel A, and negative flow through channel B. After the critical frequency (about 5 Hz) there is positive flow through channel C, positive flow through channel A and negative flow through channel B. **b**, Device M2 produces positive flow through all three channels, A,B, and C, at every actuation frequency tested.

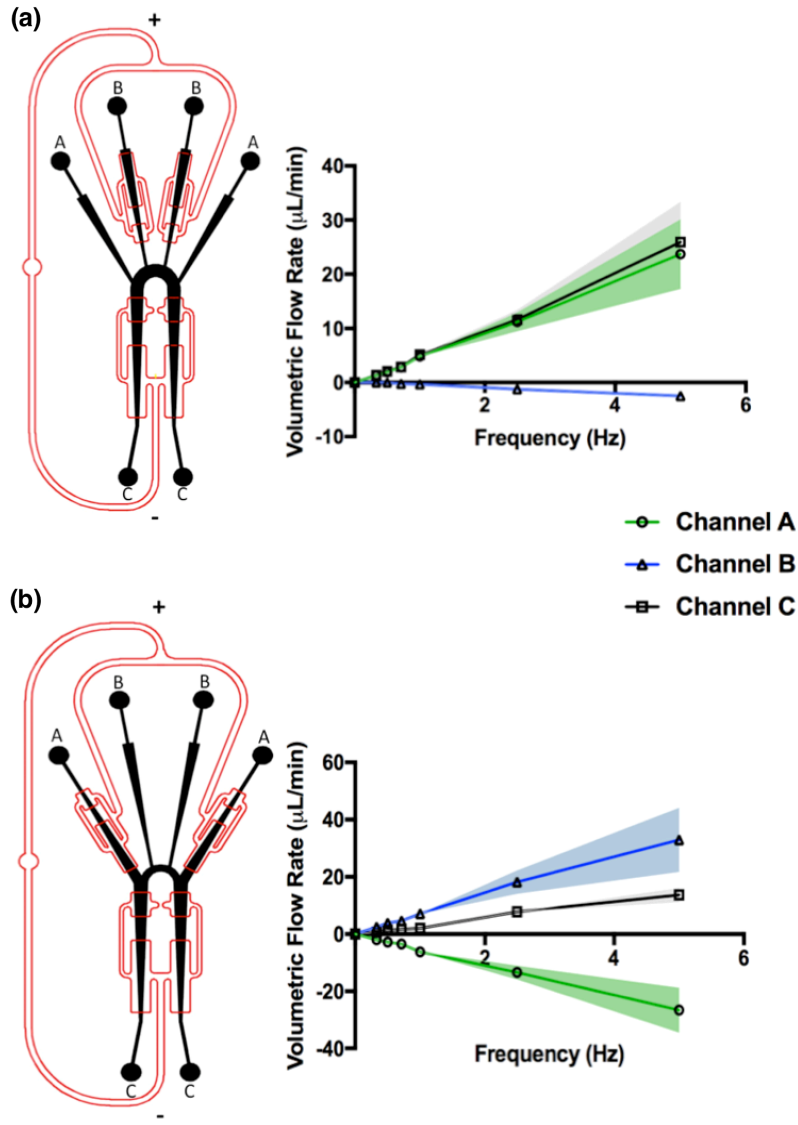


Figure 4.12: Schematics and flow rate data for two multichannel microfluidic devices. Both the devices are left-right symmetric. Positive flow is toward the top of the device, in the direction of the '+' symbol. The shading represents the uncertainty in the data due to measurement error and is calculated as the maximum possible error in the volumetric flow rate due to the resolution of the measurement of the time taken by the fluid front to travel a certain distance in the outlet tube. **a**, Device M3 produces negligible flow through channel B for actuation frequencies below a threshold frequency of about 1 Hz, after which it produces a negative flow in channel B. The device produces positive flow in channels A and C for all actuation frequencies tested. **b**, Device M4 produces positive flow through channels A and C and negative flow through channel B at every actuation frequency tested.

These network devices were then subjected to the same square wave periodic actuation pressure signal as the single channel devices and the resulting flow rates in the constitutive channels were measured. Two of the multichannel designs (M1 and M3) successfully directed flow into a single branch of the network only above a critical frequency. Below that critical frequency (around 5 Hz for device M1 and 1 Hz for device M3) negligible flow passed through the channel in question (channel C for device M1 and channel B for device M3). The absence of flow through channel B in device M3 is demonstrated in Figs. 4.13 and 4.14. In Fig. 4.13a, the actuation frequency is above the critical value and black dye can clearly be seen in channel B and in channel A. In Fig. 4.13b, the actuation frequency is below the critical value and only a negligible amount of the black fluid from the reservoir at the tip of channel B passes into channel A. This negligible amount possibly occurred due to diffusion.

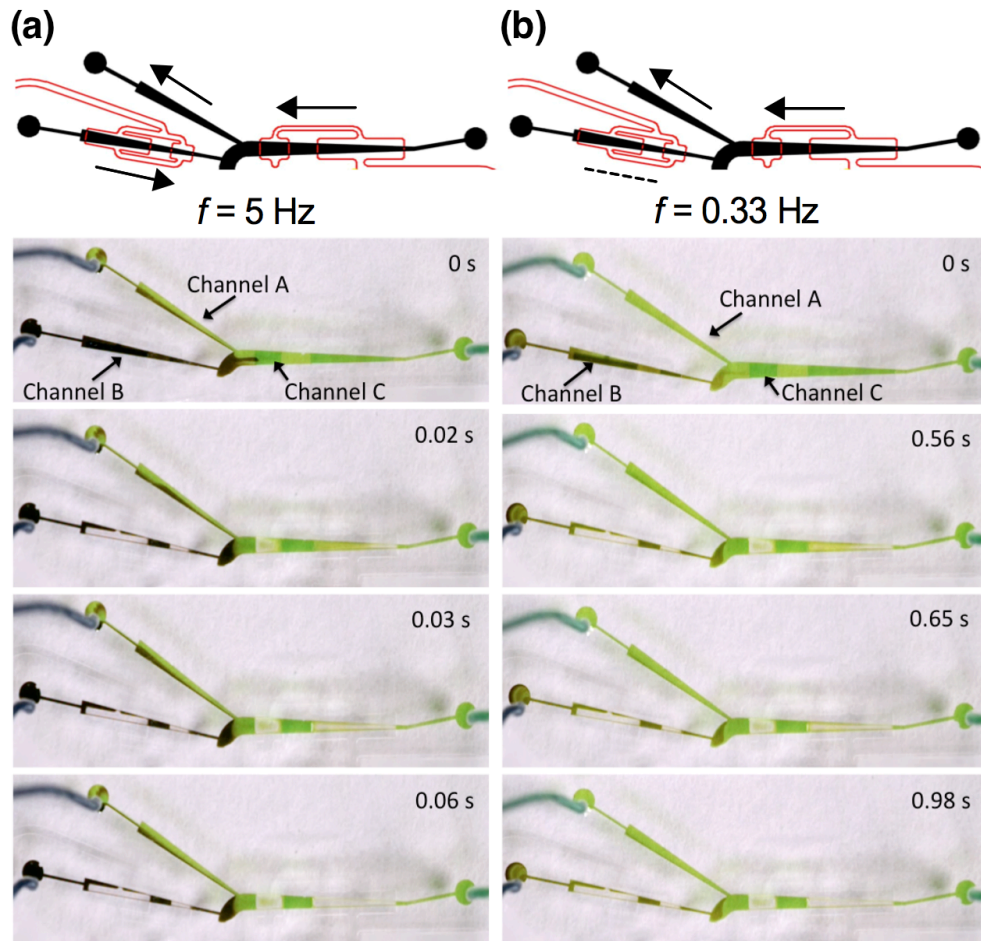


Figure 4.13: Tests were performed in half the symmetric network with water mixed with food coloring. The actuation pressures for the tests was 13 psi. Flow direction convention is the same as in 4.11 or 4.12. **a**, Device M3 actuated at high frequency (5 Hz). At this frequency, which is higher than the critical frequency for device M3, the black liquid from the reservoir feeding channel B walls pumped in the negative direction and mixed with the green fluid in channel A, which pumped fluid in the forward direction. Channel C also pumped fluid in the forward direction. **b**, Device M3 actuated at low frequency (0.33 Hz). At this frequency below the critical frequency frequency for device M3, no black fluid is pumped from the reservoir into channel B, while the green fluid in channels A and C is pumped forward.

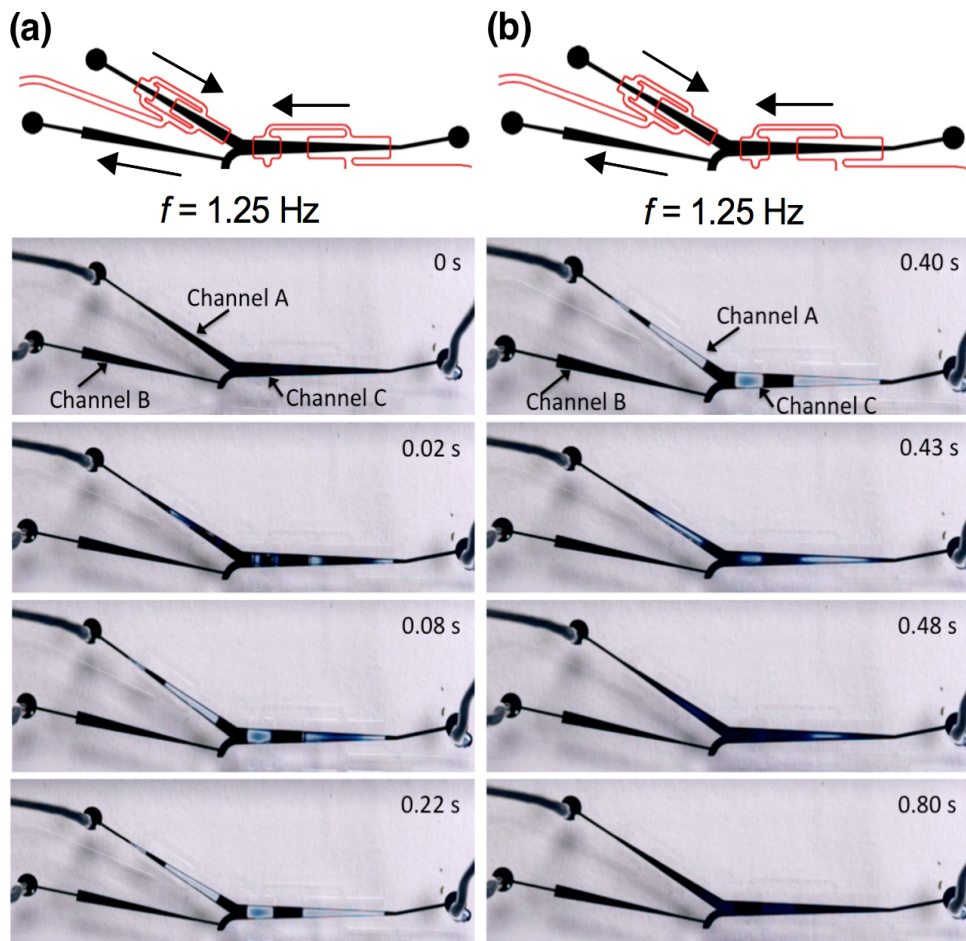


Figure 4.14: Tests were performed in half the symmetric network with water mixed with food coloring. The actuation pressures for the tests was 17 psi. Flow direction convention is the same as in 4.11 or 4.12. **a**, Device M4 actuated at 1.25 Hz, contraction part of cycle. fluid was pumped from channel A and channel C into channel B. **b**, Device M4 actuated at 1.25 Hz, re-expansion part of cycle. Fluid continued to be pumped from channels A and C into channel B.

## 4.4 Concluding remarks and future scope

It remains to be seen if these results will scale up to the full vLSI scale, with a single actuation providing rich, passive control of thousands of flow channels as in entomological respiratory systems, given the many differences between insects' complex three-dimensional respiratory

apparatuses and the planar geometries of current vLSI microfluidic devices. In spite of the limitations in transferring exact entomological microfluidics control strategies to engineered microfluidic devices, many more fundamental aspects of insect respiratory systems remain ripe for investigation, including the role of the respiratory taenidia in mixing, heat, and mass transfer in gaseous microfluidics, and looking to insect respiratory architectures for clues about efficient geometries and strategies when scaling microfluidics up to three dimensions, as critical microfluidics applications like integrated circuit cooling will require.

# References

- [1] International Technology Roadmap for Semiconductors 2.0, 2015 Edition, Executive Report.
- [2] Sarkar, Deblina and Xie, Xuejun and Liu, Wei and Cao, Wei and Kang, Jiahao and Gong, Yongji and Kraemer, Stephan and Ajayan, Pulickel M. and Banerjee, Kaustav, A subthermionic tunnel field-effect transistor with an atomically thin channel, *Nature*, 526, 91-95 (2015).
- [3] Yager, P., Edwards, T., Fu, E., Helton, K., Nelson, K., Tam, M. R., and Weigl, B. H., Microfluidic diagnostic technologies for global public health, *Nature*, 442, 412-418 (2006).
- [4] Thorsen, T., Maerkl, S. J., and Quake, S. R., Microfluidic large-scale integration. *Science*, 298 (5593), 580-584 (2002).
- [5] Araci, I. E. and Quake, S. R., Microfluidic very large scale integration (mVLSI) with integrated micromechanical valves, *Lab on a Chip*, 12, 2803-2806 (2012).
- [6] White, J. A. and Streets, A. M., Controller for microfluidic large-scale integration. *HardwareX*, 3, 135-145 (2018).
- [7] Pop, P., Minhass, W. H., and Madsen, J., Microfluidic very large scale integration (vLSI): Modeling, simulation, testing, compilation and physical synthesis, Springer International Publishing (2016).
- [8] Leslie, D. C., Easley, C. J., Seker, E., Karlinsey, J. M., Utz, M., Begley, M. R., and Landers, J P., Frequency-specific flow control in microfluidic circuits with passive elastomeric features, *Nature Physics*, 5, 231-253 (2009).

- [9] Jain, R. and Lutz, B., Frequency tuning allows flow direction control in microfluidic networks with passive features, *Lab on a Chip*, 17, 1552-1558 (2017).
- [10] Wegener, G., Flying insects: model systems in exercise physiology, *Experientia*, 52 (5), 404-412 (1996).
- [11] Weis-Fogh, T., Fat combustion and metabolic rate of flying locusts (*Schistocerca gregaria* Forskgtl). *Phil. Trans. R. Soc. Ser. B*, 237, 1-36 (1952).
- [12] Kammer, A. E., and Heinrich, B., Insects flight metabolism, *Adv. Insect Physiol.*, 13, 133-228 (1978).
- [13] Westneat, M. W., Betz, O., Blob, R. W., Fezzaa, K., Cooper, W. J., and Lee, W.-K., Tracheal respiration in insects visualized with synchrotron x-ray imaging, *Science*, 299 (5606), 558-560 (2003).
- [14] Socha, J. J., Lee, W.-K., Harrison, J. F., Waters, J. S., Fezzaa, K., and Westneat, M. W., Correlated patterns of tracheal compression and convective gas exchange in a carabid beetle, *Journal of Experimental Biology*, 211, 3409-3420 (2008).
- [15] Westneat, M. W., Socha, J. J., and Lee, W.-K., Advances in Biological Structure, Function, and Physiology Using Synchrotron X-Ray Imaging, *Annual Reviews of Physiology*, 70, 119-142 (2008).
- [16] Socha, J. J., Forster, T. D., and Greenlee, K. J., Issues of convection in insect respiration: Insights from synchrotron X-ray imaging and beyond, *Respiratory Physiology & Neurobiology*, 1735, S65-S73 (2010).
- [17] Webster, M. R., De Vita, R., Twigg, J. N., and Socha, J. J., Mechanical properties of tracheal tubes in the American cockroach (*Periplaneta americana*), *Smart Materials and Structures*, 20, 094017 (2011).

- [18] Waters, J. S., Lee, W.-K., Westneat, M. K., and Socha, J. J., Dynamics of tracheal compression in the horned passalus beetle, *American Journal of Physiology - Regulatory, Integrative and Comparative Physiology*, 304, R621-R627 (2013).
- [19] Aboelkassem, Y. and Staples, A. E., Flow transport in a microchannel induced by moving wall contractions: a novel micropumping mechanism, *Acta Mechanica*, 223 (3), 463-480 (2012).
- [20] Aboelkassem, Y. and Staples, A. E., Selective pumping in a network: insect-style microscale flow transport, *Bioinspiration & Biomimetics*, 8 (2), 026004 (2013).
- [21] Aboelkassem, Y. and Staples, A. E., Stokeslets-meshfree computations and theory for flow in a collapsible microchannel, *Theoretical and Computational Fluid Dynamics*, 27 (5), 681-700 (2013).
- [22] Aboelkassem, Y. and Staples, A. E., A bioinspired pumping model for flow in a microtube with rhythmic wall contractions, *Journal of Fluids and Structures*, 42, 187-204 (2013).
- [23] Aboelkassem, Y. and Staples, A. E., A three-dimensional model for flow pumping in a microchannel inspired by insect respiration, *Acta Mechanica*, 225 (2), 493-507 (2014).
- [24] Chatterjee, K. and Staples, A. E., Slip flow in a microchannel driven by rhythmic wall contractions, *Acta Mechanica*, *Acta Mechanica*, <https://doi.org/10.1007/s00707-018-2210-7>, 1-17 (2018).
- [25] Liu, X., Li, S., & Bao, G. (2016). Numerical simulation on the response characteristics of a pneumatic microactuator for microfluidic chips. *Journal of laboratory automation*, 21(3), 412-422.

- [26] Socha, J. J., & De Carlo, F. (2008, September). Use of synchrotron tomography to image naturalistic anatomy in insects. In *Developments in X-Ray Tomography VI* (Vol. 7078, p. 70780A). International Society for Optics and Photonics.

# Chapter 5

## Conclusions and future work

### 5.1 Summary and concluding remarks

The studies presented in this dissertation have focused on the development of mathematical models and the fabrication, analysis and testing of insect mimetic microfluidic systems. In order to solve some of the most persistent problems in engineering, researchers have derived inspiration from nature and developed the concept of bioinspired or biomimetic engineering. This revolutionary concept has resulted in important breakthroughs and critical inventions that have had a profound impact on our lives and significantly added to our understanding of nature and its principles.

Microfluidic technology has seen a significant development in the last few decades due to some of its inherent advantages over macroscale fluid dynamics. The ease of fabrication, portability, small sample requirement, lightweight and small space requirement has made microfluidic technology a popular concept in several areas of research such as biology, biomedical science, chemistry, biochemical research, and mechanics research. While there have been developments in the miniaturization and functionality of microfluidic devices, little have been explored on the topic of reduction or simplification of the associated machinery required to drive these devices. Nowadays with the popularity of the concepts of lab-on-a-chip and the development of microfluidic cards for chemical analysis of extraterrestrial environments,

getting rid of some extra space might be a vital factor behind the success or failure of a mission or a biomedical device. But, insects on the other hand, for generations have utilized evolutionary refinements to their respiratory system to actively manipulate and control the flow of respiratory gases inside their tracheal or respiratory tubes. It is this efficiency in handling of fluids that gives insects superior metabolic capabilities which are required for different purposes for example flight and locomotion. In this thesis, equipped with a newly found knowledge of the working principle of the insect respiratory system, we focused our attention on mathematical modeling and practical manufacturing of insect respiratory system inspired microfluidic devices that employ an unique pumping mechanism. The study brought to light a number of vital results and findings.

In the first study, after mathematically investigating the effects of slip boundary conditions on insect mimetic microchannel flow, it was found that there is a difference between the ways in which rarefaction affects the magnitude of the axial velocity in pressure gradient and wall shear dominated regions. For the regions of the microchannel dominated by pressure gradient, increasing the magnitude of slip, increased the axial velocity while the opposite happened in the contraction or wall shear dominated regions. Increase in slip or Knudsen number values reduced the volumetric flow rate over an entire contraction-relaxation cycle. Thus increase in the slip value may act as a diffuser by slowing the flow in small tracheal tubes thus increasing the resident time of oxygen in the tissues for respiration.

In the second study the same type of insect inspired wall collapse driven flow was modeled, but this time, the cylindrical coordinate system was used along with more physiologically realistic intratracheal pressure data. This was done in order to model the fluid flow inside certain regions of the tracheal tubes where there might be a coexistence of slip boundary

conditions as well as wall contractions. An identical relationship was found to exist between the Knudsen number and pressure gradient or wall shear stress as in the earlier section. But, one interesting result obtained from this study was the existence of negative flows for certain phase lag values. It is possible that insects use a similar strategy of phase lag control (produced via abdominal contraction frequency modulation) that, together with existing spiracular-tracheolar pressure differences (which may also be controlled via the spiracular valves) may allow them to generate bidirectional fluid flows in portions of their respiratory systems.

In the third study, some essential insect respiratory kinematics have been incorporated into the design of fifteen microfluidic devices which were then fabricated, tested, and analyzed. Eleven single channel and four multichannel devices were built where the flow was generated either by discrete wall collapse, directional wall collapse or both. All these devices were pneumatically actuated by a single pressure pulse distributed in different areas over the fluid channel as actuation sites. Flow rate versus actuation frequency plots were generated for all the devices. Each of the devices acted as a hydrodynamic ratchet, rectifying the symmetric actuation pressure input signal into unidirectional flow. In one single channel device, in particular, it was possible to change not only the magnitude but also the direction of the flow by varying the actuation frequency alone for a given actuation pressure. In the insect respiratory network mimetic multichannel devices it was possible to control the flow rate in the individual flow branches just by changing the actuation frequency. In two of the multichannel devices, at low frequencies, there were channels that produced negligible flow and were essentially switched off, but above a critical frequency, there was an appreciable amount of flow in these channels. Hence, the devices could turn the flow in certain channels on an off based on actuation frequency alone for a given actuation pressure.

These features have never been realized before in a valveless microfluidic device and may lead to drastically reduced actuation overhead in future generations of pneumatically actuated complex microfluidic devices.

## 5.2 Recommendations for future research

The results of the studies presented here may have important implications in future microfluidic device design. The idea of a single, integrated actuation channel coupled with geometric asymmetries in the individual flow channels can be used to fabricate more efficient, simpler, and cheaper microfluidic devices for diverse applications by reducing the actuation machinery from multiple actuation channels per flow channel to one actuation channel per microfluidic device. The principles described here can be employed in the fabrication of simpler models of organ-on-chip devices where there is a requirement to accurately mimic the hydrodynamic, physiological and mechanical microenvironment of the organs, and in chemical analysis systems. And if fabricated at a suitable scale, some of these devices when connected with each other, may act as efficient cell sorting mechanisms. Additionally, there is reason to believe that these insect-inspired microfluidic devices may be efficient at microscale mixing because of their pulsatile actuation mechanism combined with temporally and spatially varying hydraulic resistance profiles, a topic which may lead to fruitful investigations. Lastly, these studies may act as the starting point of a new discipline of insect mimetic microfluidics that has the potential to develop novel and efficient microscale pumping, mixing, sorting, and distribution mechanisms.

# Appendices

# Appendix A

## A.1 Derivation of reduced governing equations used in chapters 2 and 3

The analysis presented here is in the rectangular cartesian coordinate system following chapter 2, but the same derivation process is used in chapter 3 also using cylindrical polar coordinates. Using the non-dimensionalization scheme used in 2.4, the 2D Navier-Stokes equations for an incompressible, isothermal flow of a Newtonian fluid with constant viscosity, reduced to

$$\frac{\partial u}{\partial x} + \frac{\partial v}{\partial y} = 0 \quad (\text{A.1})$$

$$Re\delta \left[ \frac{\partial u}{\partial t} + u \frac{\partial u}{\partial x} + v \frac{\partial u}{\partial y} \right] = -\frac{\partial p}{\partial x} + \delta^2 \frac{\partial^2 u}{\partial x^2} + \frac{\partial^2 u}{\partial y^2} \quad (\text{A.2})$$

$$Re\delta^3 \left[ \frac{\partial v}{\partial t} + u \frac{\partial v}{\partial x} + v \frac{\partial v}{\partial y} \right] = -\frac{\partial p}{\partial y} + \delta^4 \frac{\partial^2 v}{\partial x^2} + \delta^2 \frac{\partial^2 v}{\partial y^2} \quad (\text{A.3})$$

The channel geometry is assumed to have a very high aspect ratio ( $\delta \ll 1$ ) and the microscale flow through it has a very low Reynolds number. Thus, assuming the Reynolds number as the same order of magnitude as the reciprocal of aspect ratio (following classical lubrication theory), all terms of order  $\delta^2$  and higher can be neglected. Using these

assumptions, the above equations can be reduced to,

$$\frac{\partial u}{\partial x} + \frac{\partial v}{\partial y} = 0 \quad (\text{A.4})$$

$$-\frac{\partial p}{\partial x} + \frac{\partial^2 u}{\partial y^2} = 0 \quad (\text{A.5})$$

$$\frac{\partial p}{\partial y} = 0 \quad (\text{A.6})$$

# Appendix B

## B.1 Materials and methods

**Preparation of silicon wafers with desired positive features** The protocol developed for after the fabrication of masks (C.2) from CAD designs (C.1) is outlined in the following steps,

**Step 1:** The silicon wafer was first cleaned using Acetone, Isopropanol (IPA) and distilled water.

**Step 2:** It was dehydrated on hot plate at 110°C for 10 minutes.

**Step 3:** SU8 2035 was spin coated on the wafer, in the spinner initially at 500 rpm for 20 seconds and then at 1000 rpm for 1 minute 20 seconds.

**Step 4:** SU8 coated wafer was then soft baked on hot plate at 65°C for first 3 minutes and then at 95°C for next 9 minutes.

**Step 5:** It was then exposed under the UV lamp for 30 seconds with the mask on top of it.

**Step 6:** After the exposure, the wafer was soft baked again on hot plate, initially at 65°C for 2 minutes and then at 95°C for 7 minutes.

**Step 7:** It was then developed by immersing it in a developer solution for 7 minutes or till the wafer clearly showed the features. The height of the features, which depends on the rotational speed during the spin coating process is approximately 80  $\mu\text{m}$  which is equivalent to the depth of all the actuation and the fluid channels used in the present study.

**Step 8:** It was then spun in the spinner and cleaned with IPA.

**Step 9:** After drying it off, the wafer was silanized by keeping it in vacuum. 10  $\mu\text{L}$  of silane

was put in a cap and kept beside the wafer in the vacuum chamber for at least 2 hours. Silanizing the wafer enables easy removal of cured PDMS from its surface, in the later stages of the fabrication procedure.

**Preparation of the PDMS molds with the actuation and fluid channels** The protocol is as follows,

**Step 1:** Polydimethylsiloxane (PDMS) (Dow Corning, Sylgard 184) was mixed thoroughly, in 10:1 base (27 grams) to cross linker (2.7 grams) ratio in a container and kept in vacuum for 30 minutes to remove air bubbles.

**Step 2:** The silicon wafer was wrapped in aluminum foils with the positive features facing up and small aluminum walls around the wafer.

**Step 3:** The liquid PDMS was taken out of the vacuum, pored on the wafers and then the set up was kept in the vacuum again for 10 minutes to remove air bubbles.

**Step 4:** It was then baked on hot plate at  $65^{\circ}$  for 10 minutes and then at  $100^{\circ}$  for 30 minutes.

**Step 5:** After the cured PDMS was allowed to cool, the edges were carefully cut by a scalpel and slowly peeled off.

**Preparation of the thin membranes in between the channels** The protocol is outlined as follows,

**Step 1:** PDMS was mixed thoroughly, in 5 : 1 base (2 grams) to cross linker (0.4 grams) ratio in a container and kept in vacuum for 30 minutes to remove air bubbles.

**Step 2:** A silicon wafer which has already been silanized was cleaned and then spin coated with the PDMS in the spinner at 500 rpm for 15 seconds and then at 3500 rpm for 45 seconds. This created a membrane of approximately  $14 - 20\mu\text{m}$  thickness. The spin speed can

be varied in order to create a membrane of different thickness.

**Step 3:** It was then baked at 100°C for 30 minutes and then allowed to cool off.

**Assembly of the device** The protocol is outlined as follows,

**Step 1:** The PDMS layer with the actuating channel was inserted in the plasma cleaner (Harrick Plasma, PDC-001) along with the membrane coated silicon wafer.

**Step 2:** The vacuum of the plasma cleaner was turned on and allowed to run for 2 minutes.

**Step 3:** After 2 minutes the plasma was turned on and the equipment was allowed to run for another 2 minutes.

**Step 4:** After taking out both the PDMS layer with actuating channels and the membrane coated silicon wafer from the plasma cleaner, they were manually bonded within 2 minutes by applying a small amount of pressure.

**Step 5:** The set up was kept on a hot plate at 70° – 80° for at least 2 hours.

**Step 6:** The PDMS layer bonded with the membrane was then slowly and carefully peeled off from the surface of the wafer.

**Step 7:** The inlet and outlet tube holes for the microfluidic as well as the actuating channels were punched with a 0.75 mm biopsy punch.

**Step 8:** Both the membrane covered actuating channel and the PDMS layer with the fluid channel were inserted in the plasma cleaner and the earlier process was repeated.

**Step 9:** After taking them out of the plasma cleaner, the membrane covered actuating channel was carefully aligned on top of the microfluidic channel with the help of alignment marks and they were bonded by applying a small amount of pressure within 2 minutes.

**Step 10:** The entire device was again bonded to a glass slide by following step 1 through step 5 of the assembly process.

**Step 11:** the devices were kept in vacuum until the experiments

The schematic of the fabrication and assembly process have been presented in [C.3](#).

**Experimental set up.** (Schematic in [C.4](#)) The actuating channels were pressurized using Nitrogen and depressurized by vacuum through a single port which served both as an inlet and an outlet. The pressure of the Nitrogen was regulated via a miniature precision regulator (McMaster Carr, 2227T21). In order to switch between pressurized gas and vacuum, the actuating channel was connected via tubing (Cole Parmer, AWG 30) to a fast acting solenoid valve (FESTO, MHE2-MSIH-5/2-QS-4-K 525119 D002). A 24 V power supply was used to power the solenoid valve which was computer controlled by Arduino using a solid state relay (Arduino, Board model: UNO R3).

**Experimental method.** Before conducting each run, the devices were primed by using ethanol to remove bubbles. Food coloring mixed with water was used as the working fluid in the microfluidic channels. The inlet and the outlet ports of the fluid channel were connected to short length tubes. The flow rate produced by the actuation of the thin membrane, in specified areas on top of the fluid channel, was calculated by measuring the displacement of the fluid in the outlet tube as well as the time taken to do so. This was done by placing the outlet tube parallel to a measuring ruler with graduations. At least three readings were taken for a single data point and then the average of them were used in calculating the flow rates. Single channel device S4 showed a dependence of flow direction on the actuation frequency in at least 60 - 70% cases. Since, the positioning of the membrane bonded actuation channel on top of the fluid channel had to be done manually within 2 minutes after taking them out of the plasma cleaner, the rest of the 30 - 40 % cases can be attributed to some misalignment in the manual positioning of the channels. The devices were also tested for repeatability i.e. flow rate data were taken while the frequencies and the pressures were varied from low to

high and then again from high to low. The devices showed the same pattern of behavior in both the cases. High resolution videos of the device performances were captured using high speed video camera (Sanstreak Corp., Edgertronic High Speed Video Camera).

# Appendix C

## C.1 CAD designs of the devices with dimensions

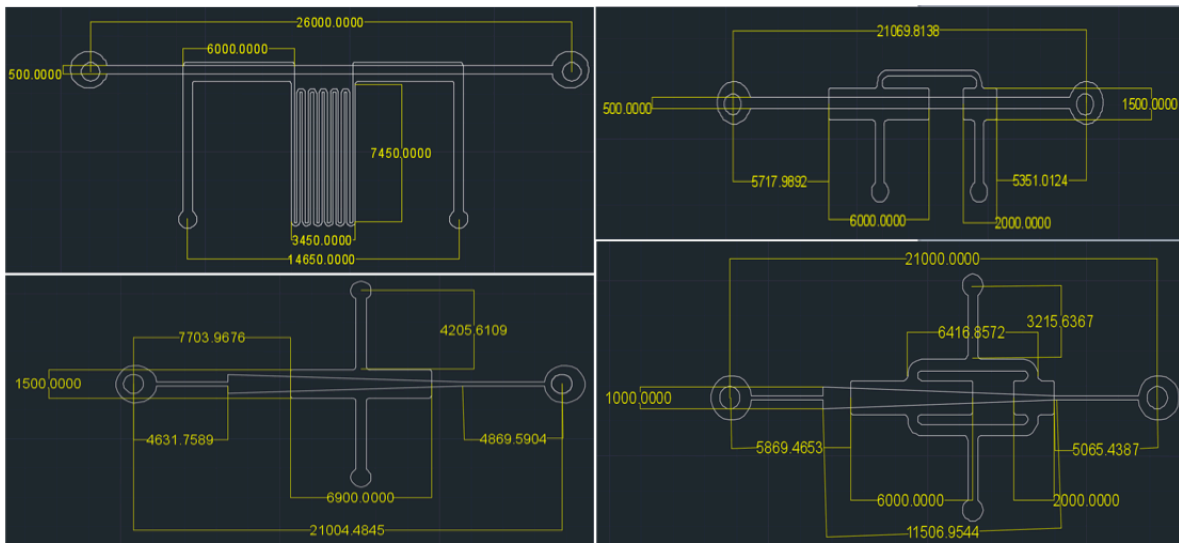


Figure C.1: CAD designs with dimensions (in  $\mu\text{m}$ ) for devices S1 (top left), S10/S11 (top right), S2 (bottom left) and S4 (bottom right). All the dimensions are in  $\mu\text{m}$ .

The single channel devices were designed using AutoCAD student version. All the fluid channels were designed in such a way that they have bigger depth and smaller width so that the membrane after touching the floor of the channel during deflection comes back to its original position easily without sticking on to the surface. Once, it got stuck to the floor of the fluid channel during fabrication, it was really difficult to get it back to its original position. Also, the dimensions of the devices approximately resemble the dimensions of tracheal tubes in some insect species.

## C.2 Masks of the channel device designs

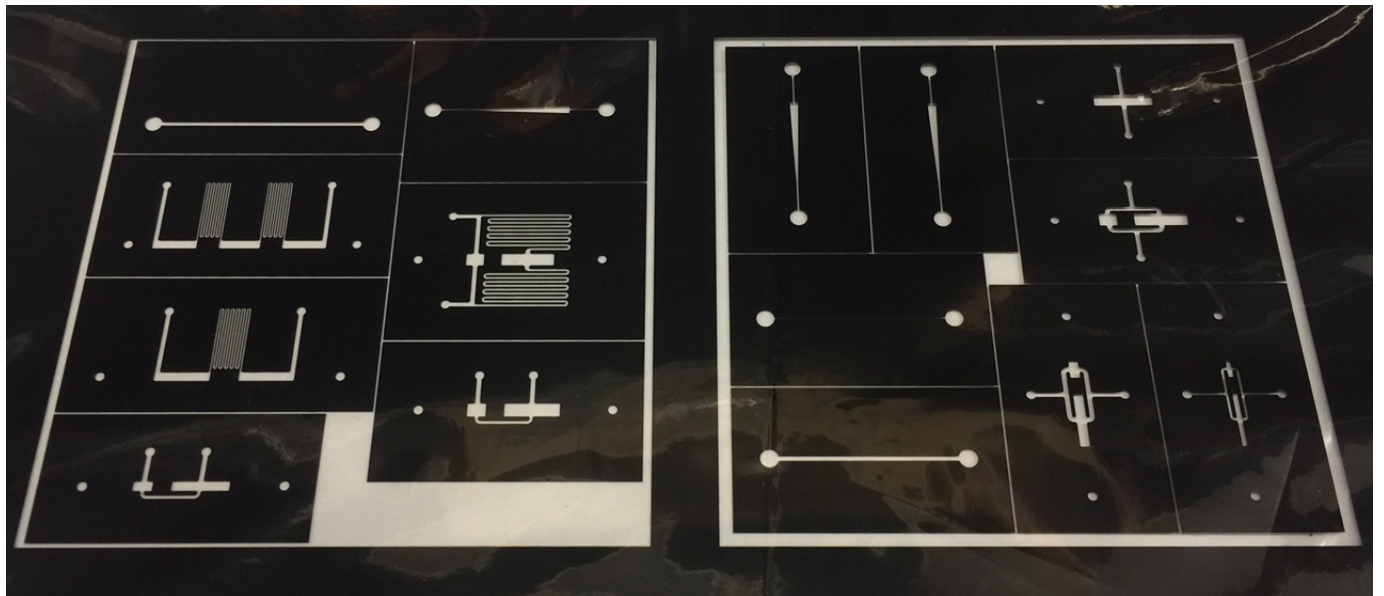


Figure C.2: Masks created from the CAD designs, that were used to create the silicon wafer.

The masks were ordered from an external agency after the CAD designs of the fluidic and actuation channels for the single channel devices were finalized. The masks selectively allow ultraviolet light to pass through and react with the SU8 coating thus forming compounds which leave positive structures on the surface of the silicon channels after the remaining of the unreacted SU8 has been dissolved away.

## C.3 Fabrication and assembly of the microfluidic devices

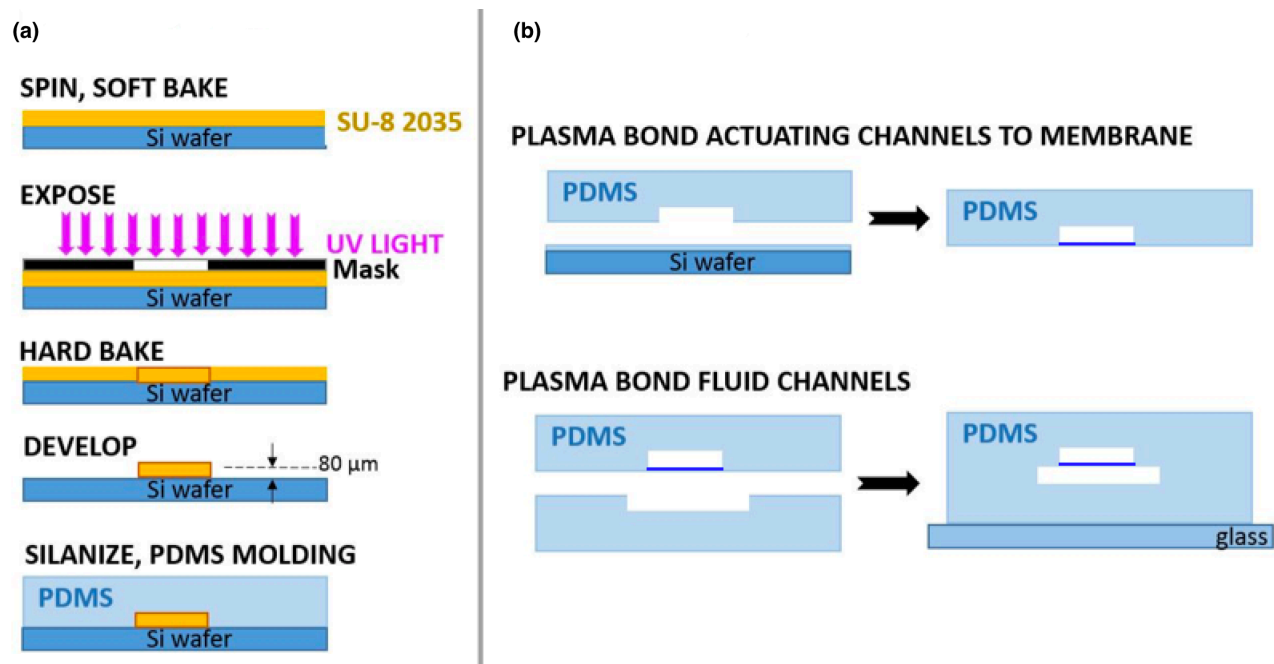


Figure C.3: **a**, Schematic of the soft lithography fabrication technique. **b**, Assembly process of the microfluidic devices.

The single and multichannel devices were fabricated using the standard soft lithography technique as illustrated in the above figure. The left hand side shows the steps involved in the preparation of the PDMS layers with the impressions of the fluid and the actuation channels. The right hand side illustrates the assembly process which is performed using the two PDMS layers with the fluid and the actuation channel impressions and the thin membrane sandwiched between them. A detailed description of the fabrication and the assembly process has been provided in appendix A.

## C.4 Schematic of the experimental setup

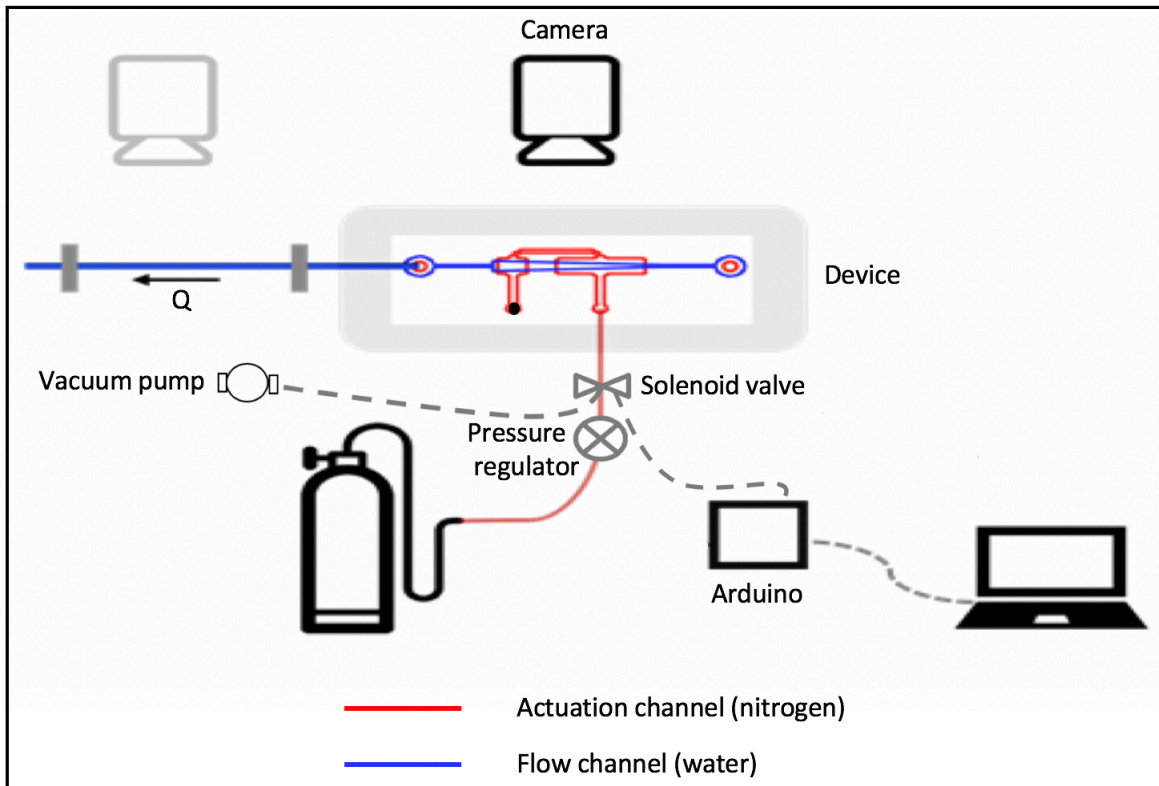


Figure C.4: Schematic of the experimental set up.

The above figure shows the schematic of the experimental set up with all the connections. The supply of pressurized nitrogen was maintained using a nitrogen cylinder and the magnitude and duration of the pressure signal was controlled using a pressure regulator and solenoid valve respectively. The output flow rate from the devices was calculated by measuring the distance traveled by the fluid front in the outlet tube and time taken. A detailed description of the experimental set up has been provided in appendix A.